Dynamics and topology of active and passive liquid crystals

Luuk Metselaar

St John's College

University of Oxford

A thesis submitted for the degree of

Doctor of Philosophy

Trinity Term 2019

Abstract

We study the interplay between flow, structure, and topology in liquid crystals, in both passive and active materials. Liquid crystals are fluids, but at the same time structurally anisotropic and strongly influenced by their topology. They exhibit long-range orientational order, with characteristics between those of simple isotropic fluids and those of crystalline solids. Active materials extract energy from their surroundings at the single particle level and convert it to mechanical work.

First, we consider the elongation of passive nematic droplets suspended in their own isotropic phase, i.e. tactoids, under the influence of an electric field, and show that a tenfold elongation is due to strong anchoring of the directors to the interface. Building on this, we introduce more complicated internal structures in the tactoids, and demonstrate that cholesteric tactoids and two-dimensional blue phase tactoids correspond to a wealth of droplet morphologies. Application of a perpendicular electric field produces structures very similar to chiral rafts, with directors normal to the plane of the tactoid in the centre, but twisting away from the normal at the edge.

Secondly, we turn to active liquid crystals. Here the interaction between topology, structure, and flow is perhaps even more pronounced, with motile $+1/2$ topological defects accompanied by large stresses. We study an active two-dimensional blue phase, and show that it is stable for contractile activity, with the active instability screened by the cholesteric pitch length. Extensile activity, on the other hand, leads to dissociation of the double-twist cylinders and causes active turbulence. An alternative method to screen the active instability is introducing substrate friction. We simulate extensile rod-like active nematics and show that anisotropic friction can give rise to a laning state with antiparallel flow. The transition is strongly sensitive to the strength of the anisotropy. Anisotropic friction is an effective way to control active turbulence and to direct the flow in a well-defined fashion.

Finally, we introduce a framework for continuum simulations of active nematics on deformable membranes. We demonstrate that long protrusions driven by motile topological defects are formed in three dimensions on deformable shells. This has potential implications for morphogenetic processes such as the regeneration of *Hydra*. Our results show that changes in the animal body shape can occur from solely mechanical cues.

Acknowledgements

First of all I would like to thank my supervisor, Prof. Julia Yeomans, for welcoming me into her research group, and for her continued guidance and support during these four years. I am grateful for the opportunity to explore my own interests in research, while your creativity and experience made it possible to fit topics into the bigger picture. In particular you have taught me to think critically, most of all about my own results.

For large parts of this thesis I am truly indebted to Amin Doostmohammadi, now a professor in his own right. Amin, you have provided me with an endless series of ideas and encouraged to trust my own judgement about promising directions. I am sure you will do amazing work with your new group in Copenhagen.

I would like to thank my office mates over the years, in particular Arnold Mathijssen, Matthew Andrew, Andrew Balin, Rian Hughes and Kristian Thijssen, the rest of the Yeomans group, as well as the people involved in DiStruc, Prof. Dirk Aarts in particular, for chats, ideas, and coffee breaks.

My time in Oxford would not have been the same without the friends I have made at the Oxford University Cross Country Club. I have thoroughly enjoyed the frantic lead-up to Varsity and the team spirit, as well as the horrible chat. Similar thanks have to go to friends at the Cambridge University Hare and Hounds, as well as the Greyhounds, for making me consider a Ph.D. in the UK in the first place and (hopefully) forgiving me for joining the dark side.

Finally, I would like to thank Amy for her continuous love and support. Thank you for taking the brave step to follow me to Oxford, for sharing endless cups of tea and slices of cake, and apologies for all the marathon talk.

Publications

Authored publications contributing to this thesis

- L. Metselaar, I. Dozov, K. Antonova, E. Belamie, P. Davidson, J.M. Yeomans, and A. Doostmohammadi (2017). Electric-field-induced shape transition of nematic tactoids, *Physical Review E* 96 (2), 022706.
- L. Metselaar, A. Doostmohammadi, and J.M. Yeomans (2018). Two-dimensional, blue phase tactoids, *Molecular Physics* 116:21-22, 2856-2863.
- L. Metselaar, A. Doostmohammadi, and J.M. Yeomans (2019). Topological states in chiral active matter: Dynamic blue phases and active half-skyrmions, *The Journal of Chemical Physics* 150 (6), 064909.
- L. Metselaar, J.M. Yeomans, and A. Doostmohammadi (2019). Topology and morphology of self-deforming active shells, *Physical Review Letters* (In Print).
- K. Thijssen, L. Metselaar, J.M. Yeomans, and A. Doostmohammadi (2019). Active nematics with anisotropic friction: the decisive role of the tumbling parameter, *(Sub Judice)*.

Contents

List of Figures

List of Tables

1

An introduction to (active) liquid crystals

1.1 Liquid crystals

Liquid crystals occupy an intermediate position between the crystalline and liquid phases of matter. They possess elasticity like a solid, but have liquid-like properties as well: fluidity, inability to support shear, and formation and coalescence of droplets. The name liquid crystal was first put forward by Lehmann in the early 20th century [1]. Liquid crystals typically consist of long, thin, rod-like particles. At very low temperatures or very high densities the particles occupy sites on a fixed lattice and exhibit orientational order, both over a long range (Fig. 1.1(a)). At high temperatures or low densities the orientation and position of the particles are distributed randomly, with only short-range correlations (Fig. 1.1(c)). The nematic phase sits in between these two regimes, exhibiting long-range orientational order, but only short-range positional order (Fig. 1.1(b)).

Historically, Friedel [2] proposed the classification of liquid crystals based on their structural properties. The three types he identified were nematics, cholesterics and smectics. Nematics have long-range orientational order, but no positional order. In the unstrained nematic the preferred direction is uniform throughout the material (the local, coarse-grained direction of a liquid crystal will be referred to as director). Cholesterics, like nematics, have long-range orientational order

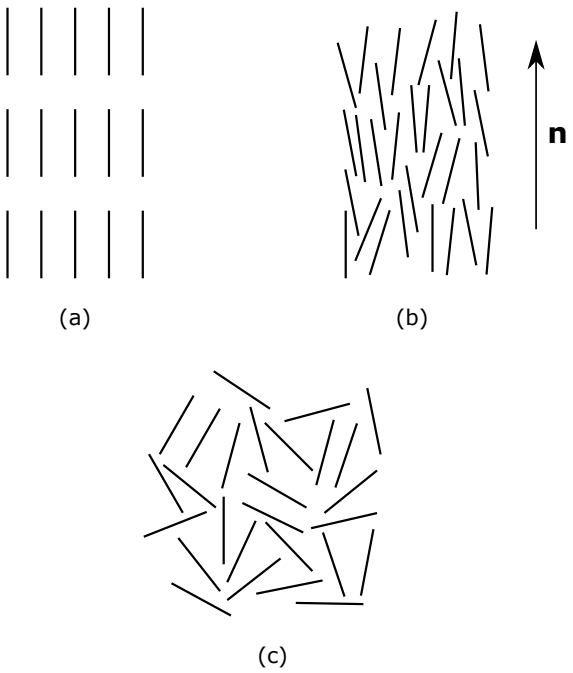

Figure 1.1: Schematic illustration of various possible phases of condensed matter. (a) Crystalline solid. (b) Liquid crystal, with the arrow $\underline{n}$ representing the local orientation of the liquid crystal. (c) Isotropic fluid.

and only short range positional order. By contrast to nematics, the preferred direction changes throughout the material in a regular fashion. A cholesteric can be described as a nematic that was originally oriented along an $\hat{x}$-axis, and then twisted around the $\hat{y}$-axis. The characteristic length scale associated with a full rotation is called the cholesteric pitch. The periodic pitch leads to a distinct "fingerprint" texture (see Fig. 1.2). There is no fundamental difference between a nematic and a cholesteric of infinite pitch. Smectics are a fundamentally different phase, and are characterised by their stratification. The particles have long-range orientational order, and tend to lie in discrete layers. The layers can freely slide over one another, and an important observation is that the diffusion in a layer is much larger than the diffusivity perpendicular to it: the energy barrier against hopping from one layer to the next is relatively large.

It could be argued, however, that the only truly crystalline liquid crystal material is a fourth type of liquid crystal: the blue phase. Blue phases possess discrete translational symmetry in three dimensions, like conventional crystals (see Fig. 1.3 for a microscope image of a single blue phase I crystal). However, the discrete

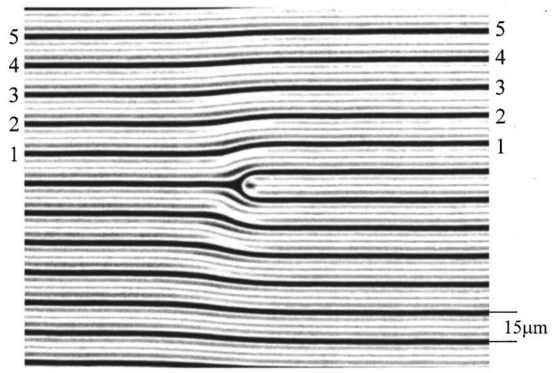

Figure 1.2: Typical appearance of the cholesteric stripe texture in a chirally doped nematic. Image taken from [3].

translational symmetry in solid crystals is due to the fixed position of molecules, whereas blue phases are liquid, the positions of molecules are disordered, and it is only the spatial pattern of molecular orientations that gives rise to the discrete translational symmetry. Frank [4] proposed that blue phases should be added as a fourth class of liquid crystals. On the other hand, if a cholesteric is defined more generally as a chiral nematic liquid, then blue phases can be considered as a generalised chiral nematic, and nematics, cholesterics and blue phases can all be described within the same framework (see for instance the phase diagrams obtained in Chapter 3 and by Duzgun et al. [5]).

The dynamics of liquid crystals cannot be considered independently of their topological structure. The blue phases are an extreme example of this, possessing symmetries that are crystallographic space groups. Here the topology is an integral part of the global structure. In general, though, it is possible to imagine a nematic completely uniform in space, but only when one does not take into account boundaries, impurities, or external fields. Take those into consideration, and topology becomes very important. A simple example would be to wrap a nematic liquid crystal over the surface of a sphere. It is not possible to unequivocally assign a preferred direction at every point on the surface: there are at least two point where the directors have to cross. A similar thing happens when a nematic is confined in a circle, where the director on the boundary is fixed to lie either parallel or perpendicular to the wall. There will be at least one point where the

Figure 1.3: Photomicrograph of monocrystals of BPI (in equilibrium with isotropic liquid) in monochromatic illumination. The crystal habit indicates cubic point symmetry, O, being a superposition of a {211} icositetrahedron and a {110} rhombic dodecahedron. The space group is the $O^8(I4_132)$ symmetry. Image taken from [6].

director cannot be defined. The points inside a nematic where the director is not properly defined are topological defects.

Since liquid crystals are liquids, and at the same time structurally anisotropic and strongly influenced by their topology, the interaction between structure, topology and flow is a physically rich field. Because liquid crystalline materials are so easily observable and can be studied with simple optical methods, they have proved a hunting ground for experimental validation of theories of broken symmetries, Goldstone modes, and, indeed, topological defects [7]. This thesis will discuss two topics concerning the interaction between flow of a passive liquid crystal material, and its structural and topological configuration. The first of these is the elongation of nematic droplets under the influence of an electric field in Chapter 2, and the second droplet shapes obtained by confining strongly chiral nematics in Chapter 3.

An example where the interaction between topology, structure and flow is maybe most pronounced is in active liquid crystals. Active nematics [8] are nematic liquid

crystals where the individual nematogens extract energy from their surroundings and convert it into mechanical work. By coarse-graining the dipolar forces it can be shown that stresses in the fluid are largest when the gradients in the director are strongest: at topological defects. In this thesis we show that chirality can prevent active turbulence (Chapter 4), that flows in active nematics can be guided by patterned surfaces (Chapter 5), and that active nematic shells will deform most strongly at the location of motile topological defects (Chapter 6).

The remainder of this introduction will deal with a more formal, free energy description of liquid crystals and topological defects, active nematics and the numerical method used in the simulations described in this thesis. Section 1.4 provides an overview of the results presented in this thesis.

1.1.1 Nematic order parameter

To quantify the nematic phase it is helpful to write down an order parameter. Taking the simplest objects that exhibit nematic order, rigid rods, the long axis of the rods can be labelled by a unit vector $\underline{b}$. Additionally, in a coarse-grained description the long-range orientational order can be captured by writing a director field $\underline{n}$, describing the local average orientation of the particles. In nematics $\underline{n}$ and $-\underline{n}$ are actually indistinguishable, meaning that the director could be more appropriately described by a line field rather than a vector field. Following the usual conventions in the literature the director will however be treated as a vector field and uniaxiality will be imposed by hand.

Taking $\underline{n}$ to be along the z-axis, $\underline{b}$ can be defined by its polar angles as $(\sin\theta\cos\phi, \sin\theta\sin\phi, \cos\theta)$. The alignment of the rods can be described by a probability distribution $f(\theta,\phi)\mathrm{d}\Omega$. Because the phase has complete cylindrical symmetry around $\underline{n}$, $f(\theta,\phi)$ is independent of ϕ and, because $\underline{n} = -\underline{n}$, $f(\theta) = f(\pi-\theta)$. The first non-zero multipole which can be used to characterise the alignment is the quadrupole, which is defined as

$$S_0 = \frac{1}{2}\langle 3\cos^2\theta - 1\rangle = \int f(\theta)(3\cos^2\theta - 1)\mathrm{d}\Omega. \tag{1.1}$$

If $f(\theta)$ is sharply peaked around $\theta = 0$ (equivalently, π), $S_0 = 1$. On the other hand, if $f(\theta)$ is randomly distributed, $S_0 = 0$. S_0, the coarse grained nematic order, is therefore a measure of alignment.

Because the director is of fixed (unit) magnitude, it cannot be used as an order parameter for the isotropic-nematic transition. This is different from ferromagnetic ordering, which is characterised by the spontaneous magnetisation, which is a vector of variable magnitude. S_0 could be an order parameter for the isotropic-nematic transition, but has the downside of not providing any information about the local director. Therefore, for the isotropic-nematic transition, a tensor order parameter is used, allowing both these properties to be conveyed.

A natural choice for the tensor order parameter is, (remembering the quadrupole for the scalar order parameter S_0,)

$$Q_{ij}(\underline{x}) = \frac{1}{N}\sum_{\alpha}\left(b_i^{(\alpha)}b_j^{(\alpha)} - \frac{1}{3}\delta_{ij}\right), \tag{1.2}$$

where the sum is over N particles in a small volume around $\underline{x}$. The tensor order parameter is symmetric and traceless, meaning that the rank two tensor contains only five independent components. The order parameter is now written in terms of the directions $\underline{b}^{(\alpha)}$ of individual molecules, not in terms of the coarse grained director $\underline{n}$. It is always possible to choose a coordinate system such that $\underline{\underline{Q}}$ can be written in diagonal form

$$\underline{\underline{Q}} = \mathrm{diag}(\lambda_1, \lambda_2, -\lambda_1 - \lambda_2). \tag{1.3}$$

The eigenvector with the largest eigenvalue is now the director $\underline{n}$. The corresponding eigenvalue is the scalar order parameter S_0 (possibly times a constant). Using this, it is possible to write $\underline{\underline{Q}}$ in terms of $\underline{n}$

$$Q_{ij} = \frac{3S_0}{2}\left(n_i n_j - \frac{1}{3}\delta_{ij}\right) + \beta\left(l_i l_j - m_i m_j\right), \tag{1.4}$$

where β is the biaxiality of the liquid crystal, and $\underline{n}$, $\underline{l}$ and $\underline{m}$ form a local orthonormal triad. In this thesis, β will be set to zero for simplicity, however, it can be important in the description of chiral liquid crystals [9].

1.1.2 Free energy of nematic liquid crystals

In thermodynamic equilibrium the nematic is at a minimum of a free energy $\mathcal{F}$. A Ginzburg-Landau theory can be constructed, where the free energy is the volume integral of a local function of $\underline{\underline{Q}}$ and its derivatives. Since the isotropic-nematic transition is only weakly first order (as already recognised by Landau [10]), the expansion may be expected to hold in a limited range in the nematic phase as well. Two sets of terms can be distinguished in the free energy density: terms containing derivatives of the order parameter make up the gradient free energy density, while terms that do not, make up the bulk free energy density.

Looking first at the bulk free energy, we expand in powers of the order parameter $\underline{\underline{Q}}$. The only rotationally invariant functions of a traceless three dimensional tensor are $\mathrm{tr}(\underline{\underline{Q}}^2)$, $\mathrm{tr}(\underline{\underline{Q}}^3)$, and functions of these two. The bulk free energy can therefore be written as

$$f_{\mathrm{bulk}} = \frac{A}{2}Q_{ij}Q_{ji} + \frac{B}{3}Q_{ij}Q_{jk}Q_{ki} + \frac{C}{4}(Q_{ij}Q_{ji})^2. \tag{1.5}$$

The expansion is usually taken far enough to ensure thermodynamic stability, but no further. To achieve stability against unbounded growth of the magnitude of the order parameter it is necessary to include terms through the fourth order in $\underline{\underline{Q}}$ in the bulk free energy, and C has to be positive. The presence of the cubic term means that the transition is first order. Note that in two dimensions the cubic term is not allowed by symmetry and the transition is second order.

For a homogeneous degree of order and a uniaxial nematic equation (1.5) can be rewritten in terms of S_0

$$f_{\mathrm{bulk}} = \frac{3A}{4}S_0^2 + \frac{B}{4}S_0^3 + \frac{9C}{16}S_0^4, \tag{1.6}$$

which is minimised by $S_0 = -\frac{B}{6C} \pm \frac{1}{2}\sqrt{\left(\frac{B}{3C}\right)^2 - \frac{8A}{3C}}$ (and, trivially, $S_0 = 0$). In this thesis the constants A, B, C are chosen to depend on η, which describes the strength of the orientation dependent interactions and the concentration of nematogens [11]. The bulk free energy is

$$f_{\mathrm{bulk}} = A_0\left(\frac{1}{2}\Big(1 - \frac{\eta}{3}\Big)Q_{ij}Q_{ji} - \frac{\eta}{3}Q_{ij}Q_{jk}Q_{ki} + \frac{\eta}{4}(Q_{ij}Q_{ji})^2\right), \tag{1.7}$$

which describes a first order, isotropic-nematic transition at $\eta = 2.7$. A_0 is a positive constant with units of energy per unit volume.

For the gradient free energy we expand in terms of derivatives of $\underline{\underline{Q}}$. The preferred state of a nematic liquid crystal is one of uniform alignment, and therefore distortions are penalised through the elastic free energy

$$\begin{aligned} f_{\text{elastic}} = &\frac{L_1}{2}(\partial_k Q_{ij})(\partial_k Q_{ij}) + \frac{L_2}{2}(\partial_j Q_{ij})(\partial_k Q_{ik}) \\ &+\frac{L_3}{2}Q_{ij}(\partial_i Q_{kl})(\partial_j Q_{kl}) + \frac{L_4}{2}\epsilon_{lik}Q_{lj}\partial_k Q_{ij}, \end{aligned} \tag{1.8}$$

where L_1, L_2, L_3 and L_4 are elastic constants. L_4 is a chiral contribution, which will be treated in more detail in subsection 1.1.5, but for now will be ignored. There is in fact a fifth rotationally invariant quantity up to second order in derivatives and second order in $\underline{\underline{Q}}$: $(\partial_i Q_{jk})(\partial_j Q_{ik})$. This term only differs from the L_2-contribution in equation (1.8) by a total derivative. When integrated, therefore, it gives a contribution differing only by a surface term. It will be disregarded here, making the implicit assumption that surface effects in the gradient free energy are small compared to bulk effects. To make sure that gradients do not become unbounded, all elastic constants have to be positive.

The elastic free energy is often written in terms of the director $\underline{n}$ and is then referred to as the Frank free energy

$$f_{\text{Frank}} = \frac{K_1}{2}(\underline{\nabla} \cdot \underline{n})^2 + \frac{K_2}{2}[\underline{n} \cdot (\underline{\nabla} \times \underline{n})]^2 + \frac{K_3}{2}[\underline{n} \times (\underline{\nabla} \times \underline{n})]^2. \tag{1.9}$$

Here K_1, K_2 and K_3 are the splay, twist and bend Frank elasticities respectively (see Fig. 1.4 for a schematic visualisation). In case of constant S_0 and pure uniaxiality the elastic constants in the tensor representation and the Frank elastic constants can be directly mapped

$$L_1 = \frac{1}{9S_0^2}(-K_1 + 2K_2 + K_3), \tag{1.10a}$$

$$L_2 = \frac{4}{9S_0^2}(K_1 - K_2), \tag{1.10b}$$

$$L_3 = \frac{2}{9S_0^3}(-K_1 + K_3). \tag{1.10c}$$

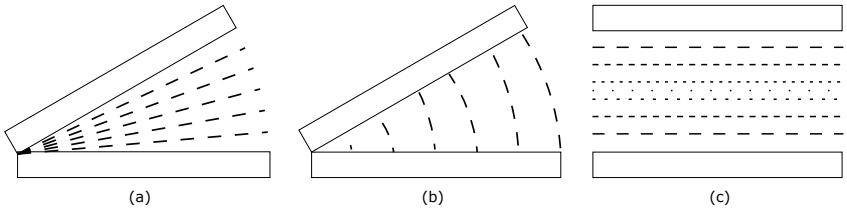

Figure 1.4: The three types of deformation occurring in nematics. (a) Splay. (b) Bend. (c) Twist (shorter line segments mean that the director is pointing more strongly out of the paper).

Only a single cubic term is included in the expansion in terms of $\underline{\underline{Q}}$ (equation 1.8), while in reality there are seven. Including all of them would lead to overfitting when mapping to the elastic constants in the director description, and in order to model a nematic with different splay and bend elasticity it is sufficient to only include the L_3-term. A common choice is to set $L_1 = L$ and $L_2 = L_3 = 0$, thus having the splay, twist and bend elastic constants equal ($K_1 = K_2 = K_3 = K$): the one-elastic-constant approximation.

The nematic liquid crystal can be coupled to an electric field by a free energy contribution

$$f_{\text{electric}} = -\epsilon_a E_i Q_{ij} E_j, \tag{1.11}$$

where $\underline{E}$ is the electric field and ϵ_a the dielectric anisotropy.

A preferred orientation at a confining surface can be imposed by an anchoring free energy [12]

$$f_{\text{anchoring}} = \frac{W_{\text{uniform}}}{2}(Q_{ij} - Q^0_{ij})^2, \tag{1.12}$$

where Q^0_{ij} is the chosen orientation and W_{uniform} is the anchoring strength. Anchoring perpendicular to a confining surface is referred to as homeotropic, while parallel anchoring is called planar. The formulation in equation (1.12) sets the preferred director unequivocally. It is however also possible to impose degenerate anchoring, that is, only describing the tilt angle with respect to a surface. For a in-plane director orientation the degenerate anchoring free energy is [13]

$$f_{\text{degenerate}} = W_1^{\text{deg}}(\tilde{Q}_{ij} - \tilde{Q}^{\perp}_{ij})^2 + W_2^{\text{deg}}\left(\tilde{Q}_{ij}\tilde{Q}_{ji} - \frac{9}{4}S^2_{\text{surf}}\right)^2. \tag{1.13}$$

The tensor $\tilde{Q}_{ij}$ is defined as $Q_{ij} + \frac{S_0}{2}\delta_{ij}$. $\tilde{Q}_{ij}$ is projected onto a surface with normal $\underline{a}$ as $\tilde{Q}^{\perp}_{ij} = (\delta_{ik} - a_i a_k)\tilde{Q}_{kl}(\delta_{lj} - a_l a_j)$. The first term in equation (1.13) favours in-plane director orientation, with strength W_1^{deg}. The second term prefers the strength of the order on the surface to be S_{surf}. When the surface ordering strength is required to be S_0, this term can be omitted.

1.1.3 Free energy of lyotropic nematic liquid crystals

The free energy description in subsection 1.1.2 deals with a thermotropic liquid crystal. However, there are many cases where it is interesting to study a liquid crystalline material in coexistence with an isotropic fluid, be that its own isotropic phase due to phase coexistence, or a different second fluid. Examples include active nematic drops [14], active nematic shells [15], hexagonal structures of isotropic drops at the liquid crystal-air interface [16], bacterial colonies [17] and changes in stripe patterns in cholesteric shells [18].

In this thesis the two phases are treated as a binary fluid, which is modelled by writing the liquid crystal concentration as a field ϕ. Contributions to the free energy that have to be considered are a mixing free energy, that phase separates the two binary fluid components, and contributions from the resulting interfaces. In order to make only one of the two fluids nematic, η in equation (1.7) is chosen to be dependent on the liquid crystal concentration.

For the binary fluid term any double-well potential would be allowed. The choice used in this thesis is

$$f_{\text{mix}} = \frac{A_\phi}{2}\phi^2(1-\phi)^2, \tag{1.14}$$

where A_ϕ is a positive constant. This gives two equilibria at $\phi = 0, 1$, corresponding to complete phase ordering.

A smooth concentration profile across an interface is ensured by including a term

$$f_{\text{interface}} = \frac{k_\phi}{2}(\partial_i \phi)^2, \tag{1.15}$$

with k_ϕ again a positive constant. It provides for a non-zero interfacial tension σ, and tends to minimise the interfacial area. A drop of one fluid emulsified in

another fluid will tend to form a spherical (circular in two dimensions) droplet. A flat interface, on the other hand, will tend to remain flat.

The coupling between the director and the fluid interface is modelled by

$$f_{\text{coupling}} = L_0 \partial_i \phi Q_{ij} \partial_j \phi, \tag{1.16}$$

where $L_0 > 0$ encourages the director to lie parallel to the interface, and $L_0 < 0$ encourages perpendicular alignment [19].

Finally, the bulk nematic free energy is made dependent on the liquid crystal concentration field ϕ by writing $\eta(\phi) = \eta_0 + \eta_s(\phi - \bar{\phi})$, where η_0, η_s and $\bar{\phi}$ are constants that can be tuned to change the location of the isotropic-nematic transition. Remember that the first-order, isotropic-nematic transition occurs at $\eta = 2.7$. Choosing parameters such that $\eta < 2.7$ for $\phi = 0$ and $\eta > 2.7$ for $\phi = 1$ ensures that the $\phi = 0$ fluid is in the isotropic phase, while the $\phi = 1$ fluid is in the nematic phase.

1.1.4 Topological defects

The tensor description of the director field is particularly useful in the presence of topological defects. When polarised light is passing through a liquid crystal put between crossed polarisers, light will, or will not, pass through depending on the local orientation of the liquid crystal director. This is the source of the well-known Schlieren textures (Fig. 1.5). The dark brushes correspond to the extinction direction of the liquid crystal. The points where two or four dark brushes meet correspond to singularities in the director field. These are topological defects: locations where the director cannot be properly defined.

The discontinuities can be located in a point (point defects), on a line (disclination lines or loops), or on a sheet (walls). In nematics only point defects and disclination lines are present. All work presented in this thesis will be concerned with two-dimensional nematics (sometimes with the director allowed to move in three dimensions, sometimes on curved surfaces), and it is therefore sufficient to consider only point defects. The defect strength can be classified by a winding number

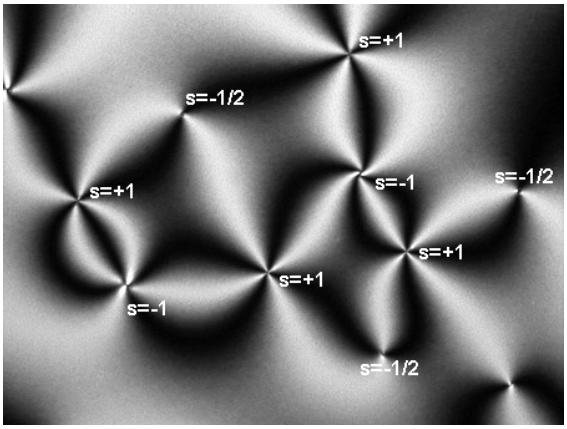

Figure 1.5: Schlieren texture in a nematic liquid crystal. Topological defects are labelled with their respective charges. Image taken from B. Senyuk's personal website.

s, which can be written as

$$s = \frac{1}{2\pi} \oint_S \mathrm{d}\theta, \tag{1.17}$$

where S is a loop in a two-dimensional plane and the director field is written as $\underline{n} = (\cos\theta, \sin\theta)$, with θ the polar angle. The winding number measures how many times the director rotates along a contour taken around the defect core. Fig. 1.6 shows a schematic representation of some of the allowed defects in a two-dimensional nematic liquid crystal. Note that the $s = \pm 1$ (Fig. 1.6(a) and (b)) defects are not topologically protected: these director fields can be continuously transformed to a uniform structure, but only when the director is allowed to move out of plane. This is not true for the $s = \pm 1/2$ (Fig. 1.6(c) and (d)) defect cores: the only way these defects can be removed is by annihilation of two oppositely charged defects.

The topological strength of the defect structures can be related to the Schlieren textures in Fig. 1.5. The charge of defects is the number of brushes that meet times $\pm 1/4$. The appearance of points where two brushes meet is evidence that liquid crystals are apolar: a rotation through π maps the director onto itself. In a polar liquid $\underline{n}$ and $-\underline{n}$ are different, and the director field will only match after rotations through 2π. Thus, in polar fluids only integer defects are possible.

It is important to note that topological defects in the Frank elastic framework carry infinite elastic energy. In the one-elastic-constant approximation the director

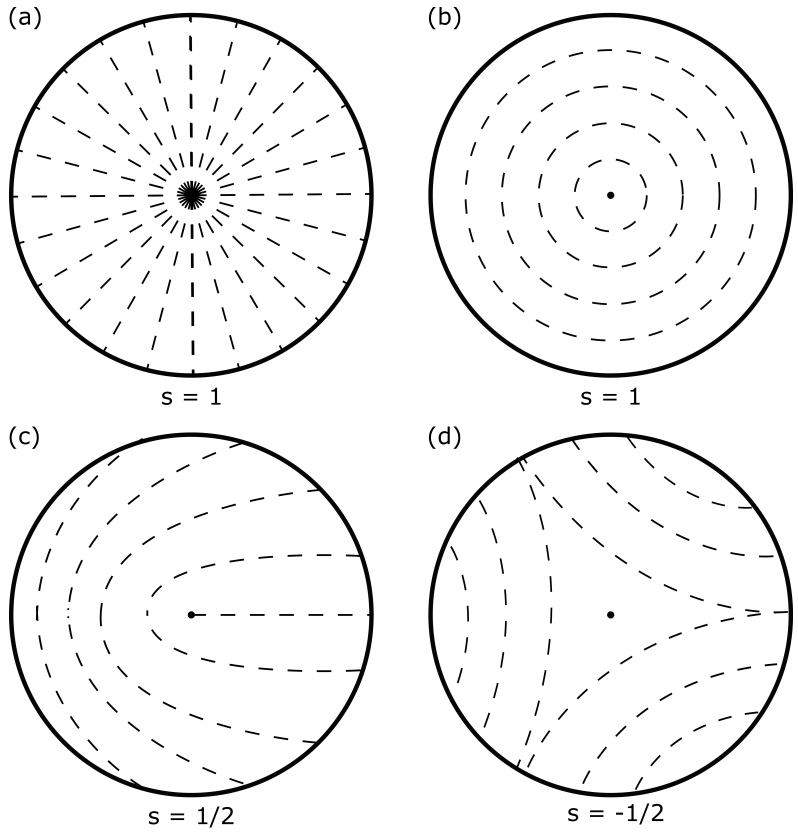

Figure 1.6: Schematic illustration of topological defects in nematic liquid crystals. (a) $s = 1$, splay-type, (b) $s = 1$, bend-type, (c) $s = 1/2$, and (d) $s = -1/2$. The director is exclusively confined to the plane of the page in all cases, and the location of the defect core is indicated by a black point.

field around a strength s defect core can be written as $(\cos(s\theta + \gamma), \sin(s\theta + \gamma))$, where γ is an arbitrary constant. The energy of this director field configuration per unit length of the disclination line (a line achieved by extending the point defect in the third dimension) can be written as $\pi K s^2 \ln(R/d)$, where d is a short distance cut-off taken as the size of the defect core, and R is a long distance cut-off which indicates the distance to boundaries or other defects [20]. In case of $s = \pm 1$ topological charges it is possible to avoid this infinite elastic energy by allowing the director to "escape into the third dimension", which means it will be directed perpendicular to the plane at the defect core and will not create a singularity. As shown by Cladis and Kleman [21], lines with integer charge are unstable for all physical sample sizes (except when K_1 is much smaller than K_3).

When considering point defects in two dimensions, the director escaping into the

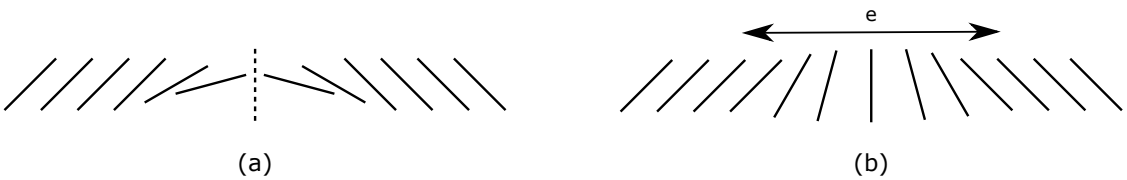

Figure 1.7: Smearing out of a defect wall. (a) Configuration with a sheet discontinuity present, indicated by the dashed line. (b) The discontinuity has been transformed to an elastic deformation over a length e.

third dimension will still lead to a charge coming from a calculation of the winding number: so even though there is no singular point, the charge is still conserved. This will be important for the two-dimensional blue phases in Chapters 3 and 4. For purely two-dimensional systems, where the director is confined to the plane, "escape into the third dimension" is not available. The issue of avoiding infinite energy is resolved by letting the magnitude of the order go to zero at the defect core. At the defect core the liquid crystal is therefore no longer in the nematic phase, but in the isotropic phase. This is an effect that is nicely captured in the tensorial description of the director field: at the defect core, S_0 goes to zero.

Walls (see Fig. 1.7(a)) are not allowed in nematics for energetic reasons: smearing out the wall over a distance e (Fig. 1.7(b)) is energetically favourable [7, 20]. The wall discontinuity carries an energy per unit area of the order of U/a^2, where U is a molecular binding energy and a is a molecular distance. Transforming the discontinuity into an elastic distortion over a length e, the energy will be of the order of $Ke/e^2 \approx U/ea \ll U/a^2$. Transforming the defect wall to an elastic distortion is favourable and allowed, and will leave behind at most some disclination lines and point defects.

1.1.5 Cholesteric blue phases

Blue phases are found in highly chiral liquid crystals in a narrow temperature window between the isotropic and the cholesteric phase. Key to understanding the properties of blue phases is the notion that the locally preferred ordering in a chiral liquid crystal is one of double twist, as opposed to the single twist found in a cholesteric helix [9]. Such a double-twisted configuration can be viewed in Fig. 1.8(a). Multiple

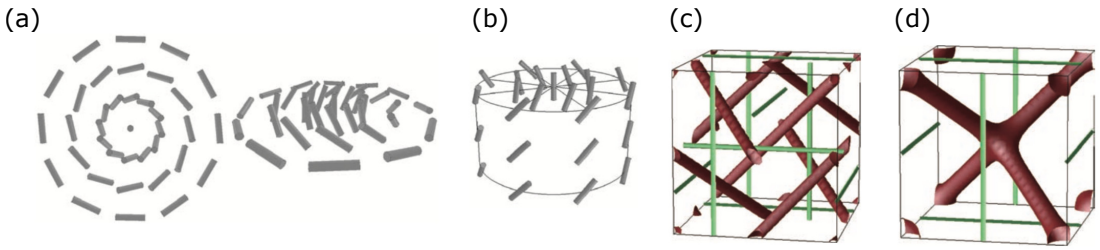

Figure 1.8: Schematic illustration of the structures of a half-skyrmion and bulk blue phases. (a) A half-skyrmion viewed from the top and the side. The director twists through $\pi/2$ from the centre to the side. (b) A double-twist cylinder taken from a bulk blue phase. The director twists in all directions perpendicular to the vertical axis, up to $\pi/4$. (c) Blue phase I. (d) Blue phase II. Image taken from [22].

of these double-twisted regions can be joined together in a hexagonal fashion to generate a two-dimensional lattice. It is clear, however, that is not possible to do so without introducing topological defects. At the vertices of the hexagonal lattice $s = -1/2$ topological defects are generated, creating frustration in the system.

In three dimensions the double-twist cylinders only twist through an angle $\pi/4$ (Fig. 1.8(b)), and will form three-dimensional regular stacks, interleaved with disclination lines. In Fig. 1.8(c) and (d) we show the structures of two bulk blue phases with cubic symmetry. Blue phase I in Fig. 1.8(c) is characterised by the space group $O^8(I4_132)$, and contains straight disclination lines that do not intersect each other. Blue phase II in Fig. 1.8(d) is characterised by the space group $O^2(P4_232)$ and the disclination lines form a double-diamond structure with an array of four-arm junctions. The $\pi/4$ rotation in the double-twist cylinder means that the director field remains continuous at the point of contact between two neighbouring orthogonal cylinders.

In condensed matter physics, it is common to talk about double-twisted regions as vortex-like excitations without a singularity at their centre. This is based on work by Skyrme [23], which showed that particle-like topological excitations can be stable in certain types of continuous nonlinear fields. A skyrmion is a localised variation of the field, and the topological skyrmion number is defined as

$$N = \frac{1}{4\pi} \int dxdy \underline{n} \cdot \left(\frac{\partial \underline{n}}{\partial x} \times \frac{\partial \underline{n}}{\partial y} \right). \tag{1.18}$$

In this language, the double-twist cylinders in the blue phases of chiral liquid crystals have a topological skyrmion number of 1/2 (for hexagonal lattices, Fig. 1.8(a)) or 1/4 (for three-dimensional cubic lattices, Fig. 1.8(b)).

To include cholesterics and blue phases in our free energy description we keep the chiral term in the elastic free energy (equation (1.8))

$$f_{\text{elastic}} = \frac{L_1}{2}(\partial_k Q_{ij})(\partial_k Q_{ij}) + \frac{L_2}{2}(\partial_j Q_{ij})(\partial_k Q_{ik}) + 2\frac{2\pi}{\lambda}L_1\epsilon_{lik}Q_{lj}\partial_k Q_{ij}. \tag{1.19}$$

It is convenient to write the elastic free energy slightly differently, combining the term linear in gradients with the $(\nabla \underline{\underline{Q}})^2$ term by completing the square

$$f_{\text{elastic}} = \frac{L_2}{2}\left(\partial_i Q_{ji}\right)^2 + \frac{L_C}{2}\left(\epsilon_{kli}\partial_k Q_{jl} + 2\left(\frac{2\pi}{\lambda}\right)Q_{ij}\right)^2, \tag{1.20}$$

where L_C is an elastic constant. The elastic free energy in equation (1.20) is identical to the expression in equation (1.19) up to total derivatives and a $\text{tr}(\underline{\underline{Q}}^2)$ term, which can be included in the bulk free energy density. The parameter λ gives the pitch length and is related to the chirality of the cholesteric helix (we will consider $\lambda > 0$ corresponding to right-handed chirality). The limit $\lambda^{-1} = 0$ and $L_C = L_2$ gives a nematic liquid crystal within the one-elastic-constant approximation.

Conveniently, having written the elastic free energy in the form (1.20), the minimisers can be found by solving a first order differential equation

$$Q_{ij} = -(\lambda/4\pi)\epsilon_{kli}\partial_k Q_{jl}. \tag{1.21}$$

The solution of equation (1.21)

$$Q_{ij} \sim \begin{pmatrix} 0 & 0 & 0 \\ 0 & \cos 4\pi x/\lambda & \sin 4\pi x/\lambda \\ 0 & \sin 4\pi x/\lambda & -\cos 4\pi x/\lambda \end{pmatrix} \tag{1.22}$$

is a biaxial helix, with the helical axis along the x-direction. The direction of the helical axis is arbitrary, and since equation (1.21) is linear, any linear combination of biaxial helices is also a solution. This gives rise to the double-twist cylinders in the blue phases.

1.1.6 Nematohydrodynamics

Flow of Newtonian fluids already gives rise to a wealth of phenomena. However, for liquid crystals the coupling between the fluid flow and the orientational motion of the nematogens has to be taken into account as well. This coupling works both ways: typically, flows disturb alignment. On the other hand, the reorientation following a distortion in the orientational field is generally accompanied by a flow. The hydrodynamics of liquid crystals in terms of a director field $\underline{n}(\underline{x})$ and a velocity field $\underline{u}(\underline{x})$ was written down by Ericksen in the early 1960s [24, 25], and further developed by Leslie [26, 27] and Parodi [28].

Edwards, Beris and Grmela [29–31] have subsequently developed a theory for coupling between the nematic director and the fluid velocity in terms of the tensor order parameter $\underline{\underline{Q}}$. The advantage of this over the Leslie-Ericksen approach is that the strength of the order is allowed to vary, whereas the director formulation only allows for reorientation and therefore cannot take account of defects, or flow-induced ordering.

1.1.6.1 Beris-Edwards formulation

The order parameter $\underline{\underline{Q}}$ evolves according to a Ginzburg-Landau equation, but taking into account advection with the flow

$$\left(\frac{\partial}{\partial t} + u_k \partial_k\right) Q_{ij} - S_{ij} = \Gamma_Q H_{ij}, \tag{1.23}$$

where $\underline{\underline{H}}$ on the right-hand side is the molecular field and Γ_Q is a rotational diffusivity constant. The first two terms on the left-hand side correspond to the material derivative and describe the time dependence of a quantity advected by a flow with velocity $\underline{u}$. This is generalised for a nematic by the co-rotational term $\underline{\underline{S}}$, which describes how the order parameter tensor $\underline{\underline{Q}}$ responds to flow gradients.

$$\begin{aligned} S_{ij} = (\xi D_{ik} + \Omega_{ik})\left(Q_{kj} + \frac{\delta_{kj}}{3}\right) - \left(Q_{ik} + \frac{\delta_{ik}}{3}\right)(\xi D_{kj} - \Omega_{kj}) \\ -2\xi\left(Q_{ij} + \frac{\delta_{ij}}{3}\right) Q_{kl} W_{kl}, \end{aligned} \tag{1.24}$$

Interpretation	**Combination**
Viscosity ν_1 parallel to velocity $\underline{u}$	$(\alpha_3+\alpha_4+\alpha_6)/2$
Viscosity ν_2 parallel to velocity gradient $\underline{\nabla u}$	$(-\alpha_2+\alpha_4+\alpha_5)/2$
Viscosity ν_3 orthogonal to both $\underline{u}$ and $\underline{\nabla u}$	$\alpha_4/2$
Shear viscosity ν_{12}	α_1
Rotational viscosity γ_1	$\alpha_3-\alpha_2$
Torsion coefficient γ_2	$\alpha_3+\alpha_2$
Splay viscosity ν_{splay}	$\gamma_1-\alpha_3^2/\nu_1$
Twist viscosity ν_{twist}	γ_1
Bend viscosity ν_{bend}	$\gamma_1-\alpha_2^2/\nu_2$

Table 1.1: Interpretation of Leslie viscosity coefficients.

where $D_{ij} = (W_{ij}+W_{ji})/2$ and $\Omega_{ij} = (W_{ij}-W_{ji})/2$ are the symmetric and antisymmetric parts of the velocity gradient tensor $W_{ij} = \partial_j u_i$ respectively. ξ is a constant, the "tumbling parameter", which depends on the molecular details of the liquid crystal under consideration. It is linked to the alignment parameter λ defined in the Ericksen-Leslie-Parodi framework by $\lambda = \frac{3S_0+4}{9S_0}\xi$. In strong flows, the director will tend to align at the Leslie angle, such that the torque experienced by a particle vanishes. Without other constraints, the Leslie angle is given by $\lambda = 1/(\cos 2\theta_L)$. The alignment parameter is defined in terms of the Leslie coefficients by $\lambda = -\gamma_2/\gamma_1$, where $\gamma_1 = \alpha_3-\alpha_2$ and $\gamma_2 = \alpha_2+\alpha_3 = \alpha_6-\alpha_5$, and reflects the shape of the molecules. The coefficients α_i are the Leslie coefficients, and there are five independent ones. The interpretation of the various combinations of the Leslie viscosity coefficients is summarised in Table 1.1. For $|\lambda| < 1$ (or $|\xi| < \frac{9S_0}{3S_0+4}$) the liquid crystal is in the flow-tumbling regime, since the hydrodynamic torque does not vanish and can cause continuous changes in the director orientation. For $|\lambda| > 1$ (or $|\xi| > \frac{9S_0}{3S_0+4}$) the liquid crystal is in the flow-aligning regime.

The order parameter field $\underline{\underline{Q}}$ must evolve in such a way that the free energy is minimised, but at the same time has to remain traceless under time evolution. To that end, the molecular field $\underline{\underline{H}}$ is defined as

$$H_{ij} = -\frac{\delta \mathcal{F}}{\delta Q_{ij}} + \frac{1}{3}\frac{\delta \mathcal{F}}{\delta Q_{kk}}\delta_{ij}, \tag{1.25}$$

where the second term ensures that $\underline{\underline{Q}}$ remains traceless.

1.1.6.2 Cahn-Hilliard equation

The second order parameter ϕ evolves according to the Cahn-Hilliard convection-diffusion equation [32]

$$\frac{\partial \phi}{\partial t} + \partial_i \left(u_i \phi \right) = M \nabla^2 \mu, \tag{1.26}$$

where M is the mobility and μ is the chemical potential

$$\mu = \frac{\delta \mathcal{F}}{\delta \phi} = \frac{\partial \mathcal{F}}{\partial \phi} - \partial_i \frac{\partial \mathcal{F}}{\partial (\partial_i \phi)}. \tag{1.27}$$

Phase equilibrium requires that the chemical potential is constant. Using the Laplacian of the chemical potential on the right hand side of equation (1.26) ensures that the liquid crystal concentration ϕ is conserved.

1.1.6.3 Navier-Stokes equations

The velocity field $\underline{u}$ evolves according to the generalised Navier-Stokes equations

$$\frac{\partial \rho}{\partial t} + \partial_i (u_i \rho) = 0, \tag{1.28}$$

$$\rho \left(\frac{\partial u_i}{\partial t} + u_j \partial_j u_i \right) = -\partial_i p + \partial_j \Sigma_{ij}, \tag{1.29}$$

$$\begin{aligned} \Sigma_{ij} = 2\nu D_{ij} + 2\xi \left(Q_{ij} + \frac{\delta_{ij}}{3} \right) Q_{kl} H_{kl} - \xi H_{ik} \left(Q_{kj} + \frac{\delta_{kj}}{3} \right) \\ -\xi \left(Q_{ik} + \frac{\delta_{ik}}{3} \right) H_{kj} + Q_{ik} H_{kj} - H_{ik} Q_{kj} \\ -\partial_i Q_{kl} \frac{\delta \mathcal{F}}{\delta \partial_j Q_{kl}} + (\mathcal{F} - \phi \mu) \delta_{ij} - \partial_i \phi \left(\frac{\delta \mathcal{F}}{\delta \partial_j \phi} \right), \end{aligned} \tag{1.30}$$

where ρ is the fluid density, p is the pressure, and ν is the viscosity. Equation (1.28) is mass conservation, and equation (1.29) conservation of momentum. In equation (1.30) for $\underline{\underline{\Sigma}}$ the first term is the viscous stress. The symmetric part of the elastic stress $\underline{\underline{\sigma}}$ is

$$\sigma_{ij} = 2\xi \left(Q_{ij} + \frac{\delta_{ij}}{3} \right) Q_{kl} H_{kl} - \xi H_{ik} \left(Q_{kj} + \frac{\delta_{kj}}{3} \right) - \xi \left(Q_{ik} + \frac{\delta_{ik}}{3} \right) H_{kj}, \tag{1.31}$$

while the antisymmetric part is

$$\tau_{ij} = Q_{ik} H_{kj} - H_{ik} Q_{kj}. \tag{1.32}$$

Both these expressions are a consequence of the liquid crystalline order and were derived phenomenologically. The last line introduces the bulk pressure $\phi\mu - \mathcal{F}$, a well-known thermodynamic relation. The $\partial_i Q_{kl} \frac{\delta \mathcal{F}}{\delta \partial_j Q_{kl}}$ and $\partial_i \phi \left(\frac{\delta \mathcal{F}}{\delta \partial_j \phi} \right)$ contributions stem from interparticle forces: they tell the fluid how to move to reduce free energy stored in distortions in the nematic tensor field and liquid crystal concentration field respectively. The total stress tensor $\underline{\underline{\Sigma}}$ can be symmetrised using the procedure described in [33], which implies that angular momentum is conserved.

These combined equations (1.23−1.30) are used throughout the thesis to calculate the evolution of the nematic order and the flow. In order to do this, the hybrid lattice Boltzmann method is used, which will be discussed in section 1.3.

1.2 Active liquid crystals

We now describe the properties of active materials. The term active matter is used to describe materials that extract energy from their surroundings at the single particle level and convert it to mechanical work. Experimental examples include cytoskeletal networks, bacterial suspensions, cell colonies, Janus catalysts and vibrated granular rods. The continuous injection of energy can lead to phenomena such as collective motion [34], pattern formation [14, 35, 36], topological defects [15, 37, 38], and active turbulence [39, 40]. Fig. 1.9 shows examples of biological systems where topological defects are continually created. Several theoretical frameworks have been developed over the years to study these types of collective behaviour. The goal is to mimic the behaviour of natural materials in a controlled manner to grasp the mechanisms at work. A well-studied class of active matter, which includes for instance elongated bacteria and filamentous particles inside cells, can be simplified to rod-like particles. It bears resemblance to nematic liquid crystals, which consist of thin, elongated particles, exhibiting long-range orientational order. The systems are modelled as an “active nematic”, writing equation of motions depending only on the symmetries of the system. There is an important difference with passive nematic liquid crystals: the activity in the active materials leads to continuous creation and annihilation of topological defects, destroying the long-range orientational order.

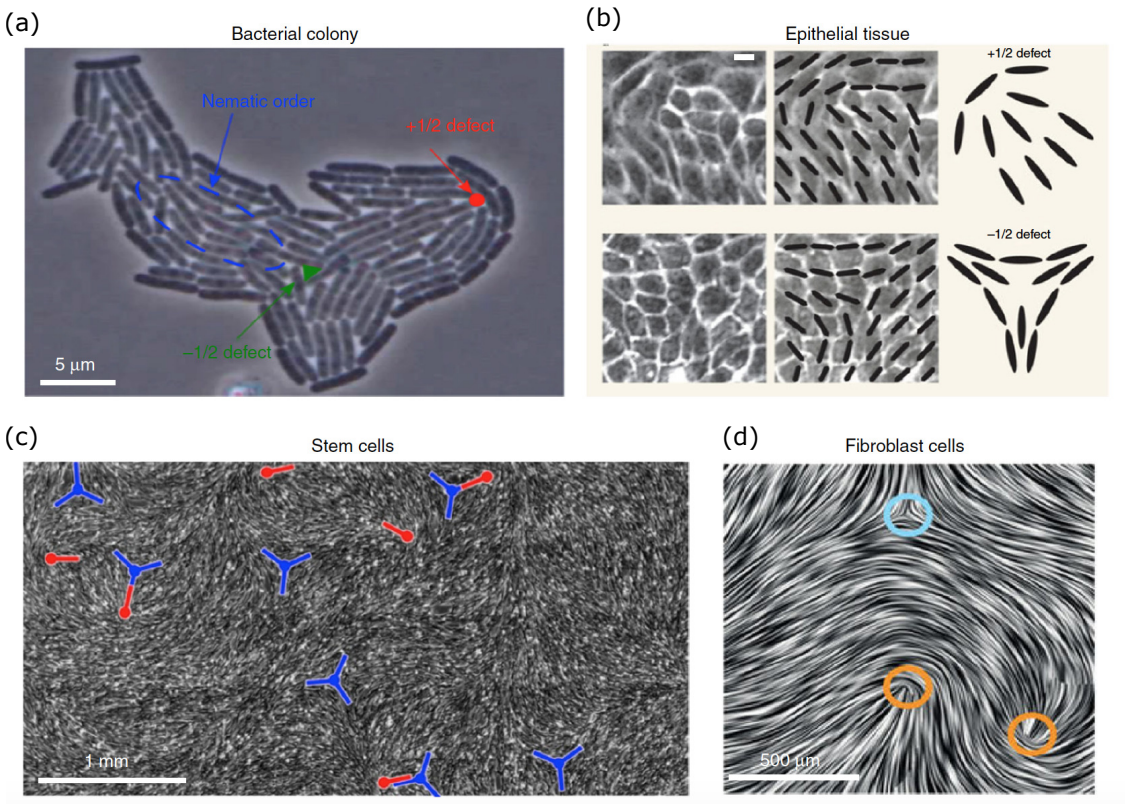

Figure 1.9: Topological defects in active biological systems. (a) Growing colony of E. coli bacteria [41]. The motion of $+1/2$ defects towards the growing interface can lead to shape changes of the colony. (b) Epithelial tissue of Madine-Darby canine kidney (MDCK) cells. Scale bar is 10 μm [38]. Strong correlations between the position of $+1/2$ defects and cell death and extrusion have been reported. (c) Monolayer of neural progenitor stem cells [42]. Cells are depleted from $-1/2$-defects (blue, trefoil symbols) and accumulate at $+1/2$ ones (red, comet-like symbols). (d) Dense monolayer of mouse fibroblast cells [43] showing $-1/2$ and $+1/2$ topological defects marked by blue and orange circles, respectively. Image taken from [8].

1.2.1 Active stress

The idea behind modelling active materials consisting of self-propelling rod-like particles as an active nematic is that the dipolar flow fields generated by each of the particles can be coarse grained [44, 45] and incorporated in the stress in the generalised Navier-Stokes equation (1.29). In any momentum conserving system the equation of motion for the momentum density $\rho\underline{u}$ is given by

$$\partial_t(\rho u_i) = -\partial_j \sigma_{ij}, \tag{1.33}$$

where $\underline{\underline{\sigma}}$ is the stress tensor. By Newton's Third Law, the forces exerted by a self-propelled particle on the fluid and the forces exerted by the fluid on the

self-propelled particle are equal and opposite. In the equation of motion for the momentum density $\rho\underline{u}$ the force density associated with each self-propelled particle and the surrounding fluid must therefore integrate to zero. The simplest model is for rod α to have equal and opposite forces $\underline{f}$ at its ends, oriented along the director, while the position and orientation are encoded in the director $\underline{n}_\alpha(\underline{x},t)$. For a collection of self-propelled particles at locations $\underline{x}_\alpha(t)$ and with ends at $\underline{x}_\alpha + a\underline{n}_\alpha$ and $\underline{x}_\alpha - a\underline{n}_\alpha$, this yields a force density

$$-\partial_j \cdot \sigma_{ij}^{\text{active}} = f_i^{\text{active}} = f\sum_\alpha n_{\alpha i}(t)\left[\delta(\underline{x}-\underline{x}_\alpha(t)-an_{\alpha i}) - \delta(\underline{x}-\underline{x}_\alpha(t)+an_{\alpha i})\right]. \tag{1.34}$$

Expanding the delta functions in equation (1.34) yields

$$f_i^{\text{active}} = -af\partial_j \sum_\alpha n_{\alpha i}n_{\alpha j}\delta(\underline{x}-\underline{x}_\alpha) + O(\nabla\nabla). \tag{1.35}$$

In a coarse grained description this gives

$$\sigma_{ij}^{\text{active}} = afc(\underline{x},t)\left(n_i n_j - \frac{1}{3}\delta_{ij}\right) + O(\nabla), \tag{1.36}$$

where $c(\underline{x},t)$ is the concentration of self-propelled particles. As usual in active nematics, the concentration will be assumed to be constant, and all other constants can be taken together in an activity constant ζ controlling the strength of the activity to arrive at

$$\sigma_{ij}^{\text{active}} = -\zeta Q_{ij}. \tag{1.37}$$

Depending on the sign of the activity constant ζ two distinct modes of self-propulsion can be recognised: $\zeta < 0$ corresponds to contractile (puller) particles that pull in fluid along their length and expel it to the sides, while $\zeta > 0$ corresponds to extensile (pusher) particles that drag in fluid from the sides and push it out along their length. Introducing this active stress in the stress equation (1.30) means that the machinery from studies of passive nematics will be available for the case of active nematics.

1.2.2 Defects in active liquid crystals

Many of the interesting dynamics in active nematics have to do with the behaviour of active defects, which is markedly different from defects in passive nematics. In passive nematics it is well established that the motion of a single defect governed by the Beris-Edwards equations can be modelled by an overdamped equation

$$\mu\left(\frac{\mathrm{d}x_i}{\mathrm{d}t} - u_i\right) = F_i, \tag{1.38}$$

where μ is an effective drag coefficient proportional to Γ_Q^{-1}, $\underline{x}$ is the location of the defect, $\underline{u}$ is the local fluid velocity, and $\underline{F}$ is the sum of all forces acting on the defect. As seen in subsection 1.1.4 the lowest energy configuration for a single defect is given by the director field $\underline{n} = (\cos s\phi, \sin s\phi)$. Following the procedure used by Denniston et al. [46], for small deformations the total force $\underline{F} = -2\pi sK\nabla_\perp\theta_{\text{excess}}$, with $\nabla_\perp = (-\partial_y, \partial_x)$, θ_{excess} the departure from the optimal defect configuration, and

$$\mu = \pi\Gamma_Q^{-1}s^2\int_{Er}^{\inf} K_1^2(x)I_1(2x)\mathrm{d}x \approx 226\pi\Gamma_Q^{-1}s^2, \tag{1.39}$$

where K_1 and I_1 are Bessel functions and $Er = \Gamma_Q^{-1}a|\dot{\underline{x}}|/K$ is the Ericksen number, the ratio of the viscous to the elastic forces, at the scale of the defect core.

In active systems it is assumed that the dynamics of the flow is much faster than the orientational dynamics of the director field, and the force $\underline{F}$ in equation (1.38) can be neglected. In this case the flow velocity can be calculated from the Stokes equation with force $\underline{f} = \underline{f}^{\text{active}} + \underline{f}^{\text{elastic}}$

$$\nu\nabla^2 u_i - \partial_i p = -f_i, \quad \partial_i u_i = 0. \tag{1.40}$$

The solution can be expressed as the convolution of the two-dimensional Oseen tensor with the force per unit area (moving to radial coordinates)

$$u_i(\underline{r}) = \int \mathrm{d}A' G_{ij}(\underline{r} - \underline{r}')f_j(\underline{r}'), \tag{1.41}$$

where the two-dimensional Oseen tensor G_{ij} [47] is

$$G_{ij}(\underline{r}) = \frac{1}{4\pi\nu}\left[\left(\log\frac{\mathcal{L}}{r} - 1\right)\delta_{ij} + \frac{r_i r_j}{r^2}\right], \tag{1.42}$$

with $\mathcal{L}$ a length scale set to recover the desired behaviour at the boundary. From the coarse-grained description in equation (1.37) the active force for $+1/2$ and $-1/2$-defects can be calculated as

$$\underline{f}^{\text{active}} = -\frac{\zeta}{2r}\begin{cases}\hat{x}, & s=+1/2\\ -cos2\phi\hat{x}+\sin 2\phi\hat{y}, & s=-1/2.\end{cases} \tag{1.43}$$

The symmetry axis is chosen to be $\hat{x}$, and the order $S_0 = 1$ everywhere. Inserting the force into the Stokes equation yields the velocity profiles

$$\underline{u}_+(r,\phi) = -\frac{\zeta}{12\nu}\left[(3(R-r)+r\cos 2\phi)\hat{x} + r\sin 2\phi\hat{y}\right], \tag{1.44a}$$

$$\begin{aligned}\underline{u}_-(r,\phi) = -\frac{\zeta r}{12\nu R}\Big[&\left(\left(\frac{3}{4}r-R\right)\cos 2\phi - \frac{R}{5}\cos 4\phi\right)\hat{x}\\ &+\left(\left(\frac{3}{4}r-R\right)\sin 2\phi - \frac{R}{5}\sin 4\phi\right)\hat{y}\Big].\end{aligned} \tag{1.44b}$$

Setting $\underline{u} = \underline{u}_+(0,\phi)$ shows that active $+1/2$-defects self-propel along their symmetry axis with constant speed $u_0 = \zeta R/(4\nu)$. Active $-1/2$-defects on the other hand give $\underline{u}_-(0,\phi) = 0$, so these are only moved by elastic deformations or background flows. The self-propelling nature of $+1/2$-defects leads to interesting interactions between oppositely charged defects pairs, summarised in Fig. 1.10. Depending on the relative orientation, and on the extensile or contractile nature of the activity, oppositely charged defects can overcome the elastic attraction or repulsion, leading to effective interactions.

1.2.3 Active turbulence

The relative motion of oppositely charged defects plays an important role in the dynamics of an active nematic. From linear stability analysis it follows that a two-dimensional active nematic is unstable to bend (splay) deformations of the director field for any extensile (contractile) active strength [44]. Distortions created by the hydrodynamic instabilities tend to localise in lines of high distortion [48], with a characteristic length scale $l_{\text{active}} \sim \sqrt{L/\zeta}$, which is found by balancing the elastic stress $\sim L/l^2$ associated with a deformation over length l with the active stress $\sim \zeta$. Due to the high elastic energy stored in these so-called "walls", $\pm 1/2$-defects primarily form here. The self-propelling nature of the $+1/2$-defects prevents

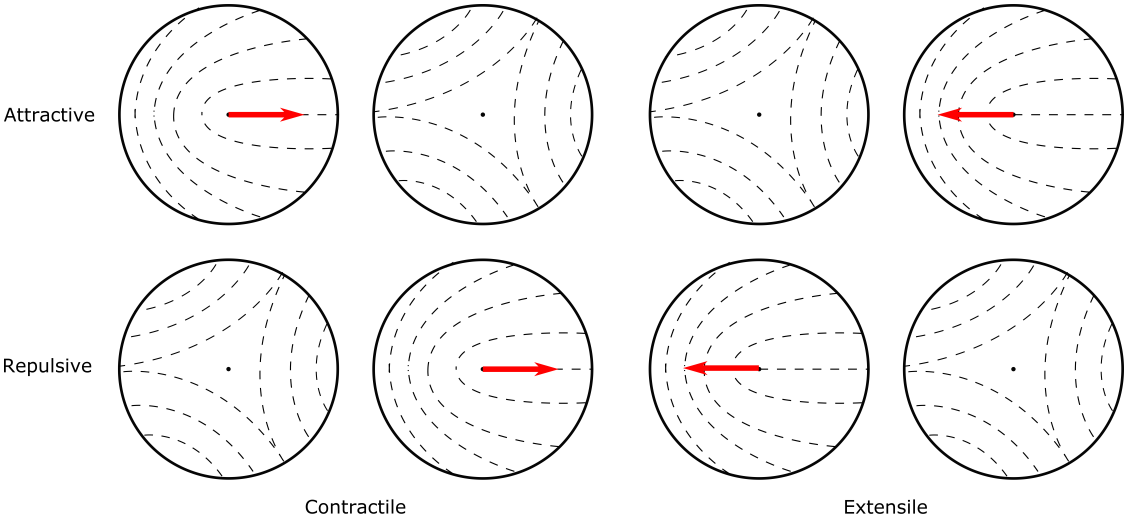

Figure 1.10: Schematic of the interaction of defects in active nematics. Based on the respective orientation the defects can either attract or repel each other. +1/2-defects propel in the direction of their "head" (extensile) or "tail" (contractile) depending on the sign of the activity constant, indicated by the red arrow in the schematics.

the forming defect pairs from annihilating immediately, thus allowing for a state where defects are continuously generated and, when oppositely charged defects meet, annihilated. This state, which exists where there are no boundaries or other hydrodynamic screening mechanisms present, is termed active turbulence. The active turbulence state is highly chaotic, consisting of fluid jets and swirls (see Fig. 1.11).

To generate active turbulence, defect pairs have to unbind (see Fig. 1.12 for an example in a two-dimensional active nematic based on microtubules and molecular motors) [14]. In this scenario, the nematic will enter into a state where activity will continuously disorder the system. It is still debated whether there is a threshold activity to create defect unbinding. A naive argument would say that the dynamics of a defect pair in an active nematic would be governed by relaxation in an effective potential

$$\partial_t r = \nu \partial_r V, \quad V(r) = \frac{\pi K}{2} \log \frac{r}{a} - \frac{u_0}{\nu} r, \tag{1.45}$$

where r is the distance between two $\pm 1/2$-defects and a the size of the defect core. The resulting potential barrier $V(r_c)$ at distance r_c

$$V(r_c) = \frac{\pi K}{2} \left(\log \frac{\pi \nu K}{2 u_0 a} - 1 \right), \quad r_c = \frac{\pi \nu K}{2 u_0}, \tag{1.46}$$

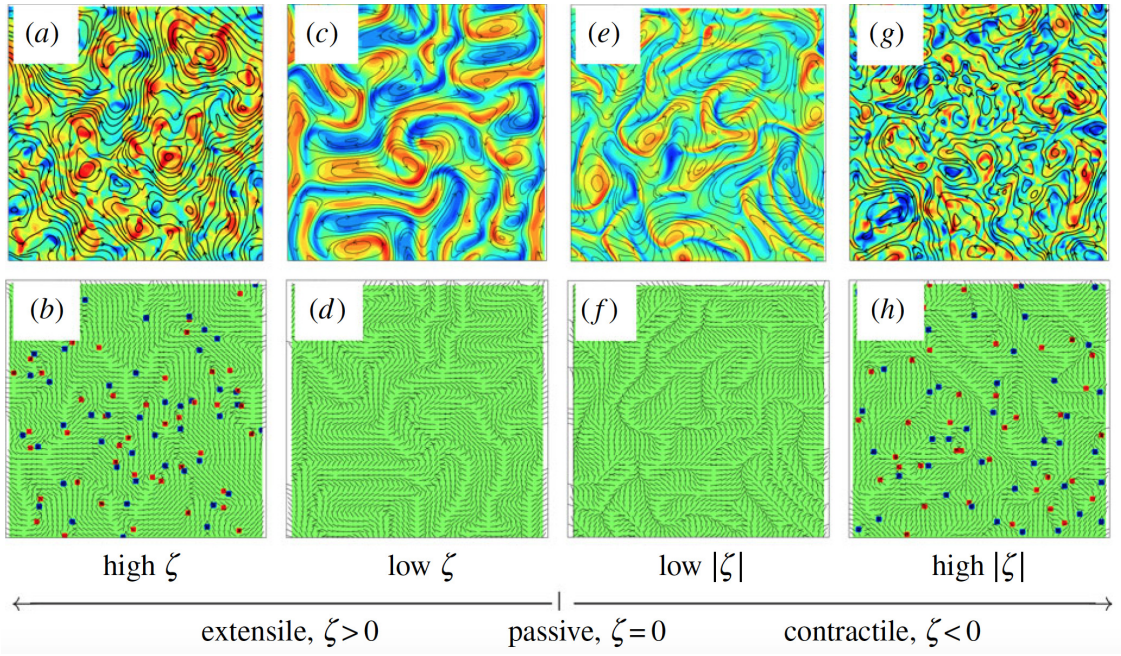

Figure 1.11: Flow and director patterns from simulations of active nematics comparing an extensile and contractile system for high and low values of the activity coefficient ζ. Streamlines and vorticity field, with red and blue colouring corresponding to high positive and negative vorticity, respectively, are shown for (a) an extensile system with large activity, (c) an extensile system with small activity, (e) a contractile system with small activity and (g) a contractile system with large activity. The corresponding director field and topological defects (+1/2, red; −1/2, blue), if present, are shown in (b,d,f, and h). Image taken from [48].

is finite, which means that the defect pair is always unbound, and nematic order always destroyed, for any non-zero temperature. It was however recently shown that rotational noise disrupt the directed motion of the +1/2-defects, and can therefore restore the ordered nematic phase [49]. Defect unbinding will only happen when the persistence length of a +1/2-defect u_0/D_r, with D_r the rotational diffusivity, is larger than the position of the barrier $r_c = K/u_0\gamma$, with γ a rotational viscosity. This means that there is a theoretical threshold for active turbulence, even in an infinite system.

Active turbulence is markedly different from inertial turbulence. Firstly, in active turbulence the energy input happens at the scale of the individual particles, which is the smallest length scale in the system. In inertial turbulence energy is input at large scales. Secondly, in active nematics inertia can be negligible (Re $\ll 1$), but still a highly disordered distribution of vortices is present [50, 51]. Taming active turbulence is an active research topic and will be considered in Chapters 4 and 5.

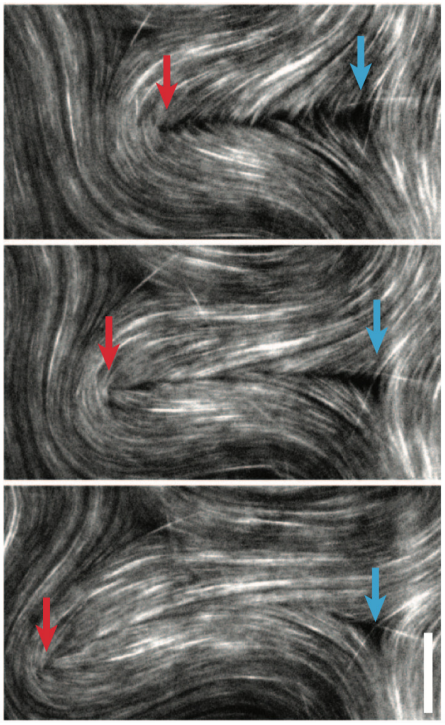

Figure 1.12: A sequence of images demonstrates defect unbinding in an active suspension of microtubules and kinesin. The fracture line terminates with a pair of oppositely charged disclination defects (the red arrow tracks the $+1/2$ topological defect, the blue arrow the $-1/2$ topological defect). After the fracture line self-heals, the defect pair remains unbound. Time lapse, 15 s; scale bar, 20 μm. Image taken from [14].

1.3 The hybrid lattice Boltzmann method

In the context of this thesis the Navier-Stokes equation (1.29) is solved using a lattice Boltzmann algorithm, while the Cahn-Hilliard equation for ϕ (1.26) and the evolution equation for $\underline{\underline{Q}}$ (1.23) are solved using a finite difference approach, as first put forward by Marenduzzo et al. [52].

The lattice Boltzmann algorithm is defined in terms of a set of partial distribution functions at each lattice site $\underline{x}$. The distribution function represents the density of particles with a certain velocity at a certain point in time. In the algorithm, the distribution function is discretised, and only has values at lattice sites with spacing Δx and at discrete times with time step Δt. In the hybrid lattice Boltzmann scheme one set of distribution functions is needed, here named $f_i(\underline{x})$, where i labels a lattice

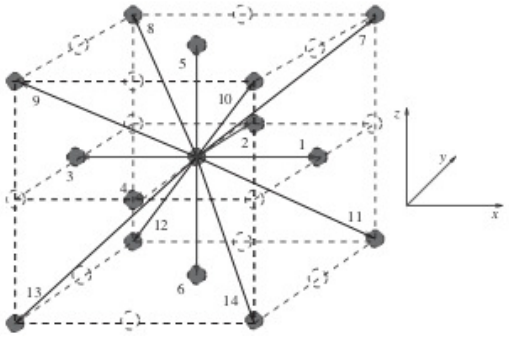

Figure 1.13: Lattice geometry and lattice vectors for the D3Q15 lattice Boltzmann model. Image taken from [53].

direction from site $\underline{x}$. The fluid density is related to the distribution function by

$$\rho = \sum_i f_i. \tag{1.47}$$

Each lattice direction i is associated with a velocity vector $\underline{e}_i$. In the D3Q15 velocity vector lattice the velocity vectors are $\underline{e}_i = (0,0,0)$, $(\pm 1,0,0)$, $(0,\pm 1,0)$, $(0,0,\pm 1)$, and $(\pm 1,\pm 1,\pm 1)$ (see Fig. 1.13). The fluid momentum is then given by

$$\rho \underline{u} = \sum_i f_i \underline{e}_i. \tag{1.48}$$

The set of distribution functions evolves over a time step Δt according to

$$f_i(\underline{x}+\underline{e}_i\Delta t, t+\Delta t) - f_i(\underline{x},t) = \frac{\Delta t}{2}(\mathcal{C}_{fi}(\underline{x},t,\{f_i\}) + \mathcal{C}_{fi}(\underline{x}+\underline{e}_i\Delta t, t+\Delta t, \{f_i^*\})). \tag{1.49}$$

This represents free streaming with a velocity $\underline{e}_i$, followed by a collision step. The collision step allows the distribution function to relax to equilibrium. $\{f_i^*\}$ is a first order approximation to $f_i(\underline{x}+\underline{e}_i\Delta t, t+\Delta t)$, obtained by computing

$$f_i^* - f_i(\underline{x},t) = \Delta t \mathcal{C}_{fi}(\underline{x},t,\{f_i\}). \tag{1.50}$$

This is similar to a predictor-corrector scheme, removing lattice viscosity terms to second order and giving improved stability. The collision operator $\mathcal{C}_{fi}$ has the form of a single Boltzmann relaxation time, together with a forcing term

$$\mathcal{C}_{fi}(\underline{x},t,\{f_i\}) = -\frac{1}{\tau}(f_i(\underline{x},t) - f_i^{eq}(\underline{x},t,\{f_i\})) + p_i(\underline{x},t,\{f_i\}). \tag{1.51}$$

The form of the equations of motion follows from the choice of the moments of the equilibrium distributions f_i^{eq} and the forcing terms p_i. The equilibrium distributions are constrained by

$$\sum_i f_i^{eq} = \rho, \quad \sum_i f_i^{eq} \underline{e}_i = \rho \underline{u}, \quad \sum_i f_i^{eq} \underline{e}_i \underline{e}_i = -\underline{\underline{\sigma}} + \rho \underline{u}\underline{u}, \tag{1.52}$$

so that the zeroth and first moment of f_i^{eq} ensure that mass and momentum are conserved. The second moment of f_i^{eq} is determined by $\underline{\underline{\sigma}}$, which is the symmetric part of the stress tensor $\underline{\underline{\Sigma}}$. The divergence of the antisymmetric part of the stress tensor $\underline{\underline{\tau}}$ enters as a body force through

$$\sum_i p_i = 0, \quad \sum_i p_i \underline{e}_i = \underline{\nabla} \cdot \underline{\underline{\tau}}, \quad \sum_i p_i \underline{e}_i \underline{e}_i = 0. \tag{1.53}$$

The conditions in equations (1.52) and (1.53) can be satisfied, as usual in lattice Boltzmann schemes, by writing the distribution functions and forcing terms as polynomial expansions in the velocity (see for instance [53]). The coefficients in the expansion are determined by requiring that the constraints are satisfied.

The equations for ϕ and $\underline{\underline{Q}}$, on the other hand, are solved using a simple finite difference scheme

$$\phi(t + \Delta t) = \phi(t) + \Delta t(M \nabla^2 \mu - \partial_i (u_i \phi)), \tag{1.54}$$

$$Q_{ij}(t + \Delta t) = Q_{ij}(t) + \Delta t(S_{ij} + \Gamma H_{ij} - (u_k \partial_k) Q_{ij}). \tag{1.55}$$

Compared to the full lattice Boltzmann approach, where seven sets of fifteen distribution functions have to be stored (in case the D3Q15 velocity vector lattice is adopted), now only one set of distribution functions plus the value of ϕ and the five independent components of $\underline{\underline{Q}}$ are needed. This reduces the computational cost significantly, and avoids the error term arising from the Chapman-Enskog expansion connecting the lattice Boltzmann model to the order parameter evolution [54].

1.4 Overview of the thesis

This thesis consists of five related investigations concerning the dynamics and topology of active and passive liquid crystals. Here we outline the content of each Chapter, and touch upon some practical implications of our work. In addition to the main Chapters 2−6, Chapter 7 summarises our findings and gives directions for future research.

In Chapter 2 we investigate the electric-field-induced elongation of lyotropic nematic tactoids. Nematic tactoids occur at the isotropic-nematic phase transition, and are long-lived but metastable micro-domains of the nematic phase growing in the isotropic phase during phase separation. The work was inspired by experimental results on chitin tactoids from Patrick Davidson's group at Paris-Sud, and unveils the physical mechanism behind their strong elongation, up to aspect ratios of ~ 20. By simulating nematic droplets in an isotropic background we show that the strong elongation is due to a combination of strong anchoring of the nematic director to the interface and small internal elasticity. The stretching is completely reversible upon removal of the field, and the time-scales suggest hydrodynamics plays a role. This is confirmed by our simulations. In the elongated state the individual particles in the tactoids are much more aligned than in the spindle-like state. Therefore, aligning tactoids using an electric field could improve the optical properties of liquid crystal films, which are obtained through a drying process during which the solutions undergo an isotropic-nematic transition.

In Chapter 3 we turn our attention to cholesteric and two-dimensional blue phase tactoids. In nematic tactoids the shape is strongly influenced by the anchoring of the individual particles to the interface. Therefore we investigate what happens when a liquid crystal with a more complicated internal structure, such as a cholesteric or a two-dimensional blue phase, is confined in a droplet. We identify a wealth of droplet shapes including disk-like, elongated and star-shaped morphologies. We then continue by applying an electric field perpendicular to the shapes to obtain droplets with directors pointing along the electric field in the centre, but twisting away near the edge. Such edge structures suggest an analogy to experimental

observations of chiral rafts in dilute suspensions of rod-like fd-viruses with attractive interactions due to addition of non-adsorbing polymers. Our simulations could be used to investigate the interaction between raft structures, potentially as a model for rafts in lipid bilayers.

Next, in Chapter 4 we continue with the topic of two-dimensional blue phases, but introduce activity. The structure of a two-dimensional blue phase comprises a hexagonal lattice of double-twist cylinders, separated by a lattice of $-1/2$ topological defects. In models for active nematics active flows are generated by gradients in the director field. In the ground state of the two-dimensional blue phase there are gradients everywhere in the system, which leads to interesting dynamics. In particular, in case of contractile activity, a stable vortex lattice is generated, because the active instability is screened by the cholesteric pitch length. The double-twist cylinders are unstable to extensile activity, however, and we observe active turbulence. Previous work has focussed on substrate friction or confinement as methods to control active materials, relying on the hydrodynamic length scale or the system size respectively to screen the activity. Our work shows that certain types of active materials could also be controlled by introducing an internal length scale, in this case the cholesteric pitch.

In Chapter 5 we move to consider one of the other potential control mechanisms, substrate friction. We show that we can reproduce experiments on two-dimensional microtubule-kinesin mixtures on a smectic oil-water interface, obtaining a laning state with well-defined antiparallel flow directions. We do this by introducing anisotropic friction, meaning that the dissipation by the substrate in one direction is much larger than in the other direction. We find that the occurrence of the laning state is strongly dependent on the friction ratio.

Finally, in Chapter 6 we develop our active lyotropic liquid crystal model further to allow for simulations of deformable active nematic shells in three dimensions. Topological defects have to exist on a shell due to the Poincaré-Hopf theorem: the total topological charge will be $+2$. Since stresses in active nematics are largest at the location of topological defects, it can be expected that any deformation of an

active nematic shell will occur at the location of the defects. In our simulations we reproduce experiments and simulations of motile topological defects on strictly spherical shells. We then demonstrate that protrusions form on deformable active nematic shells, driven by the topological defects. This has potential implications for morphogenesis processes: we show that these events can occur due to purely mechanical cues.

2

Electric-field induced shape transition of nematic tactoids

The occurrence of new textures of liquid crystals is an important factor in tuning their optical and photonic properties. In this chapter we show, both experimentally and by numerical computation, that under an electric field chitin tactoids (i.e., nematic droplets) can stretch to aspect ratios of more than 15, leading to a transition from a spindle-like to a cigar-like shape. We argue that the large extensions occur because the elastic contribution to the free energy is dominated by the anchoring. We demonstrate that the elongation involves hydrodynamic flow and is reversible: the tactoids return to their original shapes upon removing the field. This work was carried out in collaboration with Patrick Davidson and co-workers at Paris-Sud, who performed the experiments and co-wrote the paper, which is published in Physical Review E [55].

2.1 Introduction

When considering liquid crystals, a distinction is made between thermotropic and lyotropic liquid crystals. Thermotropic liquid crystals are chemically pure substances consisting of rod-shaped or disk-shaped molecules. The interaction between the molecules results in long-range orientational order of their preferred axis, but without

any three-dimensional translational order, and the phase behaviour is dependent on temperature. Lyotropic liquid crystals, on the other hand, are formed when elongated colloidal particles are dispersed in a solvent. As Onsager showed in his theoretical treatment of the isotropic-nematic transition [56], homogeneous dispersions of elongated stiff particles with hard-core repulsion can become unstable and phase separate when the concentration increases. Orientation fluctuations in the isotropic state will drive density differences, resulting in phase separation of the rods into a dilute isotropic phase and a dense nematic phase.

The phase separation mechanism is purely entropic. The loss in entropy due to orientational ordering in the nematic phase is counterbalanced by the increase in translational entropy: the available space for each rod increases when the particles become more aligned.

The lyotropic nematic droplets that appear in the disordered isotropic phase during phase separation are termed tactoids [57]. These tactoids are in fact transient. They are the fingerprint of early-stage phase separation, and eventually they coalesce to minimise the interfacial area between the isotropic and nematic phases: the thermodynamically stable state consists of two continuous phases, with only a single interface between them. Since this kinetic evolution is typically very slow, and the two separated nematic and isotropic phases may only be achieved after months or years, at any time tactoids can be considered to be in local equilibrium, associated with a free energy minimum.

Tactoids have characteristic shapes that have already been the subject of several theoretical studies [58–64] and experiments on systems such as vanadium pentoxide (V_2O_5) [58, 65], carbon nanotubes [66, 67], rod-like viruses [68, 69], F-actin in cells [70], chromonic liquid crystals [71], and cellulose nano-crystals [72–74]. These investigations showed that the typical tactoid shapes, for example the so-called spindle-like shape with a bipolar director field (see the right inset in Fig. 2.1), are determined by the balance between a low surface tension, strong anchoring, and the elasticity of these lyotropic nematics. Such distinctive shapes are not usually found

in the case of thermotropic nematics that have very large surface tension, leading to almost spherical drops, even though the director field can be bipolar [75].

Like most liquid crystals, tactoids are very sensitive to external magnetic or electric fields but only a few studies have so far dealt with this phenomenon. The most obvious effect of the field on a tactoid is usually the overall orientation of its long axis with respect to the field direction [58]. Subjecting tactoids of plate-like colloidal particles to sufficiently large magnetic fields induces a sudden rearrangement of the director field and leads to stable split-core defect structures [76], while tactoids of rod-like colloids can also be slightly stretched without qualitative change of the internal structure of the director field [58].

Here we present results to show that, for large electric fields, chitin tactoids with a bipolar director field can elongate to aspect ratios of more than 15, forming cigar-shaped droplets with a uniform director configuration except for at the tips. The elongation process is entirely reversible upon removal of the electric field to recreate the original tactoid shapes. This is in sharp contrast with previously reported aspect ratios of lyotropic liquid crystals under influence of an applied field. We will first discuss experimental results, carried out by Patrick Davidson's group at Paris-Sud, in some detail, because the simulations were performed in order to understand these experimental observations. For details about the experimental setup we refer to [55]. We then describe numerical simulations of the dynamical evolution of tactoids in an electric field, and, after having reproduced the observations from the experiments, argue that the substantial elongations are the result of weak elasticity and strong anchoring. Furthermore, we show that there is a minimum electric field necessary to elongate the tactoids, which is also associated to strong anchoring of the directors to the interface.

2.2 Experimental results

The chitin volume fraction in the capillaries considered is $\phi \approx 0.02$. The suspension demixes into coexisting isotropic and nematic phases, with respective volume fractions $\phi_{\mathrm{I}} = 0.018$ and $\phi_{\mathrm{N}} = 0.028$. Nematic tactoids form and slowly sediment

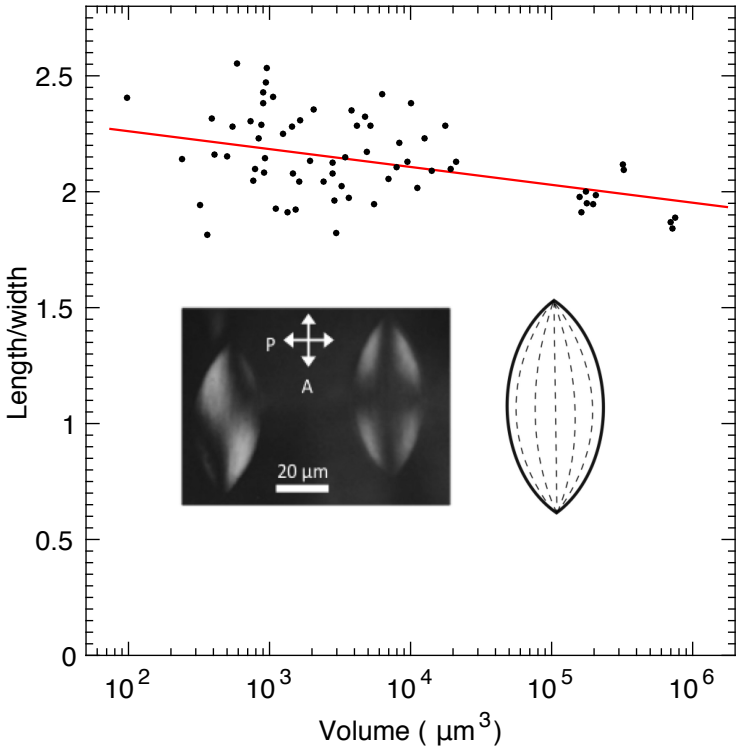

Figure 2.1: Aspect ratio of the tactoids as a function of the tactoid volume before applying the electric field. Left inset: the observation under crossed polarisers (white double headed arrows) reveals the bipolar structure of the tactoids. The two tactoids look different because the axis of the tactoid on the right is exactly parallel to the analyser direction whereas that of the tactoid on the left lies at an angle of $\sim 3°$. Right inset: schematic drawing of a tactoid, with dashed lines representing the director field.

over a few hours as the macroscopic isotropic-nematic phase separation proceeds. In the absence of any applied field, the tactoids have a spindle-like shape and bipolar morphology, independent of their size (see the insets in Fig. 2.1). They are randomly oriented throughout the sample. Moreover, their aspect ratio, $L/D \approx 2$ where L is the length and D the diameter, is only weakly dependent on the volume V (see Fig. 2.1). The interfacial anchoring, that is, the strength of the alignment of nematogens parallel or perpendicular to the interface, and the surface tension scale with the surface area of the tactoids, while the elasticity scales with the volume. The constant aspect ratio observed here therefore suggests that the interfacial anchoring and the surface tension dominate in this system. We note that this is in contrast to previous works, where aspect ratios of tactoids were shown to decrease with increasing volume [58, 67, 69, 77], in reasonable agreement with theoretical

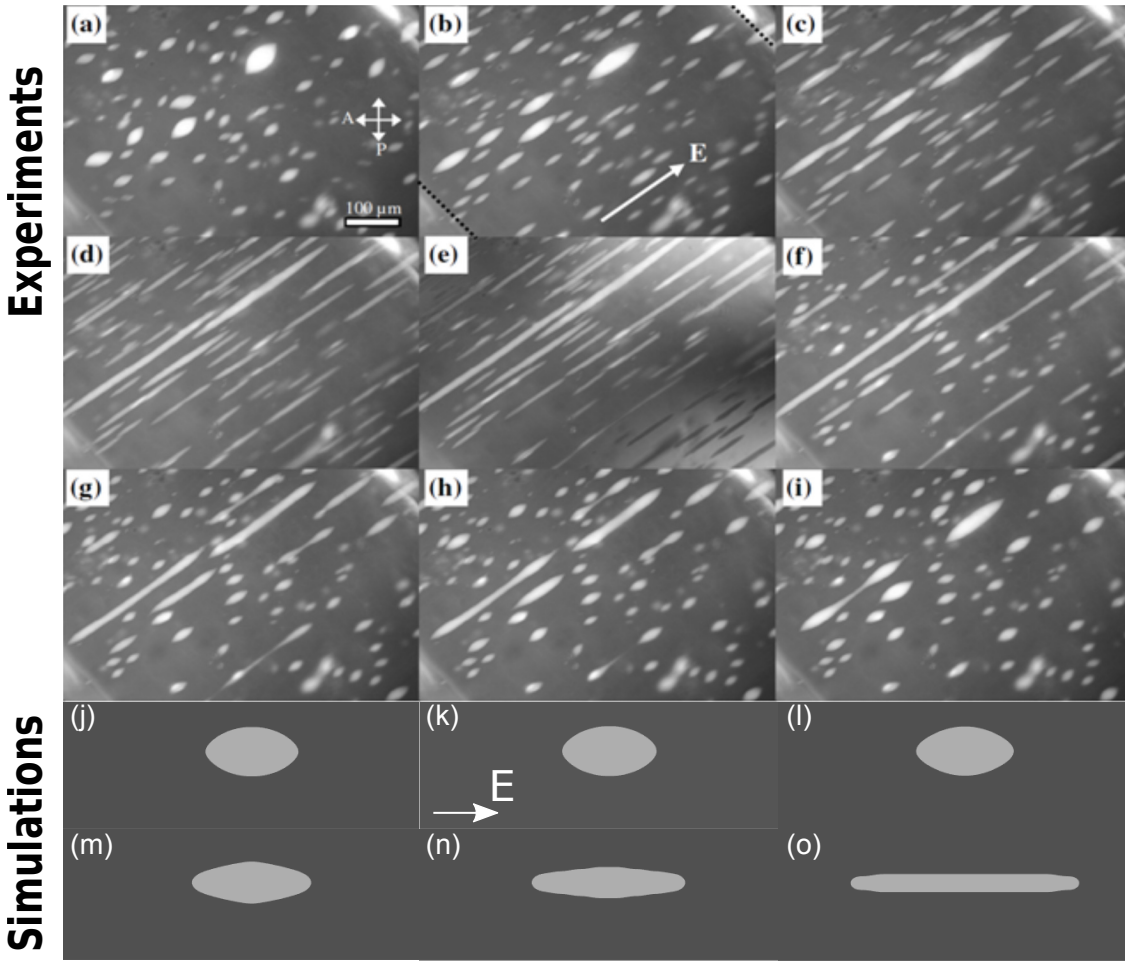

Figure 2.2: Time-evolution of the tactoids under a field $E_{\rm rms} = 160$ Vmm^{-1}, $f = 300$ kHz, and relaxation after switching off the field. Experiments: (a–e) The field is applied respectively for time $\tau_{\rm on} = 0, 120, 210, 640, 1080$ seconds. (f–i) The sample has relaxed for $\tau_{\rm off} = 230, 380, 530, 820$ seconds after the field removal. The double-headed arrows in (a) show the orientations of the polariser P and the analyser A. In (b) the field direction (white arrow) and the shadows cast by the out-of-focus electrodes (black dotted lines) are shown. Note that in (e) the contrast varies and is inverted in some regions, due to introducing a Berek compensator. Simulation: (j–o) Time evolution of simulated tactoids under an electric field. (j) Equilibrium tactoid shape. The director field is bipolar and the aspect ratio is ~ 2. Because we employ a diffuse interface model the tips may appear slightly rounded. (k–o) The tactoid 200, 400, 800, 1600 and 30000 simulation time steps after applying the electric field. The droplet stretches to an aspect ratio of ~ 16, and becomes cylindrical with conical tips.

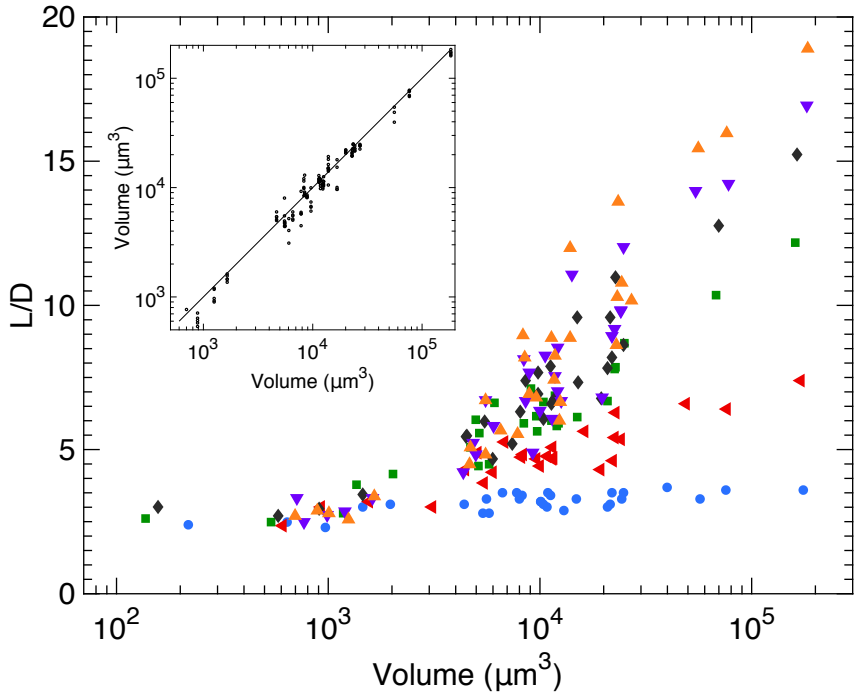

Figure 2.3: Axial ratio of the tactoids as a function of their volume and the time under field $E_{\rm rms} = 160$ Vmm^{-1} and $f = 300$ kHz. The data corresponding to the same time under field are plotted with the same symbol. Blue circles are taken after 120 s, red triangles after 210 s, green squares after 410 s, black diamonds after 640 s, purple inverted triangles after 850 s and orange triangles after 1080 s. The data measured for the same tactoid lie almost on a vertical line, as the volume of the tactoid is approximately independent of the time under the field. This is demonstrated by the inset which shows the volume of the tactoids at different times as a function of the final volume after 1080 seconds under field.

predictions [58, 59, 67, 78] for models where elasticity is relevant.

Before the first application of the field, the tactoids are completely disoriented. When the electric field is applied, a reorientation of the director along the field is observed inside the tactoid, except in the close vicinity of the nematic-isotropic interface. This purely elastic process is very fast (response times $<$ 1s) and is reversible upon field removal. At much longer time scales ($10 - 100$ seconds) the tactoids slowly reorient along the field, rotating approximately as rigid bodies. Simultaneously, but at even longer time scales ($100 - 1000$ seconds), the tactoids become distorted as their aspect ratio increases. Therefore, short pulses of electric field, separated by relaxation times, were first applied to orient all the tactoids along the electric field direction and avoid any distortion of their shape. A population of

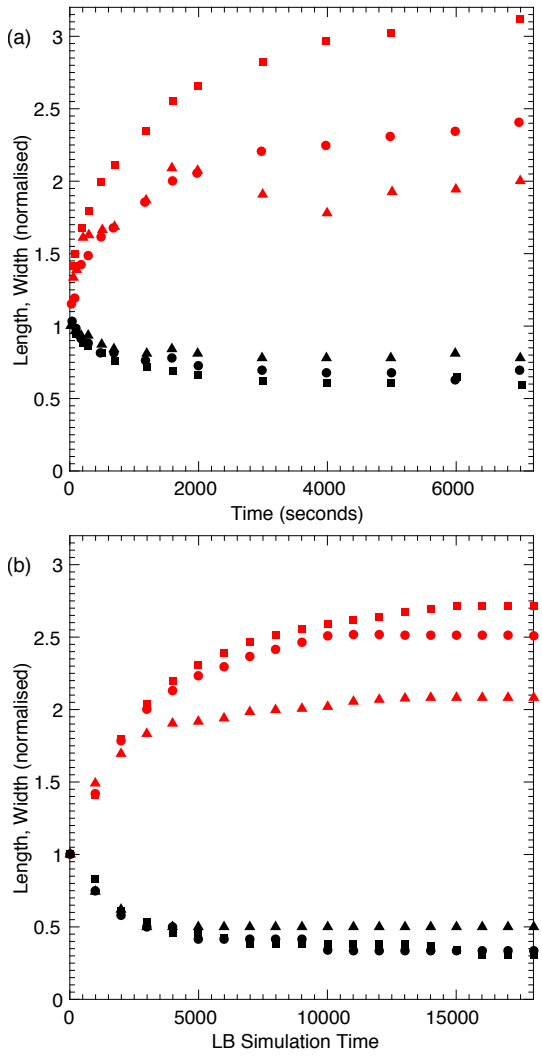

Figure 2.4: Time-dependence of length L (red markers) and width D (black markers) of tactoids of different sizes. L and D are normalised by their initial values in the absence of an electric field. (a) Experiments: Three chitin tactoids with $LD^2 = 2.0 \times 10^4$ μm^3 (triangles), 1.5×10^5 μm^3 (dots) and 3.7×10^5 μm^3 (squares), subject to a 500 kHz a.c. field $E_{\rm rms} = 154$ Vmm^{-1}. (b) Simulations: Three tactoids with $LD = \pi 8^2$ (triangles), $\pi 14^2$ (dots) and $\pi 16^2$ (squares).

tactoids of very different volumes but of same shape and orientation was thus produced (Fig. 2.2(a)).

When submitted to an a.c. electric field of constant amplitude (in a d.c. electric field charges accumulate until the field is completely screened in the bulk electrolyte), the tactoids strongly deformed and became highly elongated along the field direction (Fig. 2.2(b)-(e)). With time, the largest tactoids evolved from the bipolar structure to a tubular shape with conical tips (Fig. 2.2(d)-(e)). In the simulations, described

in more detail below, this behaviour is nicely recovered (see Fig. 2.2(j)-(o)). The deformation is reversible as the tactoids became bipolar again and their aspect ratio returned to its initial value in $\sim 10^3$s after the electric field was switched off (Fig. 2.2(f)-(i)). This behaviour is significantly different from previous work on tactoids where the aspect ratio only increased by $\sim 10\%$ under a 1T magnetic field and the tactoid structure remained strictly bipolar [58, 65, 78].

The deformation of the tactoids in the field strongly depends on their volume (see Fig. 2.3). For example, small tactoids of volume $10^2 - 10^3 \mu\text{m}^3$ did not deform much on the time scale of the experiment (30 minutes), while the aspect ratio of large tactoids ($10^5 \mu\text{m}^3$) doubled in 5 minutes and reached $L/D \approx 15$ in 30 minutes. The volume of the tactoids remained almost constant during the deformation process (see the inset in Fig. 2.3).

The evolution of the tactoid shapes when a field is applied is summarised in Fig. 2.4(a) which shows the time evolution of the tactoid length and diameter for different tactoid volumes. Small tactoids undergo small deformations but on the relatively fast time scale of a few hundred seconds. By contrast, the largest tactoids show very large deformations occurring on time scales of several thousands of seconds. The large time scale suggests that fluid flows are involved in the deformation of large tactoids under the electric field. The same qualitative behaviour was observed for field amplitudes between 100 and 450 Vmm^{-1}.

Without a field, the length and diameter of the tactoids scale with the cube root of their volume (see Fig. 2.5), which is expected because all tactoids have the same aspect ratio. Under the electric field, the tactoid diameter decreases with increasing tactoid volume, showing a crossover from a cube root behaviour to a weaker dependence as a function of volume. The value of the crossover volume, V_c, depends on the electric field amplitude; it is $V_\text{c} \sim 2 \times 10^4 \mu\text{m}^3$ at $E_\text{rms} = 154$ Vmm^{-1} and $V_\text{c} \sim 5 \times 10^3 \mu\text{m}^3$ at $E_\text{rms} = 309$ Vmm^{-1}. There is a larger corresponding increase in the tactoid length leading to aspect ratios as high as 15. Moreover, we observed the qualitative change of the tactoid morphology from the usual spindle-like shape with bipolar structure to a tubular shape. This consists of an almost

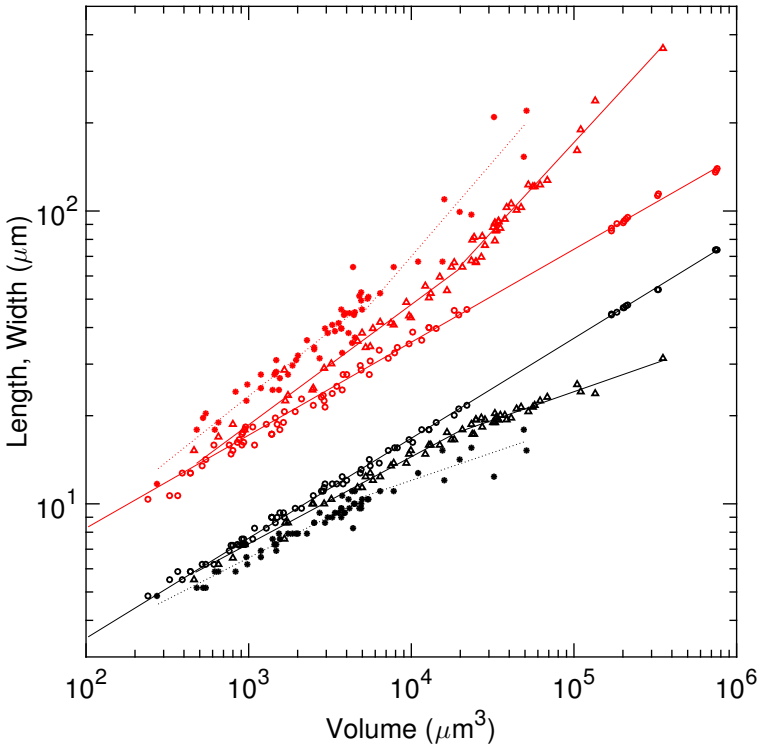

Figure 2.5: Length L (red markers) and width D (black markers) of the tactoids as a function of the tactoid volume LD^2 before the application of the field (open circles), after 61000 s under $E_{\rm rms} = 154$ Vmm^{-1} (triangles) and after 3600 s under $E_{\rm rms} = 309$ Vmm^{-1} (closed symbols). The no-field data are fitted with a power law with coefficients $\beta_{\rm L} = 0.32$ and $\beta_{\rm D} = 0.34$, very close to the $V^{1/3}$ dependence expected for constant aspect ratio L/D. The 154 Vmm^{-1} data are piecewise fitted with power laws with respectively $\beta_{\rm L} = 0.41$ and 0.60, and $\beta_{\rm D} = 0.30$ and 0.20, with the crossover at $LD^2 \sim 2 \times 10^4 \mu$m^3. For $E_{\rm rms} = 309$ Vmm^{-1}, the coefficients are respectively $\beta_{\rm L} = 0.44$ and 0.64, and $\beta_{\rm D} = 0.28$ and 0.19, with the crossover at $LD^2 \sim 5 \times 10^3 \mu$m^3.

cylindrical central region with uniform director distribution ending with two conical tips with an approximately bipolar director field.

To our knowledge, these features have not been reported in any other system. For comparison, under a 1T magnetic field, large V_2O_5 tactoids are aligned along the field and are slightly elongated, with an aspect ratio increasing by only about 10%, without any change of their bipolar structure [58]. In a similar way, the axial ratio of lens-like tactoids formed by gibbsite platelets only slightly varies (by $\sim 30\%$) under a 1T magnetic field [76], in good agreement with theoretical models [63, 76].

The action of the magnetic field is due to the coupling of the field with the magnetic anisotropy of the nematic phase; this effect can only be expected if (at least)

one of the coexisting phases is anisotropic. This is no longer the case when an electric field is applied to biphasic systems. Apart from the direct coupling of the electric field with the dielectric anisotropy of the nematic phase, given by the energy term $\epsilon_0 \Delta\epsilon (\underline{E} \cdot \underline{n})^2/2$, where $\Delta\epsilon = \epsilon_\parallel - \epsilon_\perp$ is the dielectric anisotropy, there are additional energy terms that are unrelated to the phase anisotropy. These terms are relevant even for coexisting isotropic phases. They are due to the different dielectric constant ($\epsilon_{\rm in} \neq \epsilon_{\rm out}$) and conductivity ($K_{\rm in} \neq K_{\rm out}$) inside and outside of the droplet interface. Under a field, electric charges accumulate on the interface, respectively as bound (polarisation) or mobile (conductivity) charges. Their surface density is anisotropic and depends on the orientation and shape of the droplet [79–83]. Therefore, an initially spherical isotropic droplet elongated under field, becomes ellipsoidal, and orients with its main axis along the field. This process minimises the electric energy cost at the price of increasing the interface area and the interface energy. This phenomenon is well known for isotropic droplets and, when the dielectric and/or conductivity contrast is large, a droplet elongation of 15% has been reported [82].

The same mechanisms are involved in the electric-field-induced elongation of thermotropic nematic droplets in coexistence with their isotropic melt or with another liquid [84–87]. Usually for thermotropic nematics, the surface tension is much larger than the anchoring energy and the droplets are (approximately) spherical without a field. Under a field, the nematic director in the droplet is aligned along the field (assuming that $\epsilon_\parallel > \epsilon_\perp$) and the effective dielectric and conductivity contrasts at the interface are now respectively $\epsilon_\parallel - \epsilon_{\rm out}$ and $K_\parallel - K_{\rm out}$. When these contrasts are strong and the surface tension of the nematic is relatively weak (as usual), the droplet aspect ratio can be quite large, up to 3, especially for low frequencies, $f < 1$ kHz, where the conductivity mechanism is dominant [84, 86]. However, even in this case, the shape of the droplet is not spindle-like but ellipsoidal because, as in the isotropic case, there is only competition between the electric and surface tension energies, the anchoring energy being negligible. Yet, the flow induced by the friction drag exerted by the electric current in the

liquid is an artefact that can induce cusp-like distortions of the droplet in d.c. or very low frequency a.c. fields [86].

All these auxiliary mechanisms are irrelevant in these experiments. Indeed, working with external electrodes, without direct contact with the liquids, requires the use of very high frequencies to achieve enough penetration of the field in the liquid. The frequencies used are much higher than the relaxation frequency of the conductivity (Maxwell-Wagner mechanism [88]) so that this effect can be neglected. For the same reason, the flow directly induced by the electric current drag is also negligible. Moreover, the dielectric contrast $\delta\epsilon \approx \epsilon_{\text{in}} - \epsilon_{\text{out}}$ is very small ($\delta\epsilon \ll \epsilon_{\text{out}}$) in chitin suspensions and its influence on the tactoid shape is negligibly small.

The only remaining electric-field contribution to the tactoid energy is the direct coupling with the dielectric anisotropy of the nematic phase, like the magnetic field case. Nevertheless, for large tactoids, deformations were observed two orders of magnitude larger than reported for V_2O_5 in a magnetic field.

The most unexpected result is the field-induced transition from a spindle-like to a tubular shape for large tactoids. Theoretical models explain the spindle-like shape by the competition between the bend and splay elastic energies, the surface tension and the anchoring energy [58, 59, 78]. Under application of an external field the energy balance is modified, leading to variation of the tactoid aspect ratio. However, the models predict that the shape should remain spindle-like, as in the absence of field, contrary to our observations.

At least at a qualitative level, one does not expect significant differences in elastic properties and surface tension between chitin suspensions and other aqueous lyotropic colloids of rod-like particles. However, we argued above that the independence of the tactoid shape on its volume suggests that the elastic contribution to the free energy is small compared to the surface tension and anchoring contributions. Moreover, close examination of the orientation of the director in the bulk and at the interface of the tubular tactoids in strong fields revealed that although the director orientation is completely uniform in the bulk (and parallel to the electric field), close to the tips the director remains strictly

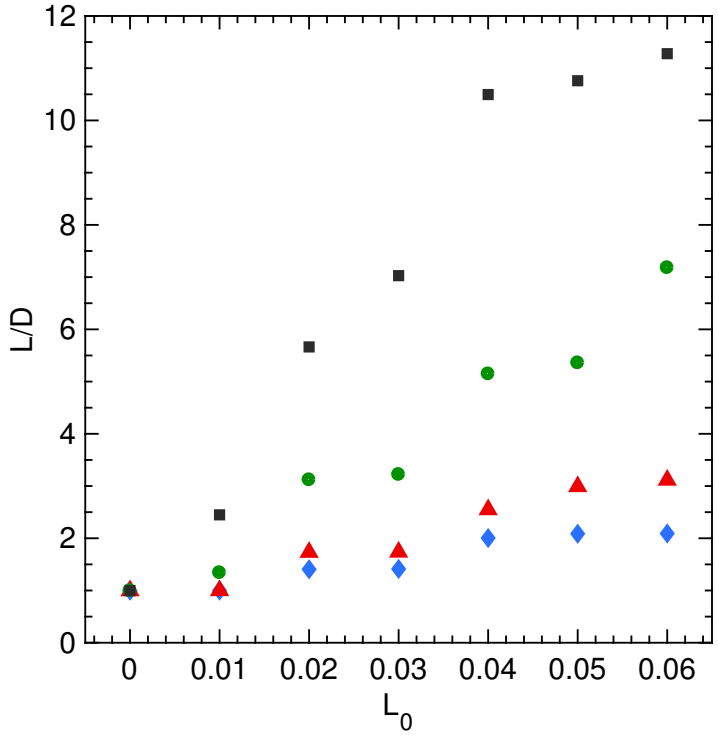

Figure 2.6: Simulation results showing how the final aspect ratio L/D of a tactoid depends on its anchoring strength L_0 and the electric field strength. Blue diamonds represent an electric field strength of 0.06, red triangles 0.10, green circles 0.15 and black squares 0.20.

parallel to the surface and relaxes over a length of about 3μm. This demonstrates that the anchoring is actually very strong and any tilt of the director from the surface can be neglected at the droplet boundary, even in strong fields.

Since, at this stage, the physical origin of this novel shape remains unknown and since its description seems out of reach of the analytical models available to date, numerical simulations were employed. Moreover, the complex dynamical evolution of the tactoids in an electric field is difficult to model analytically but it can be captured by a numerical approach.

2.3 Numerical simulations

In order to understand the nature of the shape change of the tactoids and to scrutinise the underpinning physical mechanism for their large elongation under electric fields, the nematohydrodynamics approach set out in Chapter 1 is employed. To reproduce

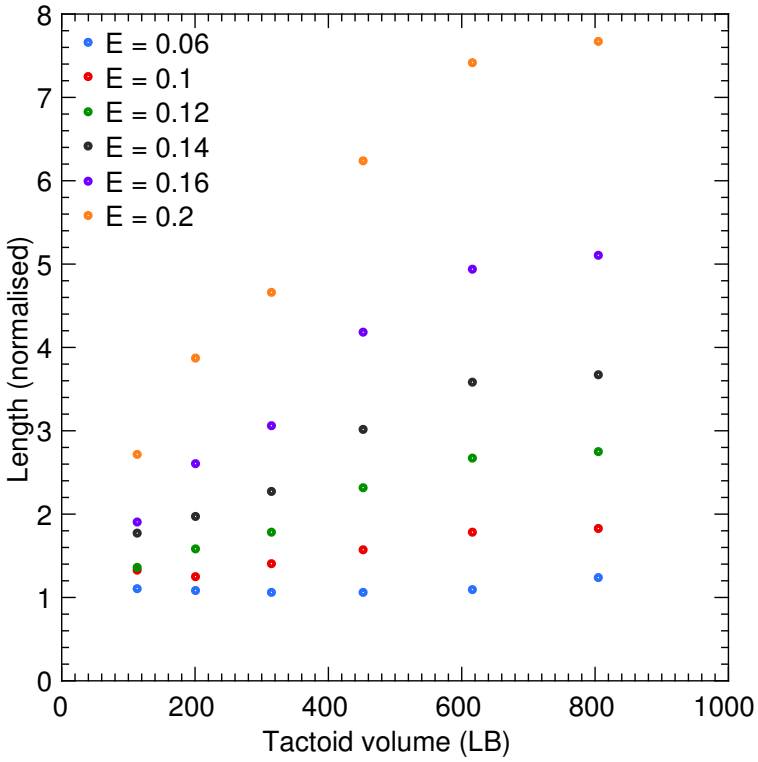

Figure 2.7: Simulation results showing how the final length of a tactoid depends on its volume and the electric field strength.

the experimental results qualitatively, the one-elastic-constant approximation is used, and the free energy parameters are set to $A_0 = 1.5$, $A_\phi = 0.28$, $\eta_0 = 2.7$, $\eta_s = 0.3$, $L = 0.093$, $\epsilon_a = 1$, $k_\phi = 0.05$ and $L_0 = 0.06$. Furthermore, in the dynamical equations the parameters are set to $M = 0.5$, $\Gamma_Q = 0.7$, $\xi = 0.7$, $\nu = 2/3$, $\rho = 1$ and $p = 0.25$.

The simulations are set up starting with a circular nematic droplet, with a uniform director field and with radius between 8 and 16 lattice units, situated on a 240×120 rectangular lattice. Before the electric field is turned on the droplet is equilibrated for 64000 time steps. It relaxes to a shape with sharp tips, an aspect ratio of about two, and a bipolar director field, recovering the characteristic properties of the experimentally observed tactoids (Fig. 2.2(j)). When the field is turned on, the tactoid becomes highly extended, taking on a cylindrical shape with conical tips as shown by the series of snapshots in Fig. 2.2(k)-(o). This shape is in agreement with the experiments (Fig. 2.2(e)).

Simulation results for the time evolution of tactoids of different area are compared to experiment in Fig. 2.4, showing similar behaviour. When hydrodynamic flow was not included in the simulations it was not possible to regain the dynamics observed in the experiments, providing evidence that the long time-scales observed in the stretching of the larger tactoids are of hydrodynamic origin.

The experimental observation that the tactoid shape is independent of its volume suggests that the elastic contribution to the free energy balance is small compared to those from the surface tension and anchoring in the chitin system. For simulation parameters which reproduce the experimental results the free energy contributions due to anchoring and surface tension are similar, whereas that from the elasticity is about ten times lower in the zero field configuration.

Having validated the simulations against the experiments we can use them to investigate how the final tactoid extension depends on the anchoring strength and the strength of the applied electric field. The results, shown in Fig. 2.6, show that the extension increases strongly with anchoring strength. In zero field tactoids with zero anchoring strength are round with a uniform director field and they are unperturbed by the field, as expected. For larger anchoring strengths ($L_0 = 0.04$ to 0.06 in simulation units) the tactoids become spindle-like with a bipolar director configuration in zero field. Applying an electric field leads to increases in the aspect ratio, of up to a few hundred percent for $L_0 = 0.06$.

We saw no evidence of elongation at field strengths below 0.05 (in simulation units) (see Fig. 2.7), independent of the tactoid volume, suggesting that there is a small energy barrier to the initiation of stretching. To check that this was not due to the lattice pinning the long, straight interface we repeated the calculations for spherical droplets and found the same qualitative behaviour. We hypothesise that the energy barrier occurs because the strongly anchored directors at the interface need a minimum field to be able to distort the interface so that they can align with the field direction. This is supported by the fact that the energy barrier decreases with decreasing anchoring.

2.4 Summary and discussion

In summary, we have shown experimentally and by numerical simulations that the application of an electric field to nematic tactoids induces a transition from the common spindle-like shape with a bipolar director field to a cigar-like shape with an almost uniform director field. The drops extend in the direction of the field to reach aspect ratios of over ten. This is a consequence of the low elasticity and strong anchoring of the chitin tactoids.

From a practical point of view, subjecting tactoids to shear flow has been shown to improve the optical properties of liquid crystal films by enhancing the alignment of the particles [73], and using electric fields can achieve this same effect in a much more controllable environment. Indeed, when doped with acrylamide monomers, these biphasic aqueous chitin suspensions could easily be polymerised under electric field, as was recently demonstrated in the case of clay suspensions [89].

To further investigate the morphological properties of liquid crystals, and their tunability, it would be interesting to look at the coalescence of tactoids. In the experiments it was occasionally observed that tactoids may coalesce while elongating, to break up again during retraction. Since bigger tactoids react more strongly to an electric field, coalescence may be an important factor in improving alignment. Furthermore chitin tactoids offer an easily accessible confined liquid crystal environment for studying fundamental properties of liquid crystal solutions.

3

Two-dimensional, blue phase tactoids

In this chapter we use full nematohydrodynamic simulations to study the statics and dynamics of monolayers of cholesteric liquid crystals. Using chirality and temperature as control parameters, we show that we can recover the two-dimensional blue phases recently observed in chiral nematics, where hexagonal lattices of half-skyrmion topological excitations are interleaved by lattices of trefoil topological defects. Furthermore, we characterise the transient dynamics during the quench from isotropic to blue phase. We then proceed by confining cholesteric stripes and blue phases within finite-sized tactoids and show that it is possible to access a wealth of reconfigurable droplet shapes including disk-like, elongated and star-shaped morphologies. Our results demonstrate a potential for constructing controllable, stable structures of liquid crystals by constraining two-dimensional blue phases and varying the chirality, surface tension and elastic constants. This work has been published in Molecular Physics [90].

3.1 Introduction

Recent work has demonstrated the possibility of stabilising exotic topological field configurations, which cannot be deformed into a uniform field by a smooth or continuous process, in diverse physical systems [91–93]. These include skyrmions

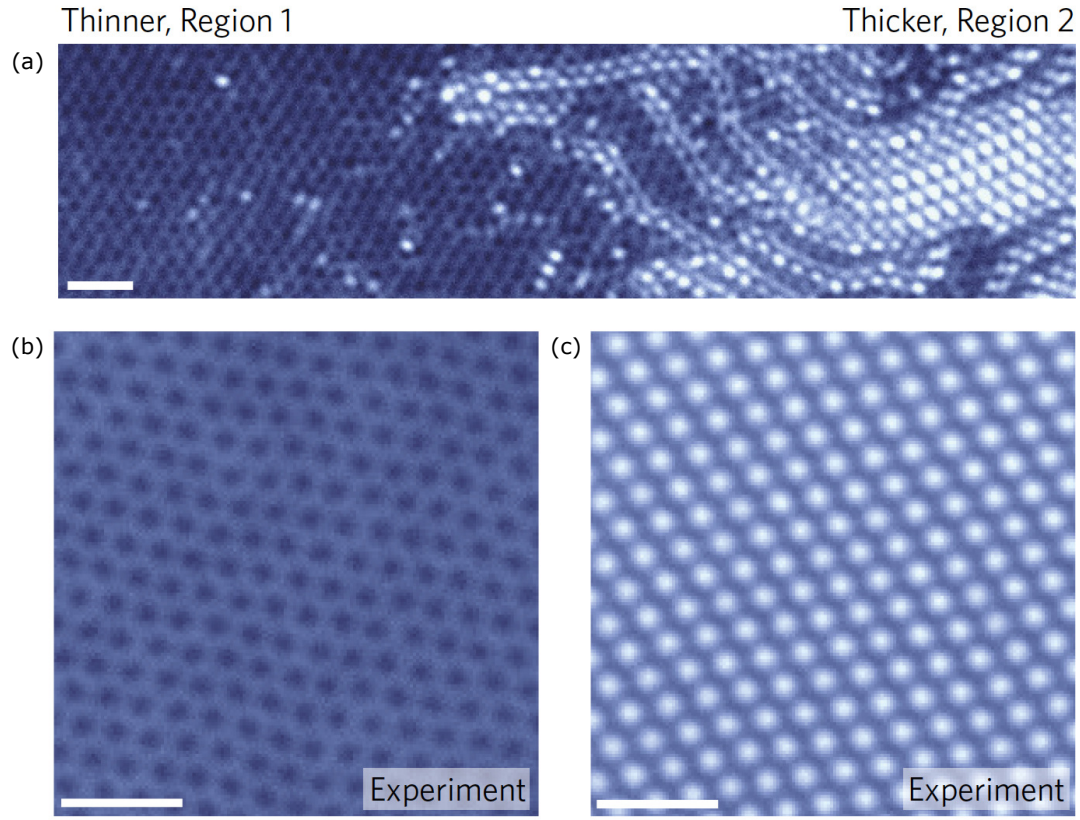

Figure 3.1: Real-space observations of the two-dimensional blue phase lattice structures in a chirally doped nematic sandwiched between two plates less than a single characteristic pitch apart. (a) Magnified view of the transition domain between "Region 1" (left) and "Region 2" (right). (b),(c) Real-space images of "Region 1" and "Region 2", respectively, with a perfect periodic structure. Scale bars, 1μm. Image taken from [97].

[23], which comprise π double twist of an order parameter radially outwards from a centre, half-skyrmions (or merons) [94], where the twist is $\pi/2$, and hopfions where the variation in the order parameter is three-dimensional. Such structures are found in chiral magnets, where they have potential applications in spintronic and magnetic memory devices, in Bose-Einstein condensates due to Rashba spin-orbit coupling [95] and in antiferromagnets, where the Dzyaloshinsky-Moriya interaction leads to weak ferromagnetism [96]. The blue phases of chiral liquid crystals, introduced in Subsection 1.1.5, are formed by ordered arrays of half-skyrmions (for hexagonal symmetry) or quarter-skyrmions (for three-dimensional cubic symmetry).

The possibility of a blue phase in two dimensions was predicted numerically [22], and has very recently been confirmed experimentally, in liquid crystals confined

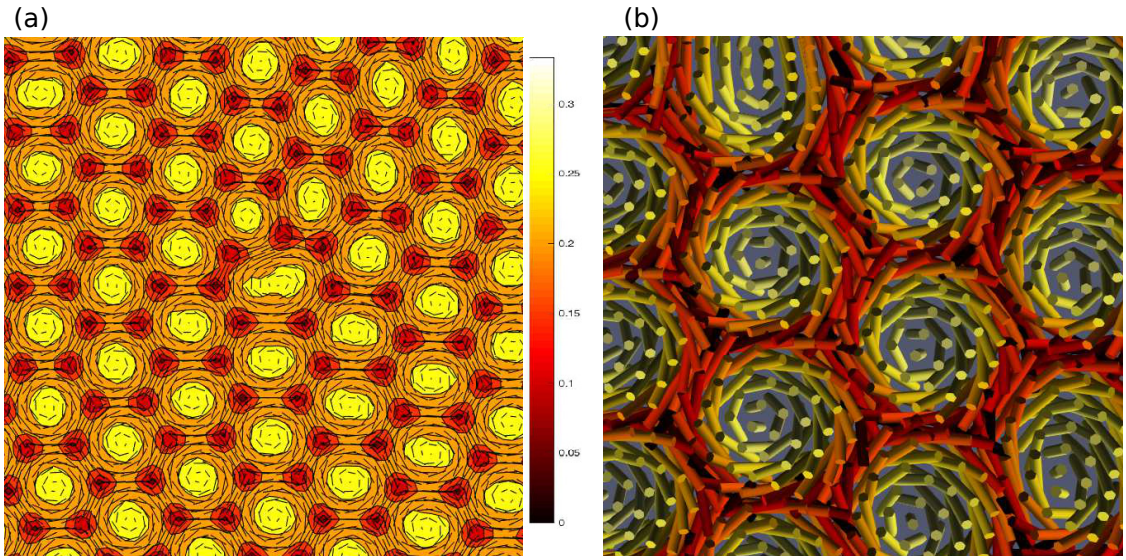

Figure 3.2: A two-dimensional blue phase with periodic boundary conditions. (a) The colour indicates the magnitude of the nematic order S_0; the half-skyrmions are yellow, and the topological defect cores appear dark red. Black lines are the projections of the director onto the plane. Imperfections in the hexatic order are due to kinetic trapping and finite size effects. (b) Magnified image of the director field. The colour coding indicates the strength of the nematic order, with yellow corresponding to a stronger orientational order.

between two plates with planar degenerate anchoring (see Fig. 3.1). The structure of the two-dimensional blue phase is a hexagonal lattice of double twist regions, (i.e. half-skyrmions), separated by an interpenetrating lattice of $-1/2$ topological defects as shown in Fig. 3.2. These experiments suggest new possibilities for studying the interplay between the properties and conformations of half-skyrmions and liquid crystalline features and structures. As a step in this direction, we numerically investigate the confinement of cholesteric and blue phases within liquid crystal droplets.

Many lyotropic liquid crystals form nematic droplets, or tactoids, liquid crystal microdomains within the isotropic phase, often as a consequence of phase ordering. Nematic tactoids take a characteristic shape, spherical or spindle-like depending on their size, because of the interplay between elastic and surface tension free energies and interfacial anchoring, as considered in Chapter 2. This suggests the possibility that novel tactoid shapes might form in a system where the bulk ordering is a two-dimensional blue phase. Therefore in this Chapter we present numerical results

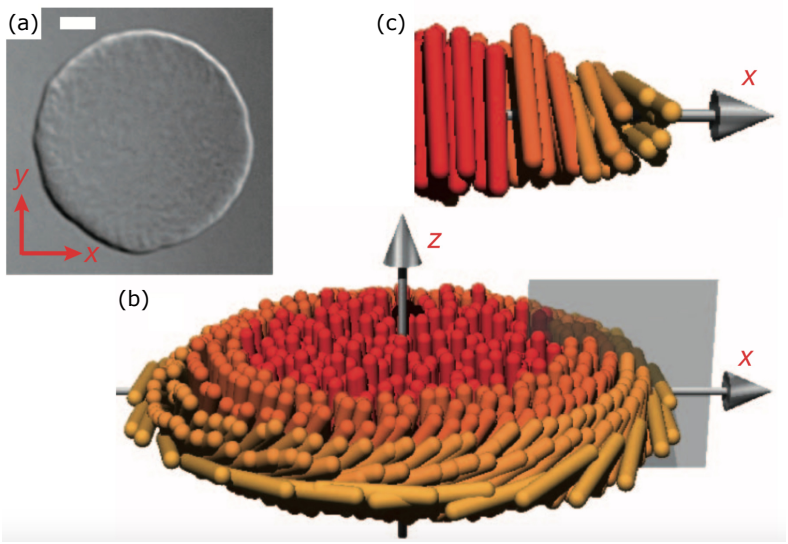

Figure 3.3: Chiral rafts assembled from fd-virus. (a) Differential interference contrast image of a fd-virus membrane. Scale bar, 5μm. (b) Schematic illustration of a colloidal membrane indicating that the rods at the edge twist away from the vertical axis in order to reduce the surface tension. (c) Cross-section shown in (b). Image taken from [98].

demonstrating the structure of two-dimensional chiral nematic tactoids as the pitch, droplet size, elasticity and the surface tension vary.

Moving to a longer length scale, colloidal liquid crystals such as finite rafts of fd-virus, have been shown to form interesting structures when on the surface of a liquid. Fd-viruses are approximately 1 μm long and 10 nm in diameter colloidal particles. In aqueous suspension they have only repulsive interactions, however, adding a non-adsorbing polymer such as Dextran leads to attractive depletion interactions between the fd rods, leading to an isotropic-nematic transition. The dense phase condenses into colloidal membranes. Here the depletion interaction means that the liquid crystal colloids prefer to point perpendicular to the surface and hence half-skyrmions are unfavourable, and the blue phase is replaced by a twist localised around the outside of the droplet (see Fig. 3.3). We show that within our model similar energetic effects can be mimicked by an external electric field, and we study the crossover from blue phase to raft-like behaviour.

This Chapter is organised as follows: first we describe our numerical approach and present a phase diagram to illustrate the region of stability of the two-dimensional blue phase, both in the absence and the presence of an external field. We also

Symbol	Description	Value
L_2	Bend/splay elastic coefficient	0.06-0.08
L_C	Twist elastic coefficient	0.04-0.16
λ	Characteristic pitch	10-46
k_ϕ	Surface tension coefficient	0.03-0.06
L_0	Interfacial anchoring	0.06
ϵ_a	Dielectric anisotropy	1
ξ	Alignment parameter	0.7
A_ϕ	Binary fluid coefficient	0.2
A_0	Landau-de Gennes coefficient	1.5
Γ_Q	Rotational diffusivity	0.7
M	Mobility	0.7
ρ	Density	1
ν	Viscosity	2/3
p	Bulk pressure	0.25

Table 3.1: Simulation parameters.

describe the dynamics of quenches from the isotropic phase into the blue phase. We next consider two-dimensional chiral tactoids and present results for their shapes and director field configurations. In the limit of a strong field we show that our results reproduce the structures seen in circular membranes of fd-virus.

3.2 Simulation method

The nematohydrodynamics approach introduced in Chapter 1 is used to study the morphology and dynamics of chiral tactoids. Compared to the achiral tactoids the elastic contribution to the free energy now includes a term dependent on λ, as introduced in Subsection 1.1.5. The coefficients used in the simulations are listed in Table 3.1.

Simulations are performed on a $L_x \times L_y \times L_z = 100 \times 100 \times 1$ lattice with periodic boundary conditions in all directions. For bulk cholesteric systems the initial configuration is a single pitch rotating around the y-axis. For tactoids, the initial configuration for the simulation is a circular droplet with a uniform director field pointing in the z-direction.

3.3 Phase diagrams

We begin by constructing phase-space plots, both without (Fig. 3.4(a)) and with (Fig. 3.4(b)) an external electric field, to illustrate the range of temperature and chiral strength ($\sqrt{L_C/\lambda^2 A_0}$) for which isotropic, cholesteric, or blue phases form. For each combination of parameters we find the lowest free energy state by running the dynamical simulation. Fig. 3.4a shows a phase diagram in zero external field for a range of reduced temperatures and chiral strengths. The reduced temperature τ is defined as $27(1-\frac{1}{3}\eta)/\eta$ in order to have τ equal to 1 at the isotropic-nematic transition. L_2 and L_C are set to 0.08 and 0.1, respectively.

As expected, at high temperatures the isotropic phase is stable, while at low temperatures the blue and cholesteric phases are formed. The cholesteric phase is favoured when the chirality is low (the pitch λ is high). Upon increasing the chirality double-twist becomes locally favourable leading to half-skyrmions. Topological defects form and organise in hexagonal lattices to release the high global elastic energy penalty of the double-twist, and a two-dimensional blue phase emerges.

Application of an external field along the z-axis shifts the ordering to that shown in Fig. 3.4(b). As strength of the external field is increased, the preference of the director field to lie out of plane along z suppresses double twist deformations and the half-skyrmion lattice becomes less stable, in favour of cholesteric patterns. Interestingly, at high temperatures and relatively small chiral strength the aligning field stabilises isolated half-skyrmions, separated by isotropic domains and without any $-1/2$ topological defects, which organise into a hexagonal lattice. This behaviour is markedly different from known simulation results for hexagonal blue phases in fully three-dimensional systems [99] or confined between two parallel plates [100]. For stronger electric fields the director field is out of plane in the entire domain and a (para)nematic phase, with alignment in the z-direction, is formed.

In order to characterise the dynamics of the blue phase formation, we investigate a quench from the isotropic state into the two-dimensional blue phase. The simulation is set up in a random state, corresponding to infinite temperature, and the temperature is instantaneously lowered to $\tau = 0.47$, while the chiral length

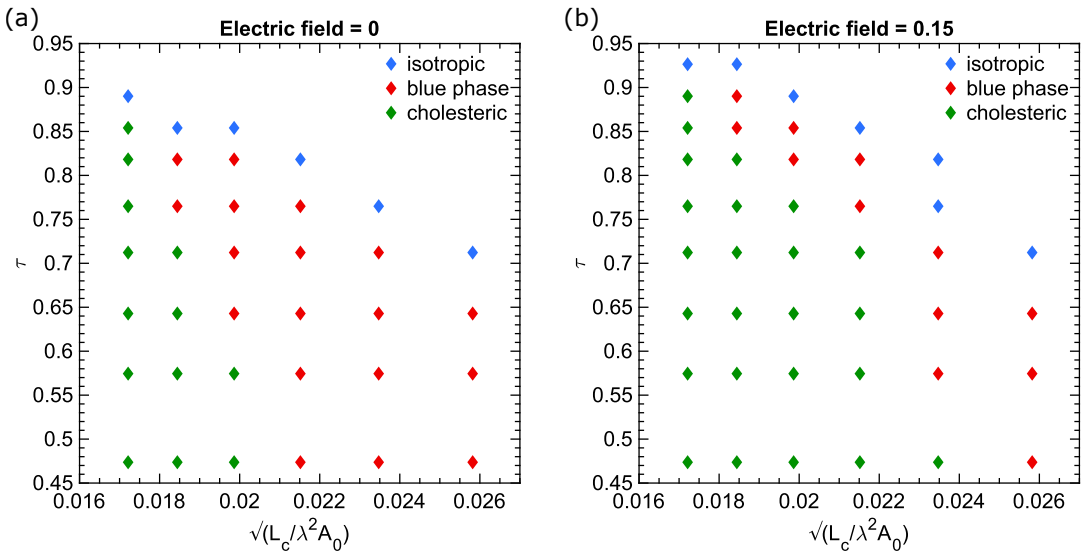

Figure 3.4: Phase diagrams for varying dimensionless pitch $\sqrt{L_C/\lambda^2 A_0}$ and reduced temperature $\tau = 27(1 - \frac{1}{3}\eta)/\eta$. (a) Zero external field. (b) External field $E = 0.15$. In the presence of the field, the two-dimensional blue phase is suppressed in favour of the cholesteric phase.

$\sqrt{L_C/\lambda^2 A_0} = 0.0235$ is kept constant at a value where the blue phase is stable. Fig. 3.5 shows snapshots tracking the temporal evolution of the transition to the blue phase, showing that it is formed through a nucleation and growth process. Measurement of the structure factor for the director field $S_{\underline{k}} = \sum_{\underline{k}} \exp(i\underline{k} \cdot \underline{n})$, shows emerging hexatic order. Compared to previous theoretical and computational studies of the formation of two-dimensional blue phases [5, 101], here we fully resolve hydrodynamic effects. Although the kinetic pathway shows minor differences, no qualitative changes in the dynamics of phase ordering are observed.

It is worth noting that the final hexagonal lattice is not perfect. This is because we do not include any thermal fluctuations in these simulations, so the system cannot overcome energy barriers, and is also due to the finite size of the simulation box, which leads to a small mismatch with the preferred period of the blue phase.

3.4 Chiral nematics in confinement

So far only bulk cholesteric and blue phases were considered. The focus now switches to the impact of confining interfaces, and the morphology of liquid crystal

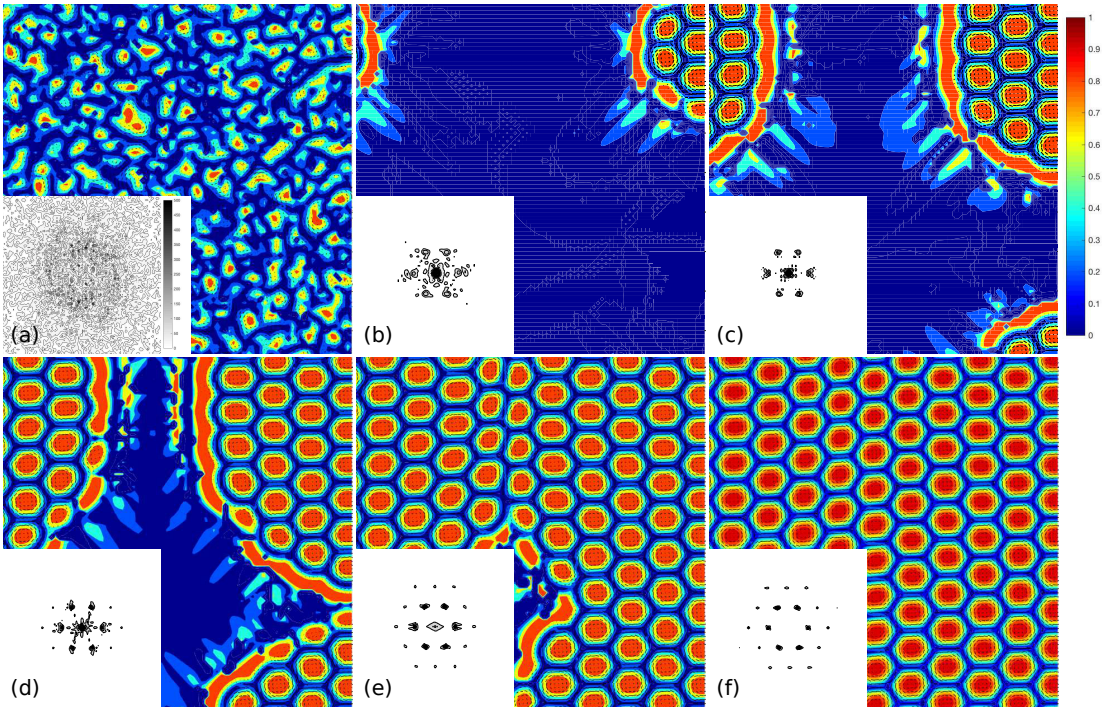

Figure 3.5: Real-space images of a quench from the isotropic phase into the two-dimensional blue phase. (a-f) are images taken 20, 400, 800, 1200, 1800 and 3000 simulation time steps after quenching. The colour coding indicates the absolute value of the projection of the director onto the direction perpendicular to the plane (z-axis). The insets in the lower left corners are Fourier transforms of the director field, indicating the relative positions of $-1/2$ topological defects (a video can be seen at https://doi.org/10.1080/00268976.2018.1496292).

tactoids by simulating droplets of chiral liquid crystal within an otherwise isotropic fluid medium. In order for the droplets to feel the confinement, the interfacial anchoring has to be non-zero, as having no anchoring would be equivalent to slicing a circular region out of an infinite domain. Therefore, in the simulations a choice has to be made for either planar or homeotropic interfacial anchoring. Here, as predicted in theory and simulations of isotropic-nematic interfaces for rod-like systems [102, 103] and in the experimental realisations [104], the anchoring is chosen to be strongly planar at the interface.

Choosing as axes the ratio of the droplet radius r to the cholesteric pitch λ and the ratio of k_ϕ, which controls the surface tension, to L_C, the twist elastic coefficient, Fig. 3.6 indicates the structures found in different regions of parameter space. The initial condition in all cases is a circular droplet with the director

pointing in z-direction: this could be achieved in experiment by applying a strong out-of-plane external field.

Panel (a) shows that for large r/λ and large twist elastic coefficient the system relaxes into a two-dimensional blue phase. Irregularities in the lattice structure near the boundaries ensure that the tactoid satisfies the planar boundary conditions without the elastic energy penalty that would be associated with strong local curvature of the interface. In panel (b) the twist elastic coefficient is smaller, which means that uniaxial cholesteric ordering becomes more favourable relative to the double twist of the blue phase. The smaller twist elastic coefficient compared to the bend-splay elastic coefficient also encourages tactoid elongation, so that the system forms a uniaxial structure in the centre, but with distorted half-skyrmions near the boundaries to better satisfy the anchoring condition. As r/λ is decreased, panels (c) and (d), uniaxial chiral ordering dominates and the droplet is strongly stretched along the chiral axis to satisfy the boundary conditions with minimal elastic energy penalty.

In panel (e), when the pitch becomes even longer compared to the droplet size, and the twist elastic coefficient is small, there is a change in behaviour, and it becomes favourable for the director to point out of plane, with a small twist at the surface. There is therefore no reason for the tactoid to elongate.

For larger twist elastic coefficient and smaller surface tension, the twist free energy dominates and the system forms a single cholesteric stripe, elongating to give the correct pitch over the short axis of the tactoid (panel (f)). For a slightly larger droplet, the stable state is a longer stripe. However, a metastable star-shape (panel (g)) can also form from a configuration where the nematogens are initially out of plane. This results from the initial dynamics which is a two dimensional twist. It is worth noting that such a metastable configuration is not possible without including hydrodynamic effects. Finally, in panel (h), double-twist regions become more favourable again, and the low surface tension allows deformations so that these can adopt the correct pitch, subject to satisfying the boundary conditions.

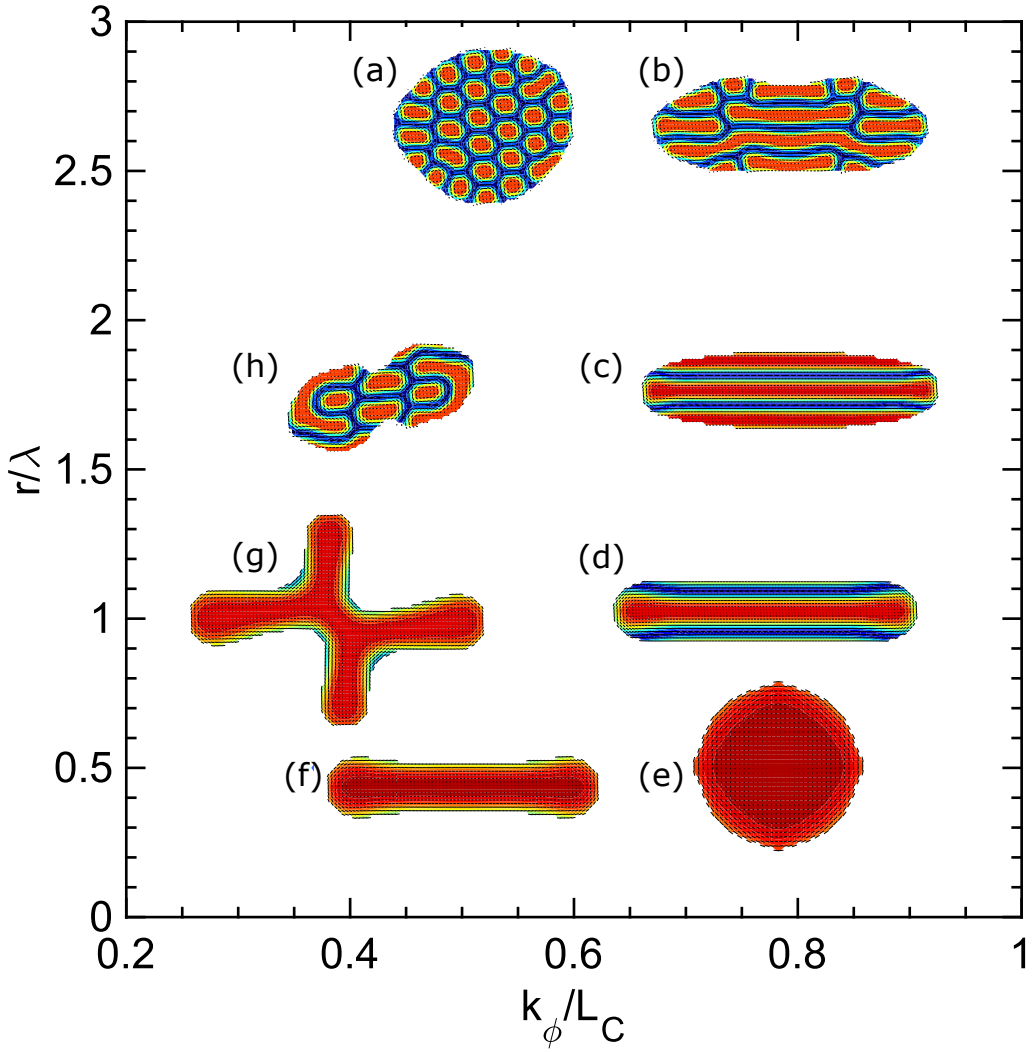

Figure 3.6: Phase diagram for cholesteric tactoids. The initial condition in all cases is a circular droplet with the director pointing in the z-direction and the bend-splay elastic coefficient is equal to 0.06 in simulation units. The colour coding indicates the absolute value of the projection of the director onto the direction perpendicular to the plane (z-axis), and black lines are the projections of the director onto the plane. The variables are droplet radius, r, cholesteric pitch, λ, surface tension coefficient, k_ϕ, and twist elastic coefficient, L_C. (a) $r = 24$, $\lambda = 10$, $L_C = 0.12$, $k_\phi = 0.06$: two-dimensional blue phase, but with defects in the lattice structure due to confinement. (b) $r = 24$, $\lambda = 10$, $L_C = 0.08$, $k_\phi = 0.06$: an elongated droplet with single-twisted domains. (c) $r = 18$, $\lambda = 15$, $L_C = 0.08$, $k_\phi = 0.06$: an elongated tactoid with cholesteric stripes. (d) $r = 24$, $\lambda = 24$, $L_C = 0.08$, $k_\phi = 0.06$: a single cholesteric stripe in an elongated tactoid. (e) $r = 18$, $\lambda = 36$, $L_C = 0.04$, $k_\phi = 0.03$: ordering predominantly along z. (f) $r = 18$, $\lambda = 36$, $L_C = 0.16$, $k_\phi = 0.06$: a single cholesteric stripe. (g) $r = 24$, $\lambda = 36$, $L_C = 0.16$, $k_\phi = 0.06$: a metastable star shape. (h) $r = 18$, $\lambda = 15$, $L_C = 0.16$, $k_\phi = 0.06$: strong deformation and local double-twist cylinders.

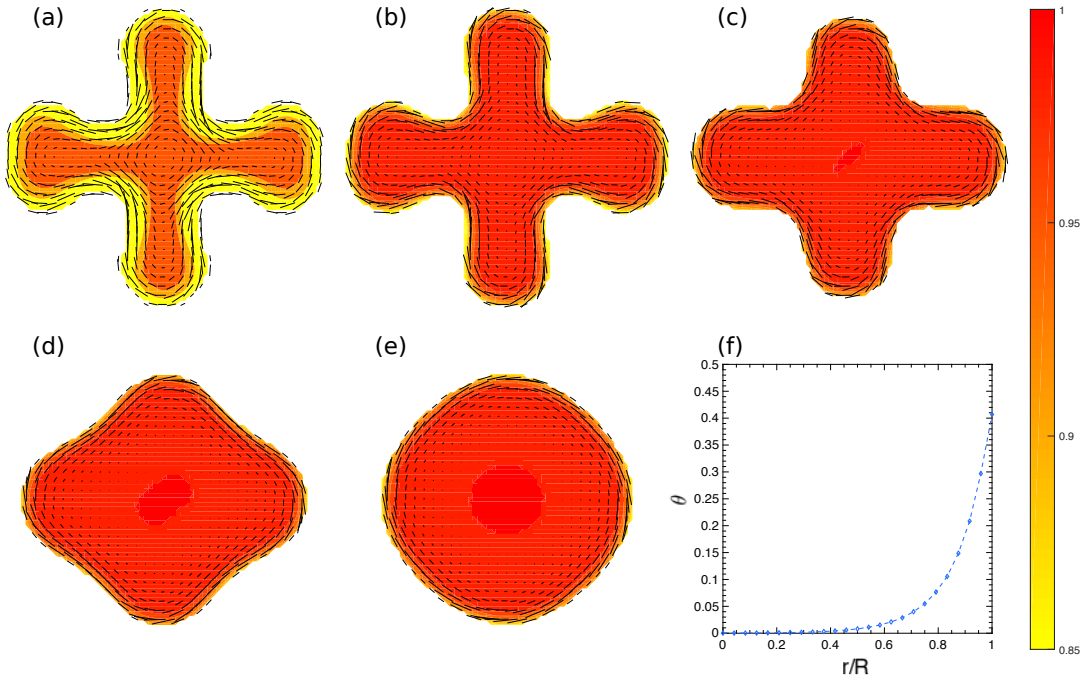

Figure 3.7: Time evolution of a star shaped tactoid after applying an external field. (a)-(e) Snapshots after 0, 200, 500, 2000 and 12000 simulation time steps. The colour indicates the value of the z-component of the director. (f) Angle of the director with respect to the z-axis 12000 time steps after application of the field, as a function of the distance from the centre of the tactoid to the edge, showing increasing twist approaching the edge.

3.5 Chiral tactoids in an external field

The tactoids in Fig. 3.6 are all stable (or metastable) in the absence of an external field. By applying a sufficiently strong field in the z-direction it is possible to align the directors out of plane. In Fig. 3.7 we follow the time evolution of a star-shaped tactoid after applying an external field. As the director aligns with the external field surface tension pulls the tactoid into a circular shape. Note, however, that there is still twist around its edges (Fig. 3.7(e)-(f)). This occurs because at the middle of the tactoid there is a competition between the aligning field and the Frank elasticity on the one hand, and the preferred chiral twist on the other. For a sufficiently strong field this leads to directors pointing along z. However, at the edge of the tactoid the relative contribution of the Frank elastic energy is less, leading to the possibility of twist.

Such an edge structure draws analogy to experimental observations of "chiral rafts" in dilute suspensions of rod-like, fd-viruses with attractive interactions induced by the addition of non-adsorbing polymers [98]. In these experiments the role of the non-adsorbing polymers is to provide attractive forces through the depletion mechanism between the otherwise repulsive rods. As a result of the depletion it is energetically favourable for the viruses to stand vertically except around the edge of the raft where twist deformations reduce the interfacial energy by lowering the polymer-virus interaction area. In our simulations, an electric field in the vertical direction mimics the depletion interaction, while at the free edges twisting results from the balance of chiral and elastic terms.

3.6 Summary and discussion

We have used nematohydrodynamic simulations of liquid crystals to study the order in, and the dynamics of, two-dimensional blue phases. In particular, we have shown that a wealth of stable morphologies can be achieved by cholesteric tactoids, liquid crystal droplets within an otherwise isotropic liquid. Bulk two-dimensional blue phases have been observed experimentally, and isolated skyrmions and hopfions have been created in cholesteric liquid crystals using optical excitations [105, 106]. Recently, confinement of cholesteric liquid crystals within three-dimensional microchannels [97, 107] and three-dimensional droplets [108] have proven successful in observing both half- and full-skyrmions without application of external stimuli. Introducing further lateral confinement in such setups could reproduce various of the stable structures reported in this study.

Another potentially relevant experimental system is the rafts of fd-virus discussed above [109]. However, due to the strong depletion interactions in these experiments it has not been possible for the rods to lie in the plane of the surface, and thus cholesteric striped, stars or blue phase rafts have not been observed so far. Carefully tuning the strength of the depletion interaction may make it possible to access other parts of the phase space considered here. Tuning of the pitch could then be achieved through manipulation of genetic or physical cues in the experiments [109]. It would

also be interesting to test for the effects of external stimuli such as an electric or magnetic field on the morphology of chiral rafts. From the theoretical point of view, one could envisage that applying the external aligning field at an angle with respect to the vertical direction could break the symmetry and lead to the formation of further exotic and controllable conformations. Similarly, applying mechanical forces could be a potential mechanism for building chiral macrostructures as was partly explored for chiral rafts, where applying extensional forces by optical traps was shown to create double or triple helices in the experiments [109].

Finally, the next step in studying exotic tactoids is to investigate the interaction between different morphologies and the coalescence of such tactoids to construct hierarchical structures. Such structures have already been shown to successfully form from coalescence of chiral rafts of fd-viruses [110].

4

Topological states in chiral active matter: dynamic blue phases and active half-skyrmions

In Chapter 3 we have shown simulations of passive monolayers of cholesteric liquid crystals. In particular, we were able to recover the two-dimensional blue phases recently observed in experiments. In this Chapter we extend this work by introducing activity: we consider a chiral liquid crystal which extracts energy from its surroundings and converts it into mechanical work. In active nematics the active stress is proportional to the nematic tensor. The active force is therefore proportional to gradients in the nematic tensor. In the ground state of a two-dimensional blue phase there are gradients everywhere in the system, which leads to interesting dynamics. Here, we characterise the dynamical response of two-dimensional blue phases and isolated half-skyrmions when introducing active stresses. This work has been published in The Journal of Chemical Physics [111].

4.1 Introduction

Previous studies of active liquid crystals have mostly focused on achiral particles. In nature, chirality is ubiquitous, ranging from the helical structure of DNA [112] and bacterial flagella [113] to numerous biopolymers such as actin, chitin and

microtubules [114]. On a more macroscopic level, the mitotic spindle is chiral due to torques within microtubule bundles [115], cells can develop chiral actomyosin patterns [116], and there is even tissue-scale chirality in spontaneous cellular shear flow [117]. Motivated by this common occurrence of chirality in biological systems, in this Chapter the combined effects of activity and chirality on pattern formation within active chiral liquid crystals are explored.

We simulate quasi-two-dimensional active chiral liquid crystals. We show that stable vortex lattices form due to the presence of internal chiral structure in an active two-dimensional blue phase, and demonstrate a threshold for dissociation into unbound vortices for the case of extensile activity. For contractile activity, however, the vortex lattice remains stable for any activity strength considered. Furthermore, we compare analytical and computational flow-fields around isolated active half-skyrmions in an isotropic background, and show that these structures are stable under contractile activity, but unstable for the case of extensile activity. This is consistent with the suppression of the splay instability reported for active cholesterics [118], but can more intuitively be understood in terms of the stability of the half-skyrmions. Finally, we simulate an active two-dimensional blue phase in square confinement, finding a dynamically ordered state where the blue phase rotates collectively as a coherent macroscopic unit.

4.2 Governing equations

In the previous two Chapters quasi-two-dimensional membranes of a passive nematic and cholesteric liquid crystal were simulated using a nematohydrodynamic approach. Here, the same nematohydrodynamic equations of liquid crystals are used, considering only a single phase, and modified to account for the stresses generated by active constituent elements [44, 118]. As was argued in Subsection 1.2.1, the active stress is proportional to the nematic tensor $\underline{\underline{\sigma}}_{\text{active}} = -\zeta\underline{\underline{Q}}$, such that any gradient in the nematic tensor generates a flow field, with strength determined by the activity parameter, ζ. Positive ζ corresponds to extensile activity, and negative ζ to contractile activity. Explicit chiral active terms such as those introduced in [119]

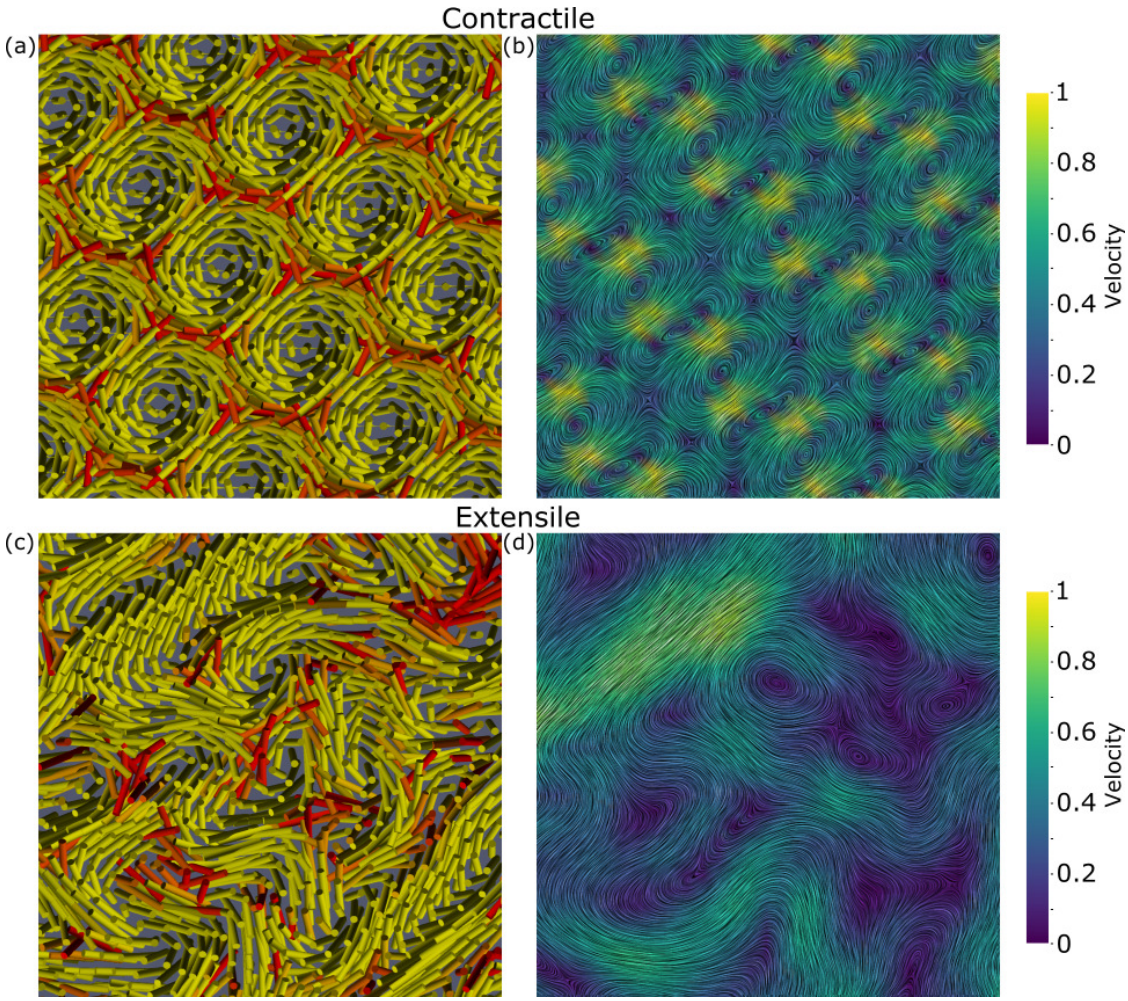

Figure 4.1: An active two-dimensional blue phase with periodic boundary conditions. (a),(c) Director field, coloured by the magnitude of the order, ranging from disordered (red) to strongly ordered (yellow) for (a) contractile activity and (c) extensile activity. (b),(d) Velocity streamlines, coloured by the magnitude of the velocity normalised by its maximum value, ranging from slow (blue) to fast (yellow) for (b) contractile activity and (d) extensile activity. The contractile two-dimensional blue phase sets up a stable vortex lattice (a), (b). The high velocities in (b) coincide with the locations of the -1/2-defects in (a). The half-skyrmions in the extensile two-dimensional blue phase have dissociated, and the system is in an active turbulence regime (c), (d). Videos can be seen at https://doi.org/10.1063/1.5085282

are not necessary in the case considered here. The two-dimensional nematic tensor under consideration in [119] cannot accommodate any twist, and can therefore not be chiral. That makes it necessary to put in chiral terms in the evolution equation for the nematic order parameter and a chiral active stress in the flow equation to obtain chiral dynamics. In our work, we use the full three-dimensional nematic tensor, meaning that the chirality in the flow equations can enter through $\zeta \underline{\nabla} \cdot \underline{\underline{Q}}$. Moreover, in our active stress there is no contribution from active torques [120], as could arise for example in E. coli bacteria due to the counter-rotation of head and tail. Instead, in here only the combined effects of active force-dipoles and passive chirality of the particles are studied.

4.3 Results

4.3.1 Dynamic blue phases

The active nematohydrodynamics equations (1.28), (1.29) and (1.23) are solved using the hybrid lattice Boltzmann method set out in the introduction (Section 1.3). We are considering only a single fluid, so in contrast to the previous two Chapters 2 and 3, the order parameter ϕ and the associated Cahn-Hilliard equation (1.26) do not have to be used. The time step and lattice spacing are set to unity. The parameters used are $A_0 = 1.5$, $\gamma = 2.85$, $L_2 = 0.04$, $L_C = 0.085$, $\lambda = 10.3$, $\Gamma_Q = 0.7$, $\xi = 0.5 - 0.9$, $\nu = 2/3$, $\rho = 1$, $p = 0.25$, in lattice Boltzmann units. The pitch λ and the inverse pitch $q_0 = 2\pi/\lambda$ will be used interchangeably. A two-dimensional velocity field is modelled, but in order to allow for twist the director is free to point in three dimensions.

An example of the response to activity for a rod-like system with $\xi = 0.9$ is shown in Fig. 4.1. Upon application of contractile activity, the director field deforms from a double-twist cylinder configuration to a vortex-like "swirl" (Fig. 4.1(a), and Fig. 4.2 for a schematic). The swirls all generate rotational flow with the same handedness, with regions of opposite vorticity in between (Fig. 4.1(b)). This type of vortex lattice is remarkably similar to those reported in active nematics with substrate friction

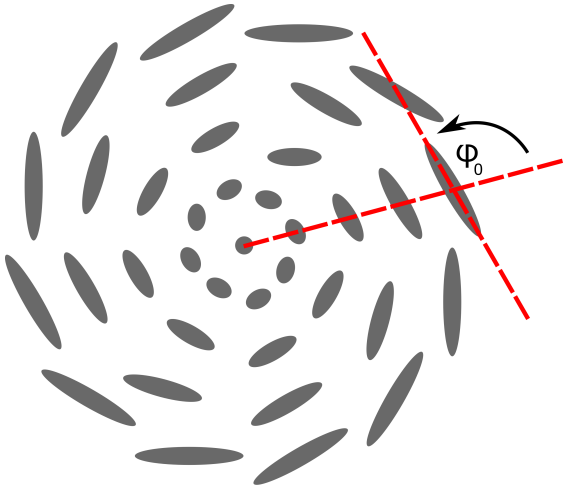

Figure 4.2: Top view of a single half-skyrmion. The director twists through an angle of $\pi/2$, from a vertical orientation in the centre of the half-skyrmion to a horizontal orientation at the edge. The angle ϕ_0 is $\pi/2$ in equilibrium, but changes under influence of activity, leading to a "swirl"-like profile.

[121], where hydrodynamic screening stabilised the vortices, while here the additional length introduced by the intrinsic pitch of the cholesteric sets the vortex scale.

The hexagonal structure of the two-dimensional blue phase is stable for all contractile activity strengths considered. Fig. 4.3(a) shows the velocity-velocity correlation function $C_{uu}(r) = \langle \underline{u}(r,t) \cdot \underline{u}(0,t) \rangle / \langle \underline{u}(0,t)^2 \rangle$ for a range of contractile activities, where $r = \sqrt{x^2 + y^2}$. There is order over several pitch lengths. The vorticity-vorticity correlation function $C_{\omega\omega}(r) = \langle \underline{\omega}(r,t) \cdot \underline{\omega}(0,t) \rangle / \langle \underline{\omega}(0,t)^2 \rangle$, where $\underline{\omega}$ is the vorticity, shows the same behaviour (Fig. 4.3(b)).

These two-dimensional blue phases are however unstable to extensile active stresses. An example of the director field (Fig. 4.1(c)) and the velocity field (Fig. 4.1(d)) show that under sufficiently large extensile activity the two-dimensional blue phase breaks up and active-turbulence-like behaviour emerges. This is further exemplified by the velocity-velocity correlation functions in Fig. 4.3(c), which show a reduction in order with increasing extensile activity. Fig. 4.3(d) shows something unexpected, however: even though for intermediate extensile activities the correlation functions show that order over multiple pitch lengths is lost, the vorticity-vorticity correlation function still indicates the existence of a well-defined coherence length. This is because the active turbulence state is first developed for

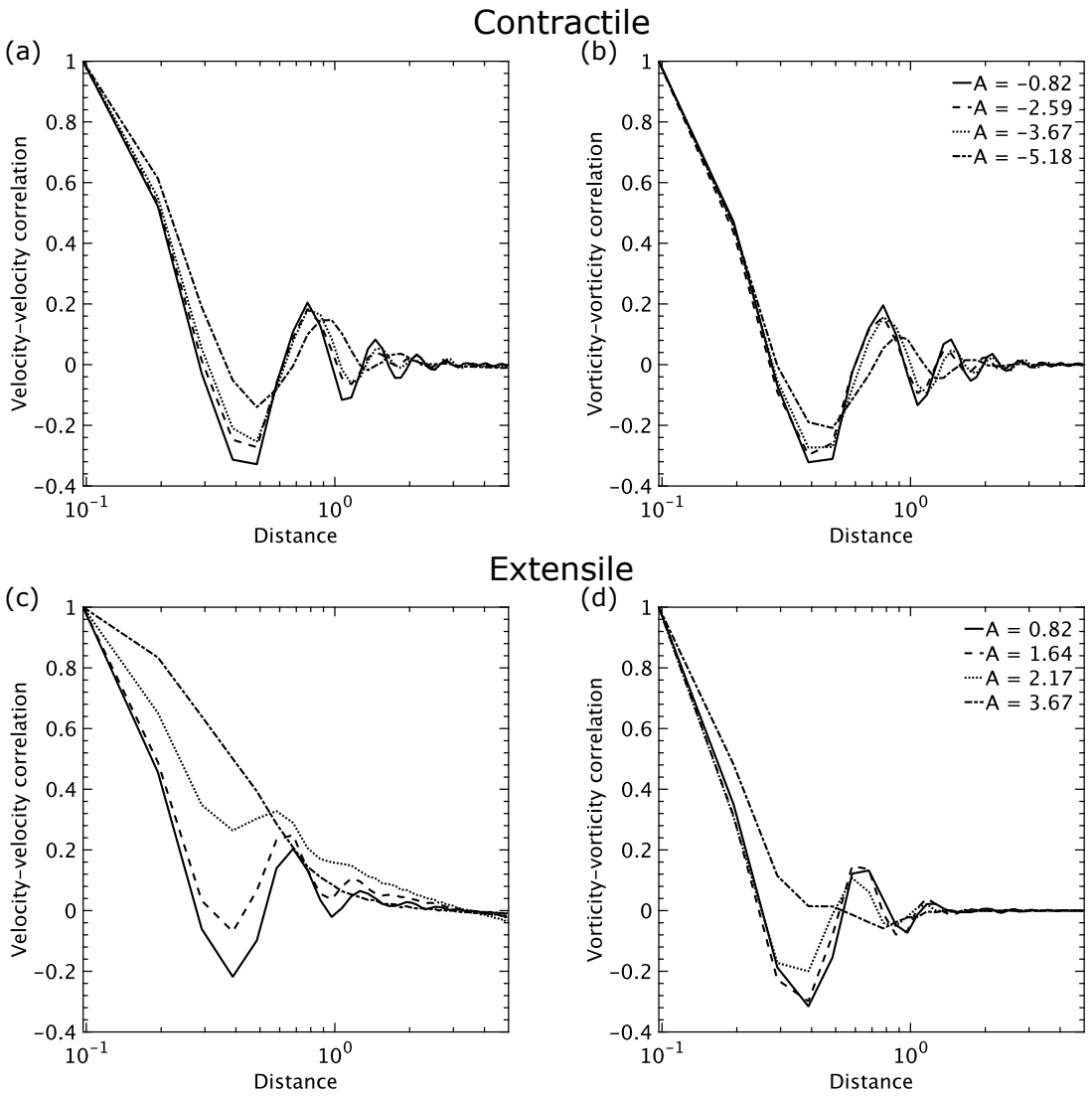

Figure 4.3: Correlation functions for (a),(b) contractile and (c),(d) extensile activities. The distance has been scaled with respect to the characteristic pitch $\lambda = 2\pi/q_0$. The dimensionless activity number $A = \pm\sqrt{\zeta/L_2 q_0{}^2}$ characterises the ratio between the characteristic pitch and the active length scale $\sqrt{L_2/\zeta}$.

relatively coherent patches with the half-skyrmions moving as coherent units, in a turbulent-like fashion. Only for larger activity numbers this coherence is lost.

In addition, measurements of the number of half-skyrmions in the system highlight the difference between contractile and extensile driving (Fig. 4.4). For contractile systems the number of half-skyrmions does not change substantially with increasing activity. The small increase in the number density is due to the stabilising effect of the contractile activity which helps the lattice become more regular so that it can fit slightly more half-skyrmions. For extensile systems, however, the

behaviour is different. The initial increase in the number of half-skyrmions for extensile activity is due to the break up of short cholesteric stripes, which are present at low activity. More importantly, the number density of half-skyrmions drops significantly when the coherence is lost. The dissociation of half-skyrmions and onset of active turbulence occurs at approximately $\zeta_{\rm cr} \approx 4L_2{q_0}^2$ ($A_{\rm cr} \approx 2$) and it is accompanied by a faster increase in the root mean squared velocity $u_{\rm rms}$ (Fig. 4.4; *inset*). This threshold can be explained by considering the competition between the pitch length set by the intrinsic chirality of the particles $\lambda = 2\pi/q_0$, and the active length scale set by the activity ζ and orientational elasticity L_2 of the system, $l_{\rm active} \sim \sqrt{L_2/\zeta}$. As the activity is increased to the level where the active length scale becomes smaller than the pitch length, the half-skyrmions break up and the active turbulence is established. The number of half-skyrmions does not go to zero in the active turbulence regime, since there is no topological difference between a double-twist cylinder and a cholesteric stripe of finite length. In order to explain the different behaviour for contractile and extensile systems, an isolated active half-skyrmion in an isotropic background is considered next.

4.3.2 Isolated half-skyrmions

4.3.2.1 Theory

A single half-skyrmion in an isotropic fluid can be approximated with an analytical model. Moving radially outwards, the director twists through an angle of $\pi/2$, from a vertical orientation at the centre of the skyrmion to a horizontal orientation in the azimuthal direction at the edge. The director field can be written as $\underline{n}(\underline{r}) = (\cos\Phi(\phi)\sin\Theta(r), \sin\Phi(\phi)\sin\Theta(r), \cos\Theta(r))$, where the polar coordinates $\underline{r} = (r\cos\phi, r\sin\phi)$ are introduced, and $\Phi(\phi) = \phi + \phi_0$ (with $\phi_0 = \pm\pi/2$ depending on handedness), and $\Theta(r) = r/R$ for $0 \leq r \leq R\pi/2$.

Considering the three elastic modes, splay, twist and bend, we write the Frank elastic free energy in terms of the director field $\underline{n}$,

$$f_{\rm Frank} = \frac{K_1}{2}\left(\underline{\nabla}\cdot\underline{n}\right)^2 + \frac{K_2}{2}\left(\underline{n}\cdot\underline{\nabla}\times\underline{n}\right)^2 + \frac{K_3}{2}\left(\underline{n}\times\left(\underline{\nabla}\times\underline{n}\right)\right)^2, \qquad (4.1)$$

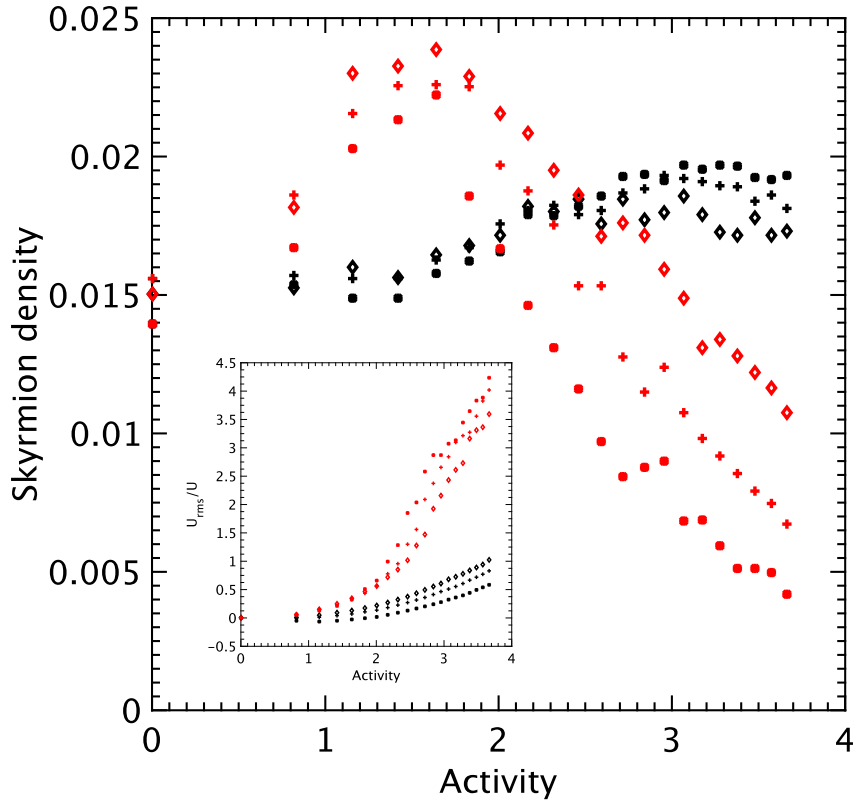

Figure 4.4: The skyrmion density, defined as the number of skyrmions per unit area, averaged over time and over five different initial configurations. Black symbols are for contractile activity, and red symbols for extensile activity. The tumbling parameter ξ is 0.5 for diamonds, 0.7 for crosses and 0.9 for squares. Above a critical activity $A_{\rm cr} \sim \sqrt{\zeta_{\rm cr}/L_2{q_0}^2}$ the vortices dissociate in the extensile system and the number of skyrmions starts decreasing. As shown in the inset, the root mean squared velocity in the extensile systems increases faster above the critical activity. The root mean squared velocity is scaled by $U = L_2{q_0}^3/\eta$.

as we introduced in equation (1.9). Inserting the director field in equation (4.1) it can be readily seen that a half-skyrmion is free of splay, but not of bend. It is well established that contractile stresses in active nematics drive an instability of the nematic state to splay deformations, while extensile stresses yield bend deformations [44]. In active chiral nematics however, the cholesteric order contributes a passive bend term that acts to screen the nematic splay mode. Instability only sets in when the activity exceeds a threshold, and only for extensile activity [118]. Due to the cholesteric order in half-skyrmions, it can therefore be expected that a half-skyrmion is unstable to extensile stresses above a finite threshold in activity, but stable to contractile stresses.

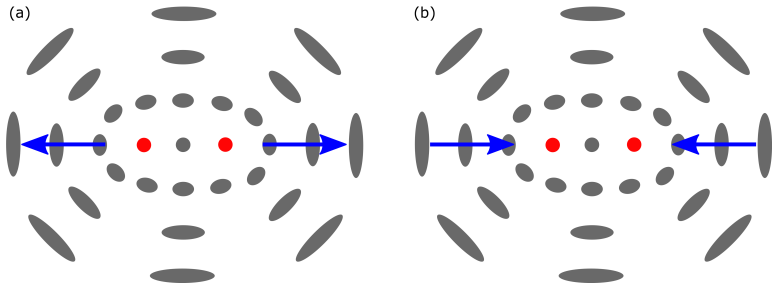

Figure 4.5: Schematic of the half-skyrmion (with topological charge +1) split into two λ^+ defects. The approximate locations of the defects are indicated by red dots, and the blue arrows show the direction in which they self-propel. (a) Extensile active stresses lead to defects moving in the direction of their "heads", thus destabilising the half-skyrmion. (b) Contractile active stresses cause the defects to self-propel in the direction of their "tails", stabilising the half-skyrmion.

An intuitive way to understand the stabilising effect of contractile stresses observed in the simulations is by considering that a half-skyrmion is topologically equivalent to a +1 topological defect. (Fig. 4.5). In the language of cholesteric liquid crystals the half-skyrmion can be split into two λ^+ defects. In contrast to +1/2 topological defects the director field is continuous at a λ^+ defect and it is instead the cholesteric pitch axis which is discontinuous. If the +1 topological charge is split into two λ^+ defects, the direction of spontaneous motion of active λ^+ defects can be used to interpret the observed behaviour: extensile active stresses drive the two defects apart (Fig. 4.5(a)), whereas contractile active stresses push the two defects together (Fig. 4.5(b)). Since the undeformed half-skyrmion is a topological excitation without a singularity at its centre, introducing λ^+ defects will come with an energy cost. This explains the existence of a threshold for vortex dissociation in extensile systems.

It is obvious from a simple calculation that the undeformed half-skyrmion director field cannot generate rotational flow. If the Stokesian regime of the Navier-Stokes equation (1.29) is considered, and the elastic terms in the stress tensor that generate backflow are neglected, the velocity obeys

$$\nu\Delta\underline{u} - \underline{\nabla}p = -\underline{f} = \zeta\underline{\nabla}\cdot\underline{\underline{Q}} = \frac{3S_0\zeta}{2}\underline{\nabla}\cdot\underline{nn}, \tag{4.2}$$

using the definition of $\underline{\underline{Q}}$. The radial component of the force will be balanced by the pressure because of incompressibility, and the azimuthal gradient of the pressure is

zero due to symmetry. The equation that has to be solved is therefore simply

$$\nu\Delta u_\phi = -f_\phi = \frac{3S_0\zeta}{2rR}\sin\frac{r}{R}\left(r\cos\frac{r}{R} + R\sin\frac{r}{R}\right)\sin 2\phi_0. \tag{4.3}$$

The symmetry of the undeformed director field, with $\phi_0 = \pm\pi/2$, cannot give rise to a flow ($u_\phi = 0$). However, if the constant phase in $\Phi(\phi)$ is now perturbed, this will lead to a rotational flow.

The change in the constant phase is due to the director field deforming from pure bend deformations (in order to adapt the preferred twist) to a configuration that also accommodates splay to counterbalance the forces generated by the active stress. The case with constant phase $\phi_0 = \pi/4$ deserves particular attention since it corresponds to the bend-splay +1 defect that has recently been studied in the context of living liquid crystals [122]. It was shown that a sufficiently high concentration of bacteria swimming through a predesigned pattern of a background liquid crystal gets attracted to a +1 bend-splay topological defect and forms a rotational flow around the core of the defect. Assuming boundary conditions $u_\phi(r = 0) = 0$ and $u_\phi(r = R\sqrt{e}) = 0$, the velocity field of highly concentrated bacteria moving around the defect core was found to follow $u_\phi = \frac{3S_0\zeta r}{16\nu}\left(-1 + 2\log\frac{r}{R}\right)$ for a two-dimensional director field in the background liquid crystal, where there was no out-of-plane component. For the bend-splay half-skyrmion considered here, we find that the velocity is $u_\phi = \frac{3S_0\zeta r}{16\nu}\left(-1 + 2\log\frac{r}{R} + 2\mathrm{Ci}(2\sqrt{e}) - 2\mathrm{Ci}(\frac{2r}{R})\right)$, with the cosine integral corrections due to the fact that the director is now varying in the out-of-plane dimension.

4.3.2.2 Simulations

The analytical result is only valid for single half-skyrmions and does not take into account the interactions between the half-skyrmions, nor the presence of the six $-1/2$-defects surrounding each cylinder in a blue phase. Therefore, in order to provide a closer comparison between our analytical prediction and the numerical results, half-skyrmions in an isotropic background are simulated by quenching from infinite temperature to $\gamma = 2.74$, with $q_0 = 2\pi/13$, and applying an external

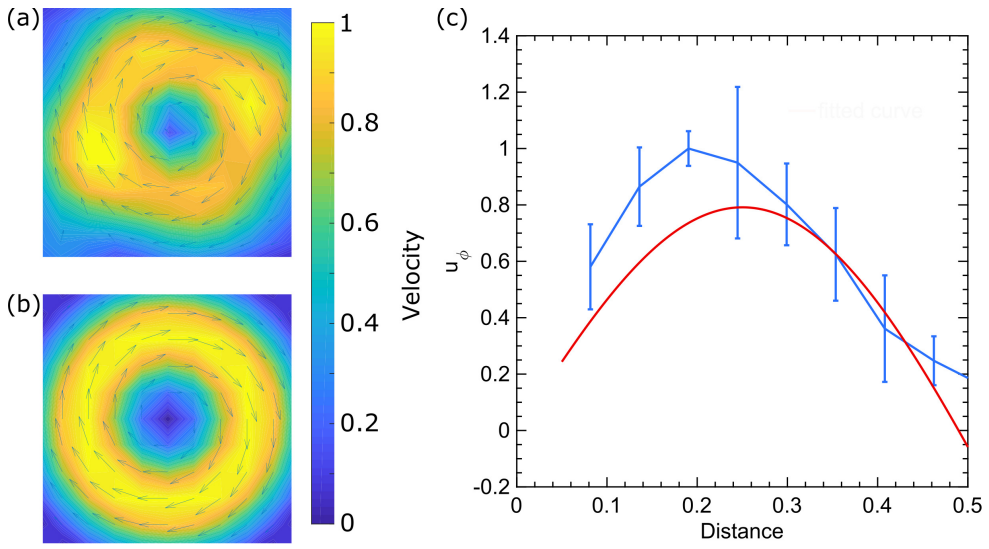

Figure 4.6: The velocity field around an isolated active half-skyrmion from (a) simulations and (b) analytics. The arrows indicate the direction of the flow, with the vector length and the background colour indicating the magnitude normalised by the maximum velocity. (c) The radial average of the azimuthal velocity from the simulation (blue, with errorbars), and the velocity from the analytics (red). The distance is scaled by the characteristic pitch.

field in the out of plane direction to stabilise the half-skyrmion, as mentioned in Section 3.3. To this end an external field free energy, introduced in equation (1.11), $f_{\text{electric}} = -\epsilon_a E_i Q_{ij} E_j$ is added to the total free energy, where the dielectric anisotropy $\epsilon_a = 1$ and $\underline{E} = 0.15\hat{z}$ is the applied external field. The resulting velocity field for a contractile activity $A = -3.27$ is shown in Fig. 4.6(a). In the analytical model the change in the magnitude of the nematic order parameter $\underline{\underline{Q}}$ going from a half-skyrmion cylinder into the isotropic phase was neglected, but nevertheless pleasing agreement with the simulation results is observed (Fig. 4.6). It should be noted that the model only holds for contractile activity or small extensile activity. In case of large extensile activity the approximation that the director field is constant in time is no longer valid.

4.3.3 Coherent rotation of a confined active blue phase

When active matter is confined, the otherwise turbulent-like motion can become coherent. For example cell monolayers [123], dense bacterial suspensions [124], and

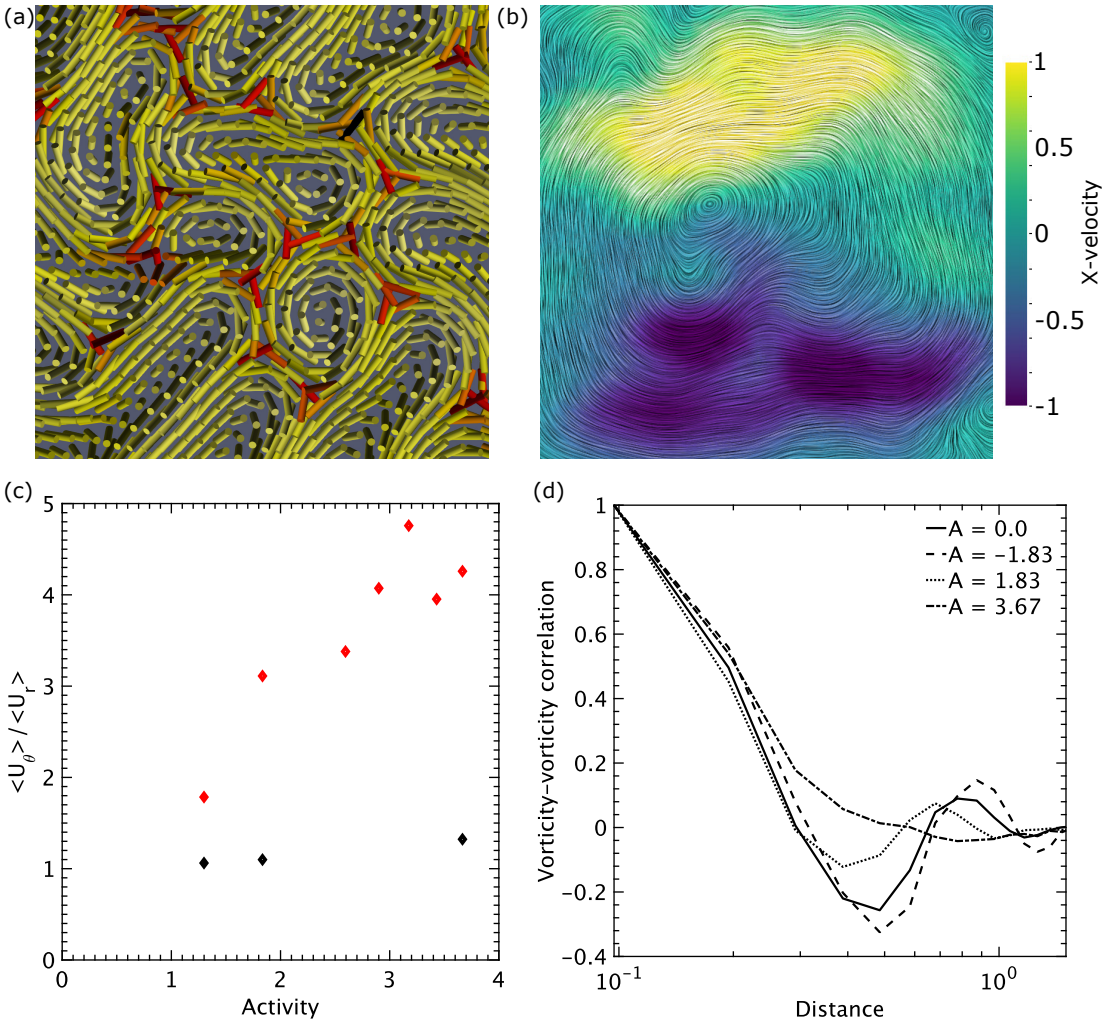

Figure 4.7: Active two-dimensional blue phases in 30×30 square confinement. Below the dissociation threshold extensile activity ($A = 1.83$) will leave half-skyrmions intact (a) and sets up a global rotational flow (b). The director field in (a) is coloured by the magnitude of the order, from disordered (red) to strongly ordered (yellow). The streamlines in (b) are coloured by the horizontal component of the velocity normalised by its maximum value, ranging from flowing to the left (blue) to flowing to the right (yellow). (c) The average orthoradial velocity divided by the average radial velocity shows that extensile activity (red diamonds) leads to coherent rotational motion, which is not present in the case of contractile activity (black diamonds). (d) The vorticity-vorticity correlation functions show that small extensile activity leaves the internal structure of the two-dimensional blue phase intact. The distance is scaled by the characteristic pitch. Videos can be seen at https://doi.org/10.1063/1.5085282

microtubule/kinesin motor mixtures [125] can all self-organise into a single circulating unit inside a circular or square box. Therefore, it is natural to ask if the active blue phase can behave in a similar way. Staying below the dissociation threshold in an extensile system, the half-skyrmions stay largely intact (see Fig. 4.7(a)), and indeed move collectively to set up a coherent rotational flow (see Fig. 4.7(a),(b)). The emergence of coherent rotation is best illustrated by calculating the ratio of the average orthoradial to radial velocity (Fig. 4.7(c)). For extensile activity above the dissociation threshold circulation persists (Fig. 4.7(c)), but without the hexagonal symmetry found in the two-dimensional blue phase. This is evident from the vorticity-vorticity correlation functions in Fig. 4.7(d) (*dashed-dotted line*), which show that for large extensile activity the coherence is lost. For contractile activity no coherent rotational flow is observed as the blue phase remains unperturbed.

4.4 Discussion

Combining active stresses of self-propelled particles with two-dimensional helical ordering in the blue phase provides a framework for studying non-equilibrium topological states in active matter. Compared to the few existing theoretical works that treat chiral active materials [118–120, 126, 127], here the topological states in chiral liquid crystals are explicitly introduced and connect the director structure to the resulting dynamics. The half-skyrmions are stable to contractile stresses, but there is an active instability threshold for extensile active particles analogous to the pitch-splay mode in active cholesterics. This can be understood by regarding the topological excitation as a +1-defect that has escaped into the third dimension. A small perturbation will lead to two +1/2-defects, which are driven apart for extensile active stresses but driven together for contractile active stresses. For small extensile activity, the half-skyrmions do not dissociate, and they set up a coherent rotational flow when enclosed, reminiscent of collective cell behaviour in confinement.

A number of directions for future work can be envisaged. For instance, the linear stability analysis performed for active nematics, smectics and cholesterics could be extended to the two-dimensional blue phase, introducing new symmetries to the

framework. Secondly, the third dimension could be made finite, both in a linear stability analysis and in simulations, to study the onset of active instabilities along the axis of half-skyrmions. Thirdly, a three-dimensional active blue phase could be simulated to investigate whether these are also stable to contractile active stresses.

5
Anisotropic friction

In this chapter we numerically study the effect of anisotropic friction on the flow behaviour of active nematic liquid crystals. Anisotropic friction is one of the methods by which active turbulence can be "tamed", that is, by which the intrinsically chaotic flow can be directed and potentially put to use. We show that we can reproduce experiments by Guillamat et al. [128], showing a clear crossover from an active turbulence state to a laning active nematic state, with well-defined flow directions by means of an anisotropic friction pattern. We further demonstrate that the occurrence of a laning active nematic state is strongly sensitive to the friction ratio. We provide some ideas for how the transition into lanes might be understood, and suggest future studies into more complicated friction patterns and comparison with interfacial anchoring as a guidance mechanism.

5.1 Introduction

Taming active turbulence has been an active research topic over the past few years. Linear stability analysis shows that a two-dimensional extensile (contractile) active nematic is unstable to bend (splay) deformations [44, 129, 130]. This means that in infinite systems the fully aligned nematic state is unstable to any level of activity. The stability analysis cannot predict the final state of the system, but numerical

simulations have shown that there is a transition to active turbulence [131, 132], with a decay in the velocity-velocity correlation function that is captured by a mean field model [51] and that was recently recorded in experiment [133]. This is a valuable insight from a theoretical point of view, but also immediately points to the challenge of constraining and directing active materials.

In an experimental system pioneered by the Dogic group [14], a two-dimensional active nematic is obtained by concentrating a bulk active gel consisting of a microtubule-kinesin mixture. By adding in a non-adsorbing polymer, depletion forces concentrate the microtubule-kinesin mixture toward a biocompatible and soft interface (see Fig. 5.1(a)). The active nematic layer can then be brought into contact with oils of different viscosities [134]. Higher viscosity will increase the number of defects, which is consistent with the insights from simulations of active nematics that include substrate friction [121, 135].

The increase in the defect density can be understood most easily from a one-dimensional argument. Consider a one-dimensional system ranging from $y = 0$ to $y = L$ with periodic boundary conditions. The nematic director can now be written in terms of an angle with the x-axis and is a function of y alone, $\theta(y)$. Active stresses will generate flows in the x-direction when there is a gradient in y-direction. If we now consider a balance between the dissipative terms in the flow equation and a point source F generating flow at $y = y_0$, we see that $\nu \frac{\mathrm{d}^2 u_x}{\mathrm{d}y^2} - f u_x = F\delta(y - y_0)$, where f is a substrate friction coefficient. This indicates an exponential relaxation of velocity over a dissipative length scale $l_{\mathrm{screen}} = \sqrt{\nu/f}$. For small friction coefficients this scale is not relevant, but for large friction coefficients the velocity is expected to decay over much shorter length scales than can be expected from viscous damping alone.

In one dimension increasing the friction coefficient (and hence decreasing the dissipative length scale) leads to a decreasing distance between shear walls and bend deformations. In two dimensions, the same mechanism, a decreasing dissipative length scale, reduces the spacing between walls formed in the active nematic, and thus increases the number of defects in the steady state. Note that the viscosity considered in the above is the viscosity of the active nematic layer itself, while

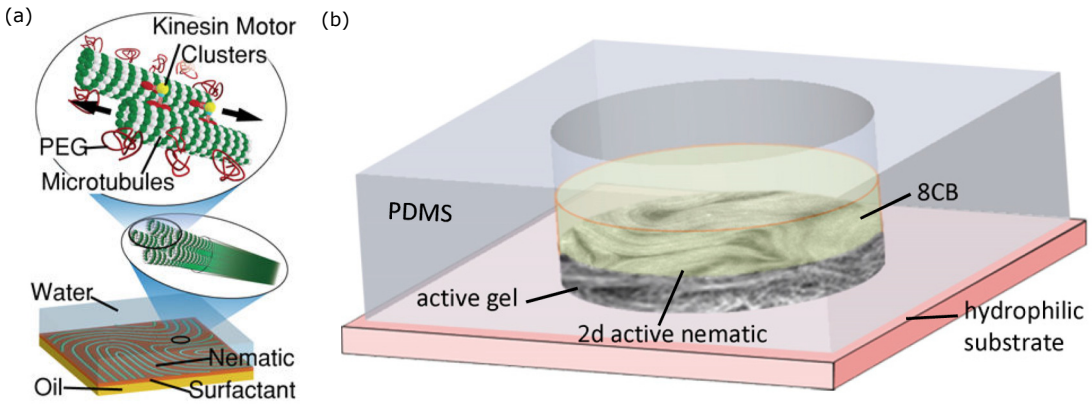

Figure 5.1: Overview of the microtubule-kinesin experimental system. (a) Microtubules are bundled together by the depletion agent PEG. Kinesin clusters crosslink microtubules and induce interfilament sliding. Bundles are confined to a surfactant-stabilised oil-water interface, where they form a quasi-2D active nematic film. Image taken from [136]. (b) Sketch of the experimental setup used in the experiments by Guillamat et al. [128]. The oil is replaced by 8CB, which forms, based on the temperature, either a nematic or a smectic phase and is anchored parallel to the interface. Image taken from [128].

the (substrate) friction coefficient stems from the viscosity of the bulk liquid the active nematic is in contact with.

In further research by the Sagués group [128] the active nematic is formed at the interface between the aqueous protein suspension and a volume of the hydrophobic oil octyl-cyanobiphenyl (8CB) (see Fig. 5.1(b)). 8CB forms, in the temperature range available in these experiments, either a nematic or a smectic phase. The interface between the aqueous and oil volume is stabilised with a polyethylene glycol (PEG)-based triblock copolymer surfactant. Additionally, the PEG promotes alignment of the 8CB molecules parallel to the interface.

When the 8CB is in the nematic phase, there is no directionality in the active nematic behaviour on the interface. Even when a magnetic field is applied to the 8CB nematic to fully align the nematic, there is no different behaviour detectable. When the temperature of the 8CB is lowered and the material transitions into the smectic phase, however, the active nematic rearranges and forms parallel stripes with uniform width perpendicular to the direction of the magnetic field (see Fig. 5.2). The bright stripes consist of densely packed microtubule bundles, while dark lanes consist of moving $\pm 1/2$-defects.

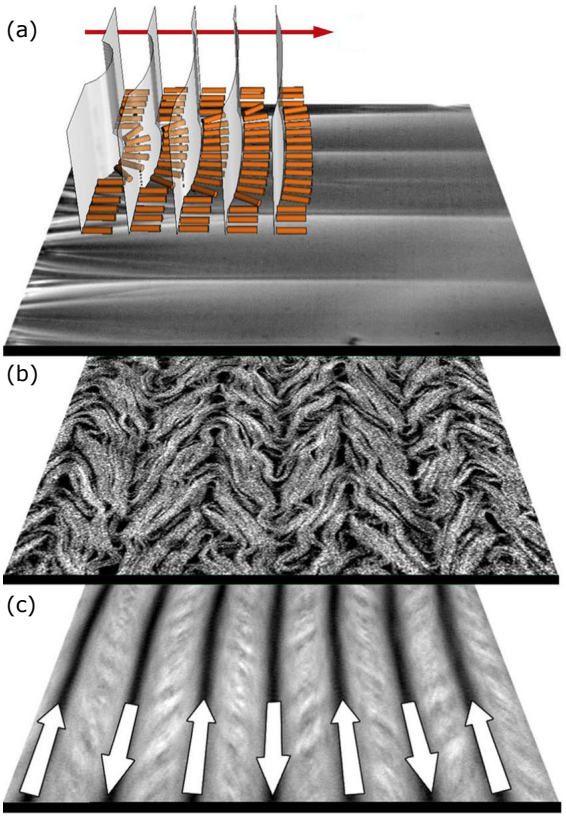

Figure 5.2: An active nematic layer in contact with a smectic-A phase. (a) Confocal reflection micrograph shows the structure of the smectic at the interface. The external magnetic field H has aligned the smectic. (b) Fluorescence confocal micrograph showing the dynamical patterning of the active nematic layer at the interface. (c) Time averaged fluorescence micrograph of the active nematic layer (total integration time 300s). Arrows show the direction of the flow. Image taken from [8].

The flat smectic planes form perpendicular to the applied magnetic field. The "bookshelf" geometry of the smectic-A phase results in a liquid that flows easily when sheared along the planes, but reacts as a solid when sheared in the orthogonal direction. The viscosity along the planes is therefore much smaller than the viscosity in orthogonal direction, and, in consequence, the effective substrate friction is much smaller in the direction along the planes than in orthogonal direction. The easy flow direction is therefore also in the direction perpendicular to the applied magnetic field. In the experiments the velocity scales linearly with the activity in the laminar flow regime, while in the active turbulence state $u \sim \sqrt{\zeta}$.

In order to reproduce these experiments we will perform simulations of a two-dimensional active liquid crystal with an anisotropic friction pattern. We show that

we get lanes with antiparallel flow, dependent on the friction ratio, and recover the scalings reported in the experimental work. We provide an explanation for how this matches with previous simulations on active nematics flowing on a substrate, and give directions for future work on the comparison of substrate friction and surface anchoring as a guiding mechanism for taming active turbulence.

5.2 Governing equations

The nematohydrodynamics approach set out in the introduction (Chapter 1) is used to study the effects of anisotropic friction on two-dimensional active nematics. As in previous work by Doostmohammadi et al. [121], substrate friction is introduced in the Navier-Stokes equation by including a term proportional to $-\underline{u}$

$$\rho\left(\frac{\partial u_i}{\partial t} + u_j\partial_j u_i\right) = -\partial_i p + \partial_j \Sigma_{ij} - f_i u_i, \tag{5.1}$$

where $\underline{f}$ is a friction coefficient that is made dependent on direction.

The active nematohydrodynamics equations (1.28), (5.1) and (1.23) are solved using the hybrid lattice Boltzmann described in Section 1.3. The time step and lattice spacing are set to unity. The parameters used are $A_0 = 1.5$, $\gamma = 2.73$, $L = 0.08$, $\Gamma_Q = 0.7$, $\xi = 0.7$, $\nu = 2/3$, $\rho = 1$, $p = 0.25$, in lattice Boltzmann units. We take the activity coefficient ζ positive, corresponding to an extensile, rod-like system. By choosing $\xi > 0.6$ we are considering a nematic liquid crystal in the flow-aligning regime.

5.3 Results

To demonstrate the formation of a laning active nematic state, with defects moving up and down lanes, simulations were performed on a 600x120 rectangular system. The friction in y-direction f_y is varied independently of the friction in x-direction f_x. When f_y is smaller than f_x, the fluid will preferably move in y-direction. The simulations are started from a randomly oriented initial state and initialised for 80,000 time steps to reach a statistically steady state. The larger dimension in x

is chosen to increase the number of lanes while keeping down the computational cost. Simulations on a 600x600 square lattice were also performed and yield the same behaviour.

An example of the response to different friction ratios can be viewed in Fig. 5.3. In all cases the active length scale $l_{\text{active}} = 1.41$. In Fig. 5.3(a) the system is in the active turbulence regime, with an equal friction ratio $f_x/f_y = 1$, and a hydrodynamic screening length $l_{\text{screen}} = 8.17$. The active energy is therefore dissipated mostly by the viscous dissipation, and instabilities are equally likely in both directions. When the friction ratio is increased to $f_x/f_y = 4$, corresponding to respective hydrodynamic screening lengths $l^x_{\text{screen}} = 1.83$ and $l^y_{\text{screen}} = 3.65$, the active nematic is still able to form irregular structures such as walls and isolated defects, and does so preferably in y-direction. For a large friction ratio $f_x/f_y = 67$, corresponding to respective hydrodynamic screening lengths $l^x_{\text{screen}} = 1.83$ and $l^y_{\text{screen}} = 14.9$, the active nematic forms lanes. The velocity is large in regions of large splay, with fluid moving up and down in neighbouring lanes (Fig. 5.3(c)).

The occurrence of active turbulence in Fig. 5.3(a) can be explained by noting that the active length scale l_{active} is significantly smaller than the hydrodynamic screening lengths in both perpendicular directions. We take care to stay away from the wet-dry crossover: at high friction, there is not enough energy for hydrodynamic wall formation and the active flux-induced instabilities of dry matter would dominate. Since we are modelling the experimental system reported by Guillamat et al. [128], which, without anisotropic friction, spontaneously creates and annihilates topological defects and is mostly uniform in concentration, we are convinced the system is "wet". The main instability is hydrodynamic in nature. In contrast, in "dry" systems the main instability is due to the formation of concentration bands that will break into filaments and coalesce. In our simulations we do not recover a vortex lattice as reported by Doostmohammadi et al. [121], which is characteristic of systems at the wet-dry crossover.

When the difference between the root-mean-squared velocities in the y-direction and in the x-direction is plotted against the friction ratio in Fig. 5.4, it can be

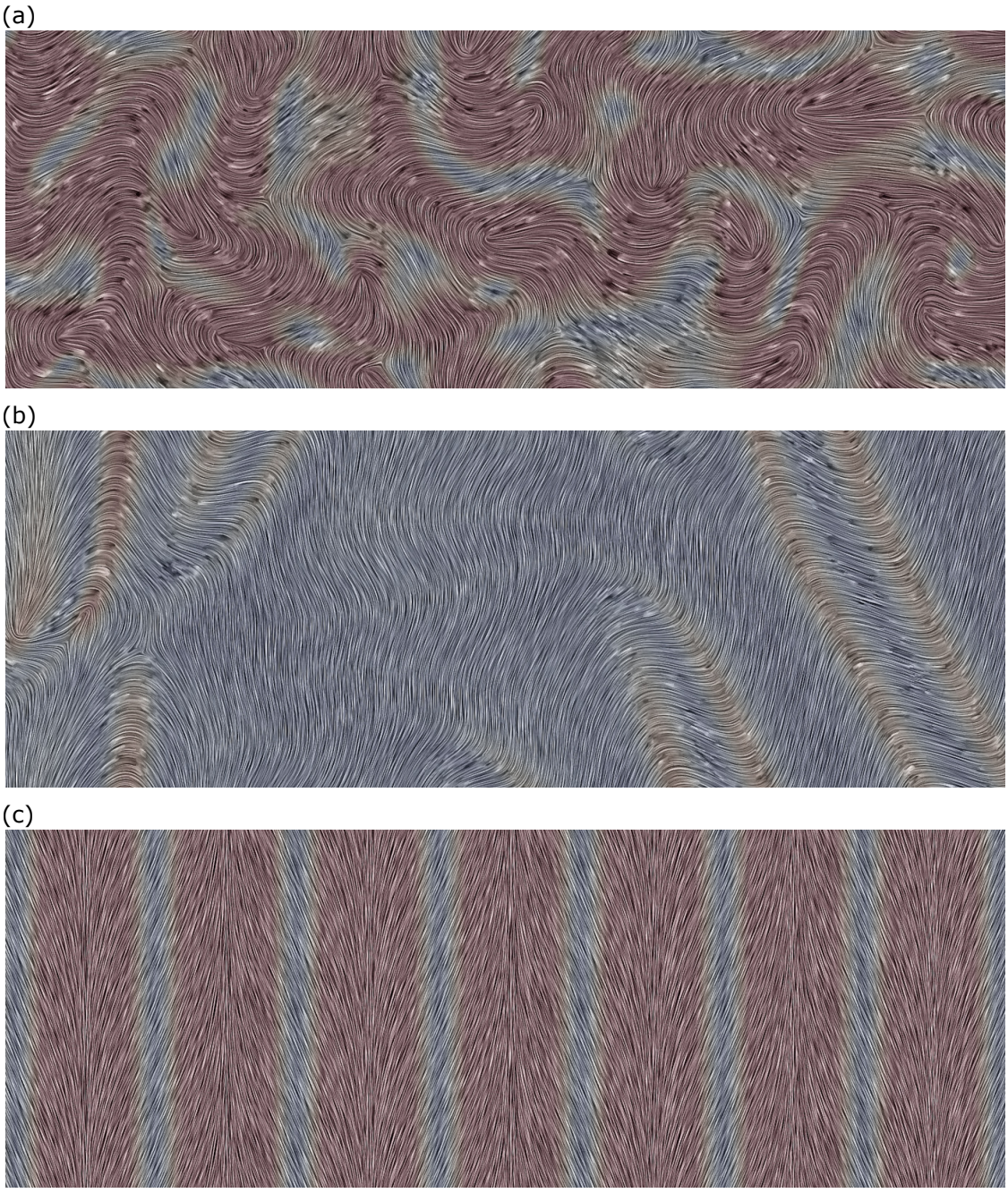

Figure 5.3: Increasing the friction ratio can lead to a transition from active turbulence to an aligned active nematic state, with defects moving up and down in the regions of large splay. The director field is coloured by the magnitude of the velocity, from blue for small velocity to red for large velocity. The active length scale is $l_{\text{active}} = 1.41$ in all cases. (a) For equal friction coefficients in x- and y-direction, with screening length $l_{\text{screen}} = 8.17$, the active nematic exhibits active turbulence. (b) For a friction ratio $f_x/f_y = 4$ and hydrodynamic screening lengths $l^x_{\text{screen}} = 1.83$ and $l^y_{\text{screen}} = 3.65$, the active nematic still forms irregular structures such as walls and isolated defects, but with a clear preference for flow in the y-direction. (c) For a large friction ratio $f_x/f_y = 67$ and hydrodynamic screening lengths $l^x_{\text{screen}} = 1.83$ and $l^y_{\text{screen}} = 14.9$, the active nematic forms a laning state.

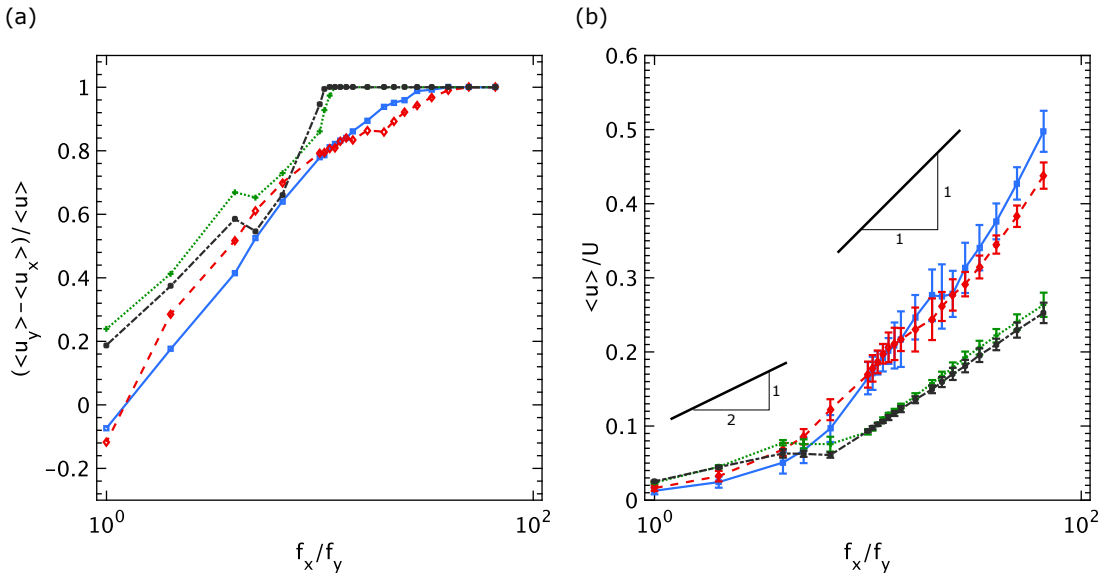

Figure 5.4: Increasing the friction ratio leads to the formation of an aligned active nematic state. The friction along the x-direction $f_x = 0.2$, while the friction in y-direction is varied. The activity $\zeta = 0.012$ (blue squares), 0.016 (red diamonds), 0.036 (green plusses), and 0.04 (black stars). The aligned active nematic state forms when $f_x/f_y \sim 15$, obvious from the fact that $\langle u_y \rangle$ becomes equal to the root-mean-squared velocity $\langle u \rangle$ in (a), while the gradient of the root-mean-squared velocity $\langle u \rangle$ also changes. The root-mean-squared velocity is scaled with $U = \zeta^{3/2}/f_x L^{1/2}$. Error bars indicate the standard deviation over ten different initialisations.

observed that both velocities are approximately equal for small friction ratios, but that the velocity in y-direction starts dominating when the friction ratio $f_x/f_y \sim 15$, for a range of activities. The snapshot in Fig. 5.3(c) is taken deep in this regime, where the aligned active filaments give rise to stripes intercalated by lanes with alternate antiparallel flow patterns. At the same friction ratio the scaling of the root-mean-squared velocity $\langle u \rangle$ changes from $\langle u \rangle \sim 1/\sqrt{f}$ to $\langle u \rangle \sim 1/f$ (see Fig. 5.4(b)), indicating that the flow has transitioned from a turbulent regime to a laminar flow regime, which is a characteristic of the laning state.

The laning state, in absence of temperature fluctuations, is stable in time. It is characterised by a time-independent director field, with alternate regions of large "up" and "down" splay, where the active stress $-\zeta \underline{\nabla} \cdot \underline{\underline{Q}}$ and, consequently, the velocity are large. In the regions in between there is a small amount of bend, but the velocity is almost zero. In the time-independent director field there is no formation of walls or topological defects, but the magnitude of the order goes

down in the highly splayed regions.

5.4 Discussion

Anisotropic friction is an effective way to control active turbulence and direct the flow in a well-defined fashion. Comparing our simulations with simulations with isotropic substrate friction, both show two scaling regimes with the friction coefficient f [121]. In a system with small isotropic friction the system is in the active turbulence regime (Fig. 5.5(a) shows a snapshot of the director field and (c) the velocity field coloured by the strength of the vorticity) and the velocity scales as $u \sim 1/\sqrt{f}$, while for large isotropic friction the vortices form an ordered array (see Fig. 5.5(b) for the regular director field and (d) for the vortex lattice) and the velocity scales as $u \sim 1/f$. We show in this work that the $u \sim 1/f$ scaling in a system with anisotropic friction occurs not for large friction, i.e. the "dry" limit, but instead for large friction ratios, and has to do with the fact that in this regime there is no formation of walls and topological defects.

All simulations so far have been performed for extensile rod-like active nematics. There is however no fundamental reason for different behaviour in disk-like or contractile systems. In future work we will perform simulations on contractile rod-like, extensile disk-like and contractile disk-like active nematics and compare the behaviour. Actomyosin gels [137] and mouse fibroblast cells [43] for instance can be modelled as contractile active nematics and may, due to their contractile behaviour, respond differently to attempts to direct flow.

We can compare the taming of active turbulence by introducing anisotropic friction with other methods to direct active nematics. Lavrentovich and co-workers have developed a system where living bacteria are transferred to a liquid crystalline medium, and interact non-trivially with the molecular ordering of the liquid crystal [138, 139]. This system is termed a "living liquid crystal". Single bacteria swim only along the director $\underline{n}$, due to minimisation of elastic distortions. Inactive bacteria also align their long axis with the director field. This elastic effect is aided by the fact that the coupling between the anisotropic viscosity of a liquid crystal and the

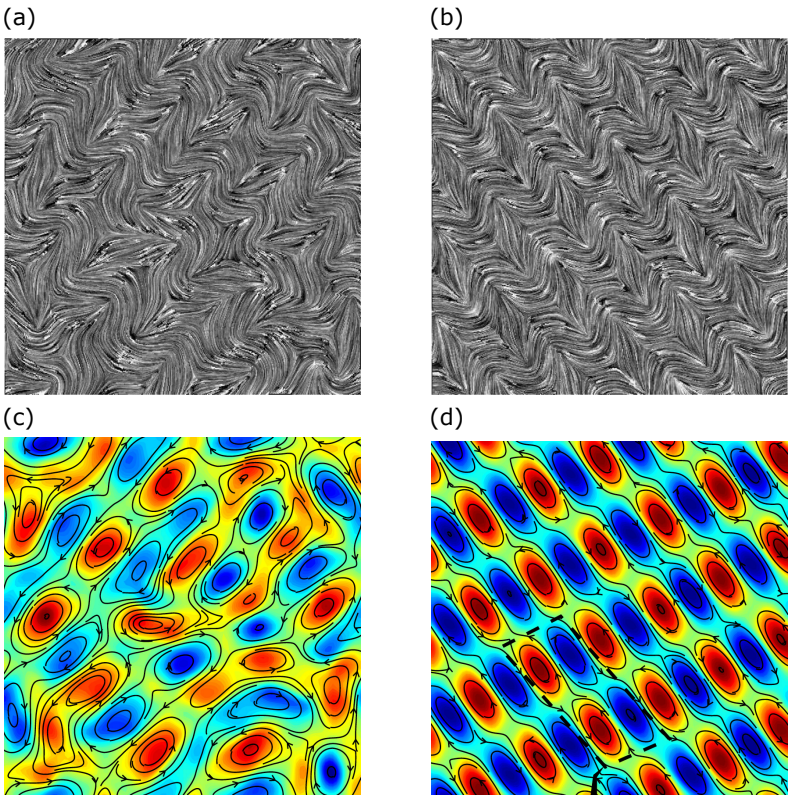

Figure 5.5: Emergence of a vortex lattice and defect ordering for extensile rod-like particles. (a)-(b) Director fields. The hydrodynamic screening length is $l_{\text{screen}} = 15.30$ ((a) and (c)) and 7.51 ((b) and (d)) (lattice units) respectively, and the active length scale $l_{\text{active}} = 1.12$. (c)-(d) Velocity field coloured by the magnitude of the vorticity. Image taken from [121].

dipolar flow field generated by a squirming micro-swimmer leads to a pusher (puller) swimming parallel (perpendicular) to the director field [140].

For comparison with the active nematic systems the collective behaviour of living liquid crystals at higher concentrations of bacteria has been considered. Here the long-range nematic alignment of the living liquid crystals is influenced by the collective flow created by the swimming bacteria. The swimming bacteria apply dipolar forces on the liquid crystal they are suspended in, meaning that the combined system can be modelled as an active nematic.

By patterning the surface of the flow cell the direction of the underlying liquid crystal can be fixed, for example imprinting $+1/2$-, $-1/2$-, and $+1$ spiral defect structures [122]. The bacteria in this background director field head towards defects of positive charge and swim away from defects with negative charge. In

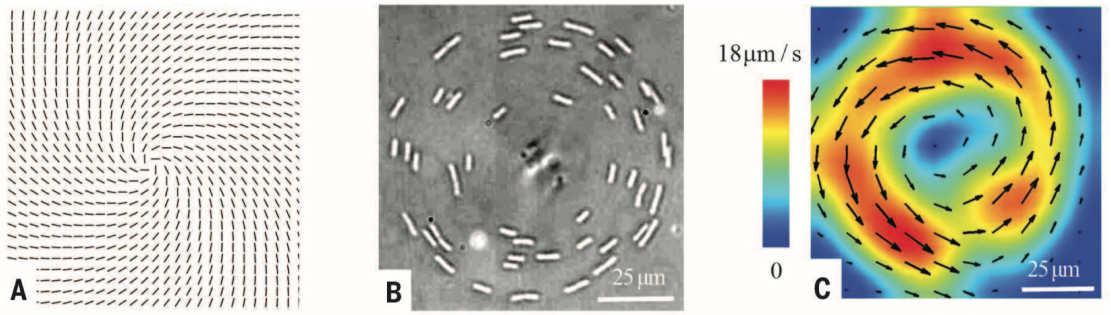

Figure 5.6: Unipolar circular flow of bacteria around a spiralling vortex. (a) Mixed splay-bend director deformation of the vortex. (b) Circular bacterial swarm enclosing the vortex centre. (c) Map of bacterial velocities. Image taken from [122].

a homogeneously aligned nematic liquid crystal the bacteria swim along $\underline{n}$ in a bipolar fashion, with equal numbers moving to the left and to the right. For pure bend and pure splay defects this holds true, bacterial swimming is bipolar and along local $\underline{n}$. For the spiral defect in Fig. 5.6(a) however this is no longer the case. The vortex is chiral and the local director makes a $\pi/4$ angle with the radial vector $\underline{r}$ everywhere. The bacteria swim in a finite width annulus (Fig. 5.6(b) and (c)), and move preferentially in the counterclockwise direction (for a clockwise spiralling defect). The swimming direction is along trajectories at a $\pi/4$ angle with respect to the local director. In unpublished work from our group it has been shown that these patterns are reproducible in simulations by imposing strong anchoring (equation (1.12)) on an active lyotropic liquid crystal.

In ongoing work we are comparing active nematics flowing over an anchoring pattern with active nematics flowing over an anisotropic friction pattern. We are simulating systems with the same surface patterning. We argue that both mechanisms are fundamentally different: in particular in the limits of strong anchoring or infinite friction both pick out a preferred direction, but in case of anchoring this means setting the local director, while friction sets the local flow axis, instantaneously dissipating all motion in the infinite friction direction. Early work indicates that they lead to different physics. This means that a suitable method has to be chosen for application in active materials.

6

Deformable active nematic shells

Up to this point we have only considered active liquid crystals in two-dimensional, flat geometries. In this chapter we introduce a framework for continuum simulations of active nematics on deformable membranes, with implications for physical triggers for morphogenesis processes. We show that we can recreate experiments and simulations of motile defects on spherical shells. Then, when we allow the shell to deform, long protrusions driven by motile topological defects are formed.

6.1 Introduction

Even when limited by the assumption of flat, two-dimensional geometries, the dynamical behaviour of active liquid crystals is extremely rich, with no counterpart in passive complex fluids. Depending on the activity and geometry, active liquid crystals have been observed to organise themselves into a variety of spatiotemporal patterns, such as oscillating textures [141], ordered arrangements of topological defects [142, 143], and "turbulence" even at low Reynolds number [14, 39, 40, 144].

When active materials are confined to curved surfaces, topological constraints strongly influence the resulting spatiotemporal patterns. In the literature there has been a substantial effort to account for the coupling between substrate geometry, orientational dynamics, and hydrodynamic flow, for instance for active turbulence

on tori [145] and arbitrary curved surfaces [146], for defect motion on spherical and ellipsoidal shells [147–149], and for defect dynamics on a surface with a prescribed evolution in time [150].

These works were inspired by the pioneering research by Keber et al. [15], who managed to confine microtubule-based active nematics onto a deformable spherical surface provided by a lipid vesicle. As in the equilibrium configuration of a liquid crystal on a sphere, following the Poincaré-Hopf theorem the total topological charge on the surface of the shell has to be +2. Without activity the minimum energy state is four +1/2 defects in a tetrahedral configuration [151]. In the case of active liquid crystals the +1/2 topological defects become motile and the spatial defect structure becomes dynamic. Keber et al. [15] showed that the spatiotemporal pattern is periodic for strictly spherical shells (see Fig. 6.1). This is, however, no longer true when stresses from the active nematic motion are coupled to vesicle deformations, creating a biomimetic shape-changing material. In the experiments the surface tension can be controlled to change the surface area. Slightly deflated vesicles continuously fluctuate around a mean spherical shape. Additionally, the vesicles exhibit four protrusions, tightly coupled to the motion of the four topological defects. Further deflation leads to anisotropic and mobile vesicles, with protrusions reaching tens of micrometers (see Fig. 6.2).

The available theoretical and simulation studies do not couple the defect-defect interaction to the dynamical evolution of the shell shape. Moreover there are indications that the coupling between defects and shape could be of relevance to morphogenesis. A very interesting model system is the multicellular polyp *Hydra*, a small fresh-water predatory animal [152]. Excised tissue fragments from the gastric region of mature *Hydra* regenerate into viable animals within a couple of days.

The most pronounced cytoskeletal features in mature *Hydra* are the actomyosin fibres near the basal side of the ectoderm layer, which are aligned with the main body axis (Fig. 6.3(b)). Excised tissue fragments preserve this actomyosin alignment, inherited from the parent *Hydra*, and they fold into closed, hollow spheroids (Fig. 6.3(a)). Subsequently, a regenerating spheroid exhibits substantial shape changes,

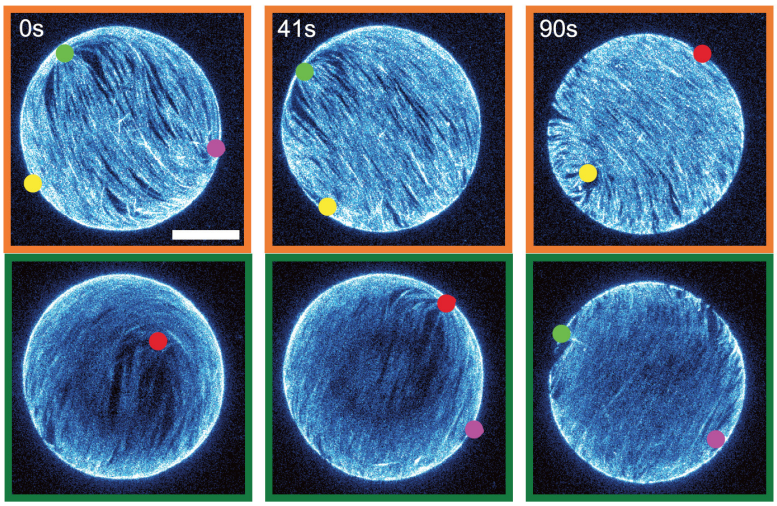

Figure 6.1: Time series of hemisphere projections over a single period of oscillation in which the four defects on a lipid vesicle coated with an active nematic switch from tetrahedral ($t = 0$s) through planar ($t = 41$s) and back to tetrahedral ($t = 90$s) configurations. The top row is the upper hemisphere projection, the bottom row the lower hemisphere projection. Scale bar, 20μm. Image taken from [15].

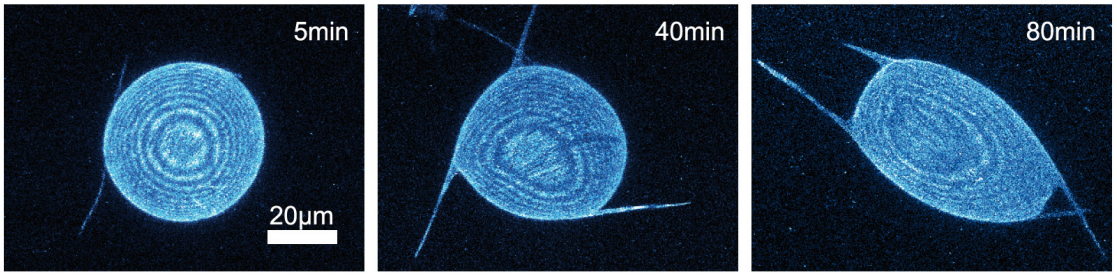

Figure 6.2: Confocal images showing the z-projection of the vesicle shape during deswelling. Starting from a spherical nematic vesicle with four +1/2 defects ($t = 5$ min), four dynamic protrusions grow from the defect sites while the vesicle slowly deswells. Image taken from [15].

yet the initial axis, determined by the orientation of the ectodermal actin fibres at the onset of regeneration, is preserved throughout the entire process. The final step in the regeneration process is what we are most interested in: the formation of the tentacles from the regenerating spheroid (Fig. 6.3(d)).

Recent in vitro work showed that tracking topological defects in tissues can provide insight into biological processes in the tissue. For example, defects in epithelial sheets were shown to induce cell death and extrusion [38], and defects in neural progenitor cell cultures were shown to cause variations in cell density and flow [42]. The correlations between topological defects and cell behaviour

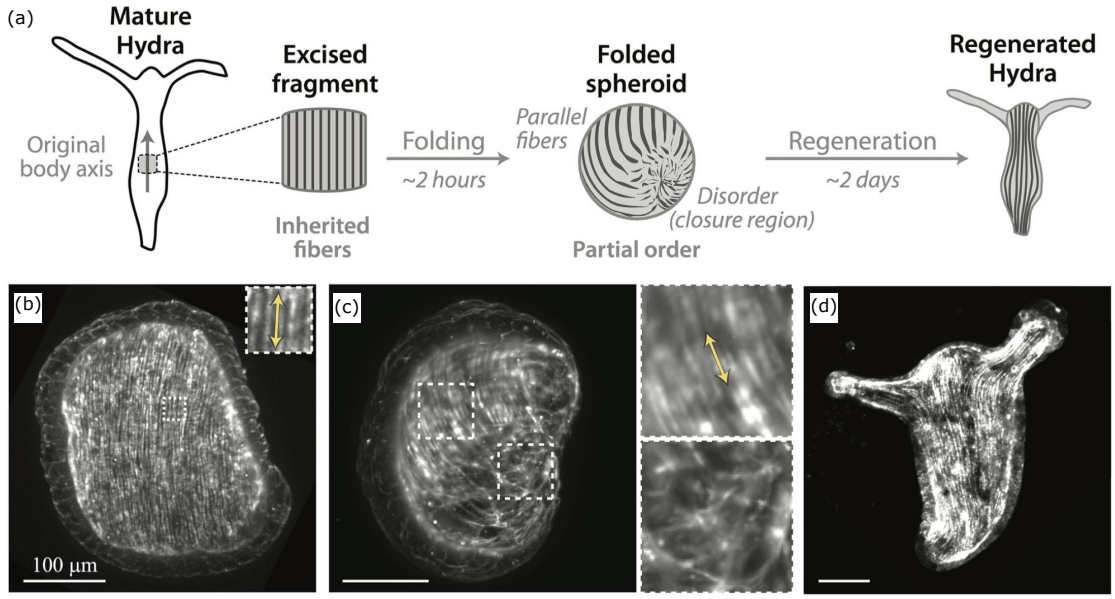

Figure 6.3: Actin organisation during *Hydra* regeneration from excised tissue fragments. (a) Schematic illustration of regeneration of an excised tissue fragment. The fragment folds into a spheroid, and then regenerates into a complete *Hydra*. The body axis is inherited from the parent organism. (b) Image of a fragment shows ectodermal actomyosin fibers aligned with the body axis. (c) A folded spheroid has an ordered array of actin fibers (top inset), but lack of order near the closure region (bottom inset). (d) A regenerated *Hydra*, with two tentacles coming out of the main body. Image adapted from [153].

arise from mechanical feedback from large compressive stresses at the defect sites, providing physical triggers for biological outcomes. Since the actin fibres tend to align, the spheroidal *Hydra* can be thought of as an active nematic vesicle, with a total +2 topological charge. The main morphological features in the *Hydra* are accompanied by topological defects, and therefore we want to use simulations of flexible active nematic shells to test whether strong local protrusions, like the *Hydra* tentacles, can be created with only mechanical cues.

In this Chapter we provide a methodology for simulating (active) nematic materials on deformable membranes. We describe the free energy functional that we will use in these simulations, and provide initial results. We reproduce periodic motion and active turbulence on strictly spherical shells, and show strong deformations driven by topological defects for half-spheres pinned on substrates and for free-floating membranes. Finally, we suggest directions for further research using the new algorithm.

6.2 Governing equations

In the previous chapters we introduced simulation frameworks for lyotropic liquid crystals (Chapters 2 and 3), as well as for active nematics (Chapters 4 and 5). To model deformable active nematic membranes we will combine the two. The most obvious approach might be to initialise a thin layer of nematic (the $\phi = 1$ phase) over the surface of a sphere, with isotropic fluid on the inside and the outside (the $\phi = 0$ phase), and impose activity. However, because the ϕ-field has diffuse interfaces, this will be a finite-thickness spheroid rather than a shell. To overcome this problem, we adapt the phase-field formulation so that the shell is thin compared to the typical radius of curvature. Additionally, we introduce a Helfrich free energy to account for the bending properties of the shell.

6.2.1 Membrane free energy

We start from the binary fluid model that we have previously used to model nematic tactoids (Chapter 2) and blue phase droplets (Chapter 3). Recall that we used a free energy term $f_{\text{mix}} = \frac{A_\phi}{2}\phi^2(1-\phi)^2$, with A_ϕ a positive constant, to set the two phase equilibria to $\phi = 0, 1$. The interface free energy was $f_{\text{interface}} = \frac{k_\phi}{2}\left(\underline{\nabla}\phi\right)^2$, providing a surface tension and ensuring the interface remains smooth. The Landau-de Gennes free energy for the nematic phase was then described by $f_{\text{bulk}} = A_0\left(\frac{1}{2}\left(1-\frac{\eta(\phi)}{3}\right)\text{tr}\underline{\underline{Q}}^2 - \frac{\eta(\phi)}{3}\text{tr}\underline{\underline{Q}}^3 + \frac{\eta(\phi)}{4}(\text{tr}\underline{\underline{Q}}^2)^2\right)$, where A_0 is a positive constant. This gives a first order, isotropic-nematic phase transition at $\eta = 2.7$. The term $\eta(\phi)$ is chosen to be linear in ϕ such that $\phi = 0$ corresponds to the isotropic phase and $\phi = 1$ to the nematic phase: $\eta_0 + \eta_s(\phi - \bar{\phi})$.

By changing the coupling term between the underlying phase field ϕ and the nematic order parameter $\underline{\underline{Q}}$, $\eta(\phi)$, a nematic can be formed at the interface between the two binary fluid phases (see Fig. 6.4). In order to simulate a nematic at the interface the expression for $\eta(\phi)$ is now chosen as

$$\eta(\phi) = \eta_0 - \eta_s(\phi - \bar{\phi})^2, \tag{6.1}$$

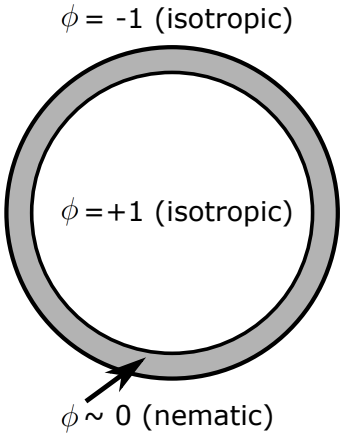

Figure 6.4: Two-dimensional schematic of a nematic membrane. The inside of the shell is at $\phi = 1$, the outside is at $\phi = -1$, which are both in the isotropic phase, and the interface between the two is nematic.

where we have, for convenience, moved the equilibria of the bulk phases to $\phi = \pm 1$. This allows parameters to be chosen such that both free energy minima in ϕ correspond to the isotropic phase, but the interface is itself nematic. For example, choosing $\eta_0 = 2.85$, $\eta_s = 0.3$, $\bar{\phi} = 0$, and allowing ϕ to vary between -1 and 1 will give $\eta(-1) = 2.55$ (isotropic), $\eta(0.5) = 2.85$ (nematic) and $\eta(1) = 2.55$ (isotropic). The interface is still diffuse, but compared to the old coupling the nematic membrane is now located at the interface, instead of between two interfaces. The parameters η_0 and η_s can be tuned to choose the range in ϕ over which the interface is nematic. The typical thickness of the nematic layer ~ 2 lattice sites.

The advantage of modelling an active nematic at the interface of two phases, while still using the full three-dimensional nematic tensor for the active nematic, is that the surface does not have to be tracked explicitly. Interesting work has modelled evolving surfaces by projecting the nematic tensor onto the surface [150], but the derivation and implementation of a surface hydrodynamic liquid crystal model is difficult. In this approach, we only have to change the coupling between the ϕ-field and the nematic tensor $\underline{\underline{Q}}$ to simulate stable active nematic shells.

To model the free energy of the membrane, we combine a mixing free energy, the interface free energy and a bending free energy

$$f_{\text{mem}} = \frac{\kappa^*}{2}\left(-\phi + \phi^3 - \epsilon^2 \nabla^2 \phi\right)^2 + \frac{k_\phi}{2}\left(\underline{\nabla}\phi\right)^2, \tag{6.2}$$

where κ^* is related to the bending rigidity as $\kappa^* = (4\epsilon^3/3\sqrt{2})\kappa$ and ϵ characterises the width of the interface. For a flat interface, the chemical potential $\mu = \delta f_{\text{mem}}/\delta\phi$ has to be zero, and the equilibrium profile is $\phi_{\text{eq}} = \frac{1}{2}(\tanh(x/\epsilon\sqrt{2}) + 1)$ for an interface located at $x = 0$. This interface is smooth and the interface width is characterised by the parameter ϵ. Note that the binary fluid mixing free energy is now included in the first term of this membrane free energy, and that it has phase equilibria at $\phi = -1, 1$.

For non-equilibrium profiles, the contribution to the chemical potential from the membrane free energy is

$$\begin{aligned}\mu^{\text{mem}} = \frac{\delta f_{\text{mem}}}{\delta\phi} &= \frac{\partial f_{\text{mem}}}{\partial\phi} - \partial_i\phi\frac{\partial f_{\text{mem}}}{\partial(\partial_i\phi)} + \nabla^2\left(\frac{\partial f_{\text{mem}}}{\partial\nabla^2\phi}\right) \\ &= \kappa^*\left((3\phi^2-1)\psi - \epsilon^2\nabla^2\psi\right) - k_\phi\nabla^2\phi,\end{aligned} \tag{6.3}$$

where $\psi = -\phi + \phi^3 - \epsilon^2\nabla^2\phi$. Note that derivatives of $\nabla^2\phi$ with respect to ϕ and $\nabla\phi$ are zero.

The membrane contribution to the stress can be derived from the free energy in equation (6.2)

$$\Sigma^{\text{mem}}_{ij} = (f_{\text{mem}} - \mu^{\text{mem}}\phi)\delta_{ij} - \partial_i\phi\frac{\partial f_{\text{mem}}}{\partial(\partial_j\phi)} + \partial_i\phi\partial_j\frac{\partial f_{\text{mem}}}{\partial\nabla^2\phi} - \partial_i\partial_j\phi\frac{\partial f_{\text{mem}}}{\partial\nabla^2\phi}. \tag{6.4}$$

It can be shown that the force density exerted by the membrane in the Navier-Stokes equation (1.29) $\underline{f}^{\text{mem}} = \underline{\nabla}\cdot\underline{\underline{\Sigma}}^{\text{mem}} = -\phi\underline{\nabla}\mu^{\text{mem}}$. Thermodynamically this follows from the Gibbs-Duhem equation $V\mathrm{d}P = \sum_i N_i\mathrm{d}\mu_i$, where N_i is the amount of matter of species i. Since $\phi \sim N/V$, the equation can be rewritten as $\mathrm{d}P = \phi\mathrm{d}\mu$.

6.3 Results

We solve the active nematohydrodynamics equations using the hybrid lattice Boltzmann method. The time step and lattice spacing are set to unity. We use the one-elastic-constant approximation for the nematic elasticity and set $L = 0.1$. To encourage the director to lie parallel to the interface, we set the anchoring strength $L_0 = 0.1$. The other parameters used are $A_0 = 1.5$, $\eta_0 = 2.9$, $\eta_s = 0.3$, $\bar{\phi} = 0$, $\Gamma_Q = 0.3$, $\Gamma_\phi = 0.1$, $k_\phi = 0.25$, $\kappa^* = 0.02$, $\epsilon = 1.2$, $\xi = 0.7$, $\nu = 2/3$, and $\rho = 1$, in lattice Boltzmann units.

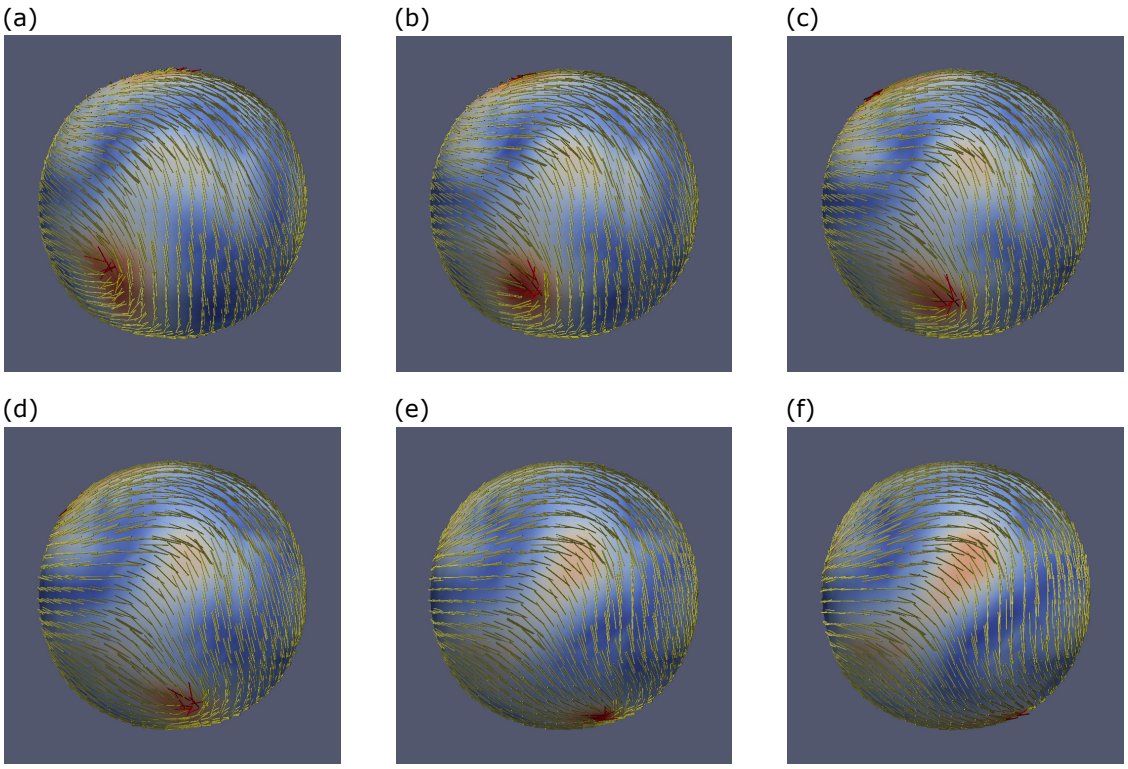

Figure 6.5: Motion of topological defects over the surface of a spherical shell with radius $r = 12$. Pictures are taken after 190, 200, 210, 220, 230, and 240 simulation time steps respectively. The activity number ($\zeta = 0.1$) is large enough to spontaneously create additional defect pairs (the growing instability is visible in the centre of panels (d) to (f)). Directors are coloured by the magnitude of the order (red meaning disordered, yellow strongly ordered), while the shell surface is coloured by the magnitude of the velocity (blue to red).

6.3.1 Static spherical shells

First, we simulate static spherical shells to validate our model. We initialise a $\phi = 1$ sphere of radius $r = 12$ in a $\phi = -1$ background on a 60 x 60 x 60 cubic lattice. We allow the interface to relax for 40 time steps, after which we set $\mathrm{d}\phi/\mathrm{d}t = 0$. As in the experiments by Keber et al. [15], and in previous simulations [148, 149], we recover periodic motion of four $+1/2$ defects for small activity. When the activity is increased additional defect pairs are spontaneously created and annihilated. In Fig. 6.5(d)-(f) the growing instability is visible in the centre of the picture. For increasing activity the dynamics become increasingly turbulent.

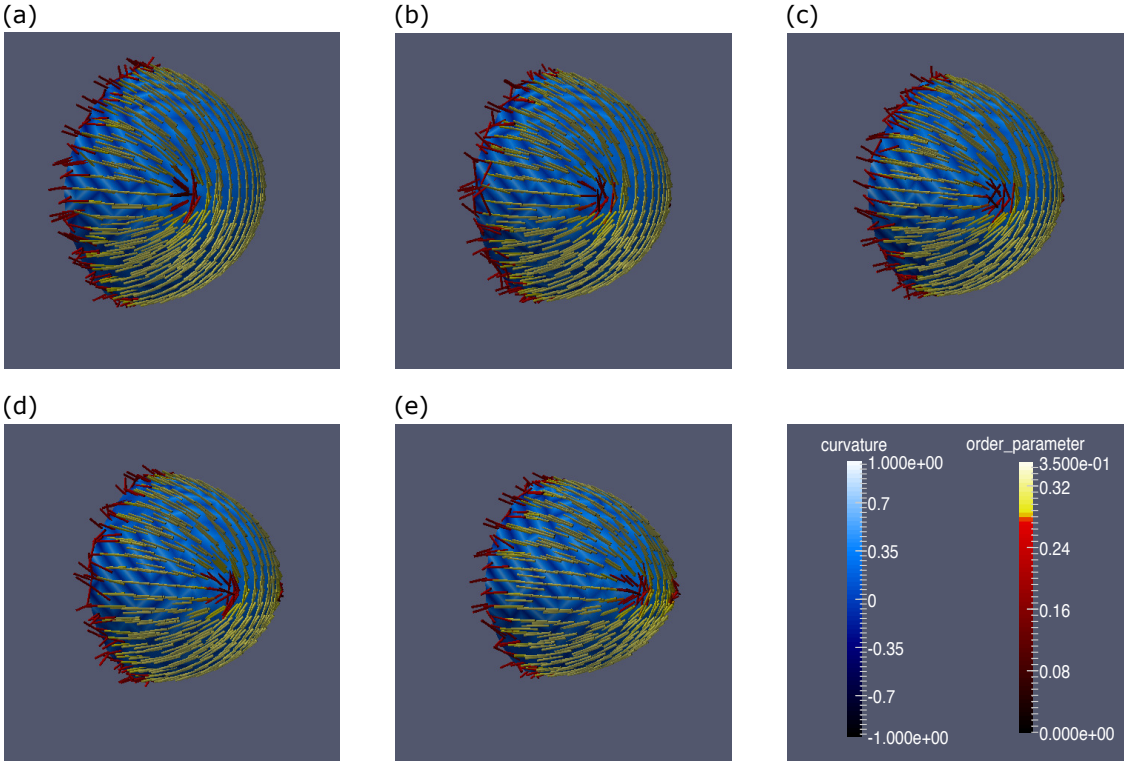

Figure 6.6: Deformation of an active nematic shell ($r = 12$) with activity number $\zeta = 0.002$ attached to a surface. The activity drives the two $+1/2$ defects gradually closer together, until the active force is balanced by the elastic force. The directors on the shell are coloured by the magnitude of the order (from red for disordered to yellow to white for fully aligned) and the surface is coloured by the magnitude of the curvature (dark blue for strongly negative to white for strongly positive).

6.3.2 Half-sphere fixed on a substrate

Next we simulate half-spheres fixed on a substrate. We initialise a $\phi = 1$ half-sphere of radius $r = 12$ in a $\phi = -1$ background on a 40 x 40 x 40 cubic lattice. The nematic is homeotropically anchored to the surface, such that the total topological charge of the nematic on the half-sphere has to be $+1$. The membrane is now allowed to deform continuously, but the interaction with the substrate constrains the deformation. Fig. 6.6 shows the deformation of the nematic half-sphere at small activity. The two $+1/2$ defects are driven together until the elastic repulsion keeps them at a fixed distance. The activity is not large enough to create additional defect pairs, so the configuration in Fig. 6.6(e) is the (unstable) steady state.

For intermediate activity the motile defects are driven together and merge into a single $+1$ defect (Fig. 6.7). This is allowed on a curved surface, indeed when the

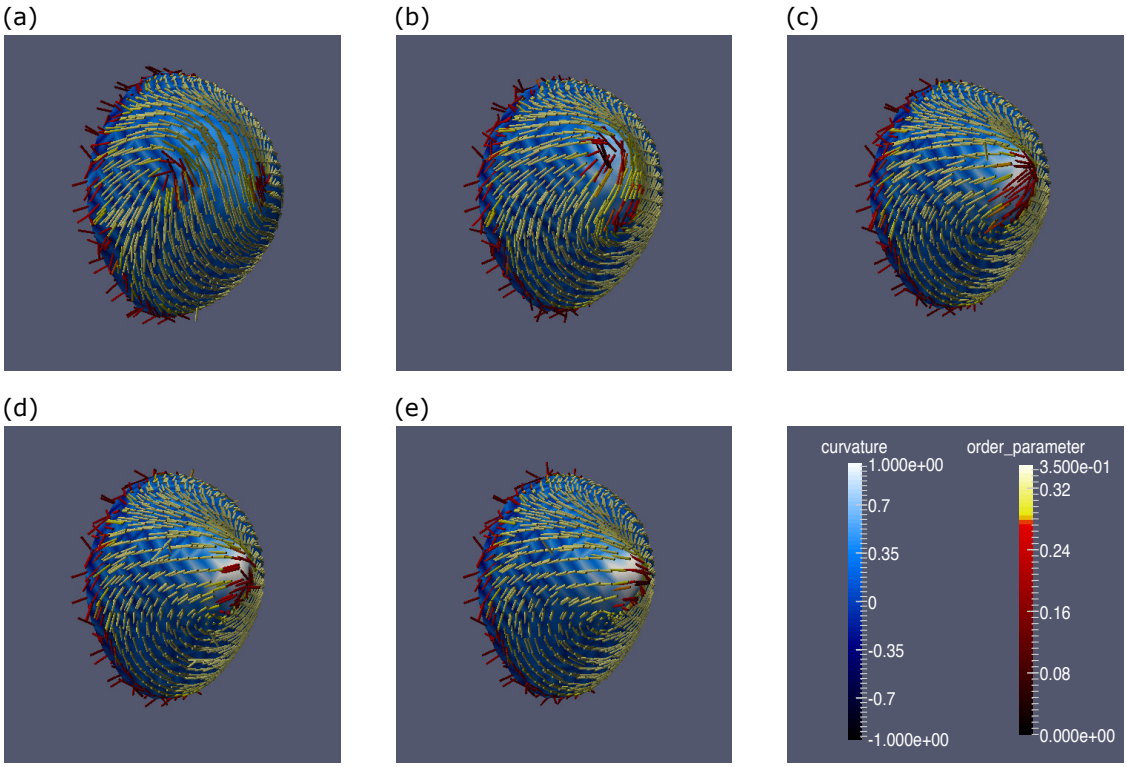

Figure 6.7: Deformation of an active nematic shell with activity number $\zeta = 0.05$ attached to a surface. Initially half-spherical with +1 total charge due to the perpendicular anchoring condition (a), the activity drives the two motile +1/2 defects together in panels (b) and (c), and leads to strong deformations (the protrusion growing in panels (d) and (e)). The directors on the shell are coloured by the magnitude of the order (from red for disordered to yellow to white for fully aligned) and the surface is coloured by the magnitude of the curvature (dark blue for strongly negative to white for strongly positive).

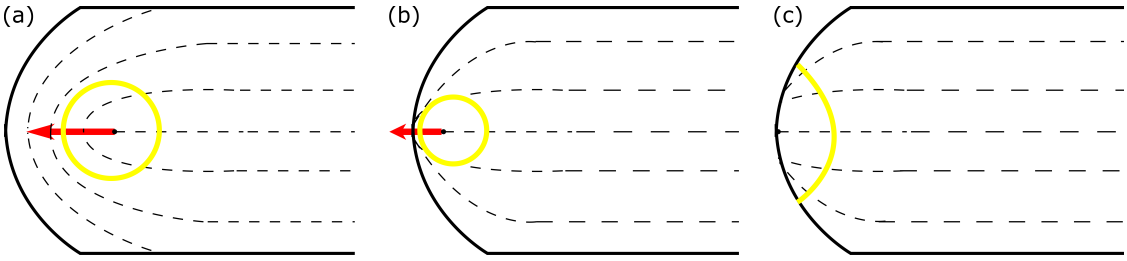

Figure 6.8: Schematic of a +1/2 topological defect approaching the tip of a protrusion (projection onto the plane). (a) The motile defect is moving over the surface of the protrusion, causing it to grow. (b) Closer to the tip the gradients will become smaller and the active stress will decrease. (c) When the defect has reached the tip of the protrusion, calculating the winding number along the yellow line gives a topological charge of +1. The gradients in the director field are small, and the active flow will therefore be small as well.

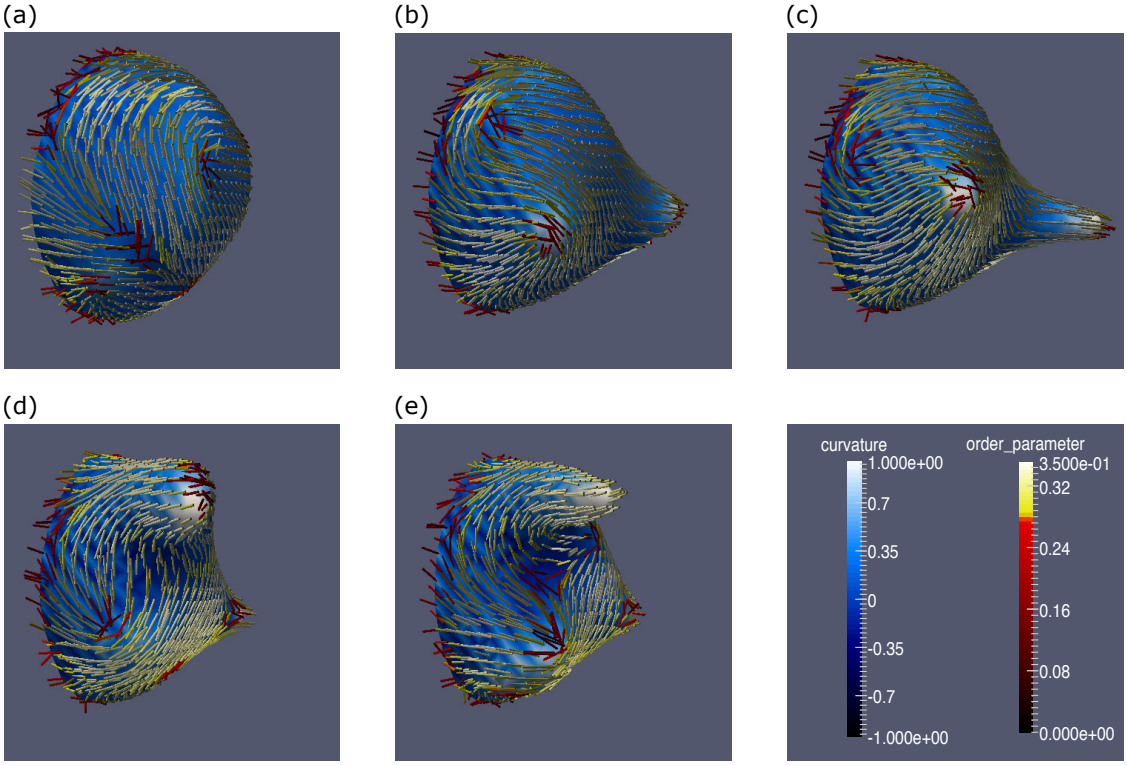

Figure 6.9: Deformation of an active nematic shell with activity number $\zeta = 0.12$ attached to a surface. The larger activity leads to a much more chaotic dynamics on the surface of the shell and a larger number of defects (a). Motile defects can drive formation of long "tentacles" (on the right in panels (b) and (c)), which will retract again due to surface tension. When a tentacle emerges from a $+1/2$ defect, to conserve charge it must leave behind a $-1/2$ defect (centre of snapshot in panels (d) and (e)). The directors on the shell are coloured by the magnitude of the order (from red for disordered to yellow to white for fully aligned) and the surface is coloured by the magnitude of the curvature (dark blue for strongly negative to white for strongly positive).

curvature is sufficiently large, the geometry itself will aid the stability of a $+1$ defect (see Fig. 6.8 for a schematic drawing). The stresses at the single $+1$ defect create a single protrusion, indicated by the region of large curvature in Fig. 6.7(c)-(e).

For large activity the dynamics on the surface of the shell is much more chaotic, and additional defect pairs form and annihilate. Remarkably, the motile $+1/2$ defects can drive formation of long "tentacles" (Fig. 6.9(b) and (c)). To conserve charge, when a $+1/2$ defect reaches the tip of a protrusion and becomes a $+1$ topological defect, it has to leave behind a $-1/2$ topological defect (centre of Fig. 6.9(d) and (e)). With the $+1$ defect on the tip of the protrusion, the active flow becomes negligible in the finger, since the gradient of $\underline{\underline{Q}}$ and, consequently, the

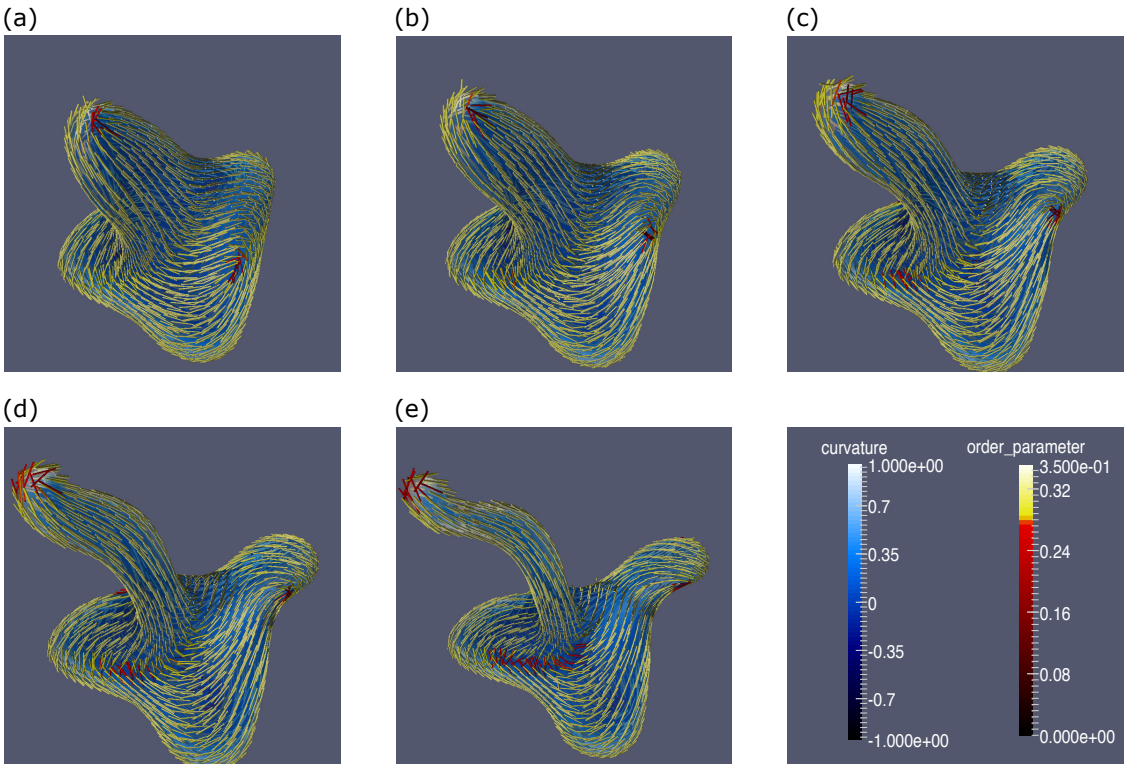

Figure 6.10: Deformation of a free-floating active nematic shell with activity number $\zeta = 0.1$. The growth of the protrusion on the top is driven by the $+1/2$ defect, and slows as soon as the defect has reached the tip. A second $+1/2$ defect on the right-hand side of the shell drives growth of a second protrusion. The directors on the shell are coloured by the magnitude of the order (from red for disordered to yellow to white for fully aligned, and the surface is coloured by the magnitude of the curvature (dark blue for strongly negative to white for strongly positive).

active force $\underline{f}^{\text{active}} = -\zeta\underline{\nabla} \cdot \underline{\underline{Q}}$ become zero on the surface of the protrusion. Surface tension will then lead to retraction of the protrusion.

6.3.3 Deformable free-floating shells

Finally we turn to free-floating shells. We use the same initialisation as for the static spherical shells, with a $\phi = 1$ sphere of radius $r = 12$ in a $\phi = -1$ background on a 60 x 60 x 60 cubic lattice, but now we allow the membrane to deform. For small activity the behaviour is unchanged from the static spherical shell, with four motile $+1/2$ topological defects but no deformation of the shell. When the activity is increased however, defects become more motile and can drive strong deformations of the shell. In Fig. 6.10 a long protrusion is driven upwards by a motile $+1/2$ defect. Again here, when the $+1/2$ defect reaches the tip of the protrusion, it becomes a

+1 defect and the active flow in the finger becomes negligible (Fig. 6.10(d) and (e)). Note also a second protrusion growing on the right.

6.4 Discussion

We have developed a new simulation method for studying active nematics on deformable membranes. Therefore we have been able to demonstrate that protrusions form in three dimensions on active nematic shells, driven by motile topological defects. Our setup is similar to the active nematics on lipid vesicle experiments by Keber et al. [15]. However, since our model uses diffuse interfaces, it is not possible to simulate protrusions thinner than ~ 2 lattice sites. Also, the ratio between the active stress, the bending energy and the surface tension in the experiments seems to be different, with the main body of the sphere staying much more spherical in the experiments. Further work will explore different parameter configurations.

The similarity with the formation of tentacles in *Hydra* is also striking. In our simulations there is no mechanism to stabilise the protrusion once the motile defect has reached the tip and the active flow has become small. At this point, surface tension will inevitably pull the protrusion back. In the living animal there seems to be some internal mechanism to balance this force, for instance, actin fibres may become cross-linked. An important point to mention is that it is currently unclear whether the active stresses generated by the actin fibres are, at the tissue level, contractile or extensile in nature. This is a topic which is still under debate.

Results presented so far are based on visual evidence. We are working on more quantitative measures of the correlation between motile topological defects and morphological processes, for instance relating the directionality of the stresses on the membrane with the topological defects, and showing the attraction of positively (negatively) charged topological defects to regions of positive (negative) curvature [147, 154, 155]. We are hoping to combine the results obtained so far with experimental work by Kinneret Keren's group at Technion in Tel Aviv.

A natural extension of this work would be to couple the strength of the activity to the curvature of the membrane. This could potentially help stabilise the protrusions:

in the current simulations, the flow generated by motile defects is quite strong and will drive the defect to the tip of the protrusion. At that point, the gradients in the director field will become very small and the surface tension will be strong enough to drag the protrusion back. If the activity is reduced for flat planes, or singly curved surfaces (the protrusion can be thought of as a cylinder), this may help stabilise the protrusions. At the moment we do not know about a mechanism in the live animal that would generate this type of coupling however.

Another possible interaction in physical systems would be a coupling of active stresses to a chemical regulator. The activity parameter could be written as $\zeta_\mathrm{a} = \zeta f(c)$, where $f(c)$ is a function of a concentration field c. The concentration field would change over time due to advection, diffusion, and reactions. It has been shown that activity regulated by a concentration field can play a role in the self-organisation of morphogenetic processes [156–158], but these papers only consider flow of the chemical regulator over the surface of the membrane. In our model the chemical regulator could flow through the three-dimensional space, mimicking experimental conditions more closely.

7 Discussion

Section 7.1 summarises the main conclusions of the investigations into dynamics and topology of active and passive liquid crystals considered in this thesis. Finally, Section 7.2 provides an outlook for the research that we are currently working on.

7.1 Summary of conclusions

In Chapter 2 we investigated the strong elongation of chitin tactoids under an electric field. Previous studies have reported increases in aspect ratio of $\sim 10\%$, but in experiments performed by Patrick Davidson's group at Paris-Sud we observed an increase in aspect ratio from ~ 2 to ~ 20, accompanied by a transition from a spindle-like shape to a cigar-like shape. Simulations show that this is due to strong anchoring of the individual particles to the interface. To align the particles close to the interface with the applied electric field, the interface has to be distorted, leading to a minimum free energy configuration corresponding to a tactoid shape with long flat sides and rounded tips, i.e., a cigar-like shape. This process is completely reversible, and the time-scales indicate that hydrodynamics should play a role, which we confirm in our simulations.

In Chapter 3 we characterise the behaviour of cholesterics and two-dimensional blue phases when confined to a two-dimensional droplet. Since the shape of

the tactoid is strongly determined by the director anchoring at the interface, we show that the more complicated internal structure of cholesterics and two-dimensional blue phases when compared to nematics makes it possible to access a wealth of morphologies. Furthermore, we show that application of an external field perpendicular to the droplet can lead to tactoids strongly resembling chiral rafts, with a uniform director in the centre and twist around the edges. In the future it would be interesting to perform hydrodynamic simulations investigating how the chiral rafts interact.

By introducing activity in two-dimensional blue phases, in Chapter 4 we show how the director structure of the blue phase affects active dynamics. The two-dimensional blue phase consists of double-twist cylinders on a hexagonal lattice, separated by $-1/2$ topological defects. Since the active force in the Navier-Stokes equations (1.29) is proportional to $\underline{\nabla} \cdot \underline{\underline{Q}}$, the ground state director field of the blue phase will set up flows in the system. We show that the internal structure of the two-dimensional blue phase is able to screen contractile forces, and we do not observe active turbulence in our simulations. For extensile activity however, there is an active instability threshold, after which the double-twist cylinders dissociate and an active turbulent state is formed.

Substrate friction is another method to avoid active turbulence in active nematics and to control the direction of the flow. In Chapter 5 we introduce anisotropic friction, meaning that the viscous damping $-\underline{f} \cdot \underline{u}$ in the Navier-Stokes equations (1.29) is different in different directions. We show that a laning state can be obtained when the friction ratio ~ 15. The laning state is stable in time and comprises alternate stripes of large "up" and "down" splay, in which the velocity is large, alternating up and down in direction. This state has not previously been obtained in simulations, but has been observed in experiments on microtubule-kinesin active nematics on an aligned smectic-water interface.

In Chapter 6 we describe a new simulation method for modelling deformable active nematic membranes in three dimensions. This gives us the opportunity to study the interaction between motile topological defects, which produce large stresses

on the membrane, and the membrane deformation, with implications for physical triggers for morphogenetic processes. We recreate simulations and experiments for periodic motion of motile defects on a strictly spherical shell. Then, when we allow for deformation, long protrusions driven by motile defects are formed, without any chemical or genetic cue.

7.2 Outlook

Two of the topics presented in this thesis are still work in progress: the first is extending our investigation of anisotropic friction. All simulations so far have been performed for extensile, rod-like active nematics. We think there is no fundamental reason why the transition to a laning state should only occur for these systems, so we plan to simulate extensile, disk-like active nematics, and contractile active nematics. This may give rise to unexpected behaviour with implications for the control mechanism adopted in different experimental configurations.

We are also comparing active nematics flowing over an anchoring pattern with active nematics flowing over a similar anisotropic friction pattern. A simple argument shows that these are different: in the limit of infinite anchoring the local director is fixed, while infinite friction in one direction sets the flow axis. We will use simulations to compare the effect of the different perturbations with the aim of suggesting future experiments.

Secondly, we are continuing to develop the simulations of deformable active nematic membranes. We have been able to show that the deformation of the shells is driven by motile topological defects, so far relying on visual evidence. We are working on more quantitative measures, to relate the active stresses on the membrane to the defect charge, and to show the attraction of positively (negatively) charged topological defects to regions of positive (negative) curvature.

A natural extension to this work would be to couple the strength of the activity to the curvature of the surface. This could potentially help stabilise the protrusions: currently, as soon as the motile defect reaches the tip of the protrusion the surface tension starts dragging the protrusion back. The active stresses could also be coupled

to a chemical regulator, modelled by a concentration field in three dimensions. It has already been shown that activity regulated by a concentration field can influence morphogenetic processes, even when the chemical is confined to a two-dimensional surface. In our simulations the chemical regulator could flow through the three-dimensional space, which mimics experimental conditions more closely.

Other topics that it would be interesting to address in the future are active chiral nematic droplets, interactions between active nematic membranes and obstacles, and passive colloids at an active nematic interface. The first would be an extension of our work on tactoids and active blue phases. We have done preliminary simulations of chiral nematic droplets, obtaining shapes like those reported by Nyström et al. [159]. By adding activity these droplets could deform and potentially self-propel in a non-trivial fashion. A paper by Tjhung et al. [127] showed that unstructured droplets of chiral active fluid show a range of complex motilities, such as oscillatory swimming, helical swimming, and run-and-tumble motion. In our model the chirality would be introduced through the internal structure in the droplet, instead of through the stress.

Secondly, one can envisage experiments where the microtubule-kinesin active nematics are brought to an oil-water interface, but with pillars extending through the interface. The oil-water interface will form a meniscus where it touches the pillar. Then, the active flows could potentially lead to interesting physics. For example, it is well known that when a rotating rod penetrates the interface between two Newtonian fluids, the meniscus can climb the rod [160]. Here the pillar would not be rotating: however, the active nematic in the membrane would flow continuously, and the interaction with the pillar may lead to a similar effect. For these simulations the model for active nematic shells can be modified to simulate an infinite active layer floating between two fluids, with a pillar in the centre as a boundary condition.

Thirdly, recent unpublished work from our group explored the behaviour of passive colloids in a channel with active flow [161]. Using our simulation method for active membranes, we could bring colloids to the active interface between two fluids and characterise the influence on the active dynamics. The effect should be

relatively pronounced, because any colloid leads to extra topological defects in the nematic layer.

References

[1] O. Lehmann, *Flüssige Kristalle* (Engelmann (Leipzig), 1904).

[2] G. Friedel, Ann. Phys. (Paris) **9**, 273 (1922).

[3] T. Ishikawa and O. D. Lavrentovich, Phys. Rev. E **60**, R5037 (1999).

[4] F. Frank, Philos. Trans. R. Soc. A **309**, 71 (1983).

[5] A. Duzgun, J. V. Selinger, and A. Saxena, Phys. Rev. E **97**, 062706 (2018).

[6] P. E. Cladis, P. Pieranski, and M. Joanicot, Phys. Rev. Lett. **52**, 542 (1984).

[7] G. P. Alexander, B. G.-g. Chen, E. A. Matsumoto, and R. D. Kamien, Rev. Mod. Phys. **84**, 497 (2012).

[8] A. Doostmohammadi, J. Ignés-Mullol, J. M. Yeomans, and F. Sagués, Nat. Commun. **9**, 3246 (2018).

[9] D. C. Wright and N. D. Mermin, Rev. Mod. Phys. **61**, 385 (1989).

[10] L. Landau, in *Collected Papers*, edited by D. Ter Haar (Pergamon, 1965), p. 193.

[11] A. Matsuyama, R. M. L. Evans, and M. E. Cates, Eur. Phys. J. E **9**, 1 (2002).

[12] M. Nobili and G. Durand, Phys. Rev. A **46**, R6174 (1992).

[13] J.-B. Fournier and P. Galatola, EPL **72**, 403 (2005).

[14] T. Sanchez, D. T. N. Chen, S. J. DeCamp, M. Heymann, and Z. Dogic, Nature **491**, 431 (2012).

[15] F. C. Keber, E. Loiseau, T. Sanchez, S. J. DeCamp, L. Giomi, M. J. Bowick, M. C. Marchetti, Z. Dogic, and A. R. Bausch, Science **345**, 1135 (2014).

[16] I. I. Smalyukh, S. Chernyshuk, B. I. Lev, A. B. Nych, U. Ognysta, V. G. Nazarenko, and O. D. Lavrentovich, Phys. Rev. Lett. **93**, 117801 (2004).

[17] D. Volfson, S. Cookson, J. Hasty, and L. S. Tsimring, Proc. Natl. Acad. Sci. U.S.A. **105**, 15346 (2008).

[18] L. Tran, M. O. Lavrentovich, G. Durey, A. Darmon, M. F. Haase, N. Li, D. Lee, K. J. Stebe, R. D. Kamien, and T. Lopez-Leon, Phys. Rev. X **7**, 041029 (2017).

[19] N. Sulaiman, D. Marenduzzo, and J. Yeomans, Phys. Rev. E **74**, 041708 (2006).

[20] P. G. de Gennes and J. Prost, *The Physics of Liquid Crystals* (Oxford University Press, 1995).

[21] P. Cladis and M. Kleman, J. Phys. (Paris) **33**, 591 (1972).

[22] J. Fukuda and S. Žumer, Nat. Commun. **2**, 246 (2011).

[23] T. Skyrme, Nucl. Phys. **31**, 556 (1962).

[24] J. L. Ericksen, Arch. Ration. Mech. Anal. **4**, 231 (1960).

[25] J. Ericksen, Phys. Fluids **9**, 1205 (1966).

[26] F. Leslie, Quart. J. Mech. Appl. Math. **19**, 357 (1966).

[27] F. Leslie, Arch. Ration. Mech. Anal. **28**, 265 (1968).

[28] O. Parodi, J. Phys. (Paris) **31**, 581 (1970).

[29] B. J. Edwards, A. N. Beris, and M. Grmela, J. Non-Newtonian Fluid Mech. **35**, 51 (1990).

[30] B. J. Edwards, A. N. Beris, M. Grmela, and R. G. Larson, J. Non-Newtonian Fluid Mech. **36**, 243 (1990).

[31] A. N. Beris and B. J. Edwards, *Thermodynamics of Flowing Systems* (Oxford University Press, 1994).

[32] J. W. Cahn and J. E. Hilliard, J. Chem. Phys. **28**, 258 (1958).

[33] L. D. Landau and E. M. Lifshitz, *Course of Theoretical Physics Vol 7: Theory and Elasticity* (Pergamon Press, 1959).

[34] D. L. Koch and G. Subramanian, Annu. Rev. Fluid Mech. **43**, 637 (2011).

[35] C. Dombrowski, L. Cisneros, S. Chatkaew, R. E. Goldstein, and J. O. Kessler, Phys. Rev. Lett **93**, 098103 (2004).

[36] Y. Sumino, K. H. Nagai, Y. Shitaka, D. Tanaka, K. Yoshikawa, H. Chaté, and K. Oiwa, Nature **483**, 448 (2012).

[37] V. Narayan, S. Ramaswamy, and N. Menon, Science **317**, 105 (2007).

[38] T. B. Saw, A. Doostmohammadi, V. Nier, L. Kocgozlu, S. Thampi, Y. Toyama, P. Marcq, C. T. Lim, J. M. Yeomans, and B. Ladoux, Nature **544**, 212 (2017).

[39] H. H. Wensink, J. Dunkel, S. Heidenreich, K. Drescher, R. E. Goldstein, H. Löwen, and J. M. Yeomans, Proc. Natl. Acad. Sci. U.S.A. **109**, 14308 (2012).

[40] J. Dunkel, S. Heidenreich, K. Drescher, H. H. Wensink, M. Bär, and R. E. Goldstein, Phys. Rev. Lett. **110**, 228102 (2013).

[41] A. Doostmohammadi, S. P. Thampi, and J. M. Yeomans, Phys. Rev. Lett. **117**, 048102 (2016).

[42] K. Kawaguchi, R. Kageyama, and M. Sano, Nature **545**, 327 (2017).

[43] G. Duclos, C. Erlenkämper, J.-F. Joanny, and P. Silberzan, Nat. Phys. **13**, 58 (2017).

[44] R. A. Simha and S. Ramaswamy, Phys. Rev. Lett. **89**, 058101 (2002).

[45] S. P. Thampi and J. M. Yeomans, Eur. Phys. J. **225**, 651 (2016).

[46] C. Denniston, Phys. Rev. B **54**, 6272 (1996).

[47] L. Giomi, M. J. Bowick, P. Mishra, R. Sknepnek, and M. C. Marchetti, Philos. Trans. R. Soc. A **372**, 20130365 (2014).

[48] S. P. Thampi, R. Golestanian, and J. M. Yeomans, Philos. Trans. R. Soc. A **372**, 1745 (2014).

[49] S. Shankar, S. Ramaswamy, M. C. Marchetti, and M. J. Bowick, Phys. Rev. Lett. **121**, 108002 (2018).

[50] V. Bratanov, F. Jenko, and E. Frey, Proc. Natl. Acad. Sci. U.S.A. **112**, 15048 (2015).

[51] L. Giomi, Phys. Rev. X **5**, 031003 (2015).

[52] D. Marenduzzo, E. Orlandini, M. E. Cates, and J. M. Yeomans, Phys. Rev. E **76**, 031921 (2007).

[53] C. Denniston, D. Marenduzzo, E. Orlandini, and J. M. Yeomans, Philos. Trans. R. Soc. A **362**, 1745 (2004).

[54] C. Denniston, E. Orlandini, and J. M. Yeomans, Phys. Rev. E **63**, 056702 (2001).

[55] L. Metselaar, I. Dozov, K. Antonova, E. Belamie, P. Davidson, J. M. Yeomans, and A. Doostmohammadi, Phys. Rev. E **96**, 022706 (2017).

[56] L. Onsager, Ann. NY Acad. Sci. **51**, 627 (1949).

[57] H. Zocher, Z. Anorg. Allg. Chem. **147**, 91 (1925).

[58] A. V. Kaznacheev, M. M. Bogdanov, and S. A. Taraskin, J. Exp. Theor. Phys. **95**, 57 (2002).

[59] P. Prinsen and P. van der Schoot, Phys. Rev. E **68**, 021701 (2003).

[60] M. P. Lettinga, K. Kang, A. Imhof, D. Derks, and J. K. G. Dhont, J. Phys. Condens. Matter **17**, S3609 (2005).

[61] M. P. Lettinga, K. Kang, P. Holmqvist, A. Imhof, D. Derks, and J. K. G. Dhont, Phys. Rev. E **73**, 011412 (2006).

[62] R. M. W. van Bijnen, R. H. J. Otten, and P. van der Schoot, Phys. Rev. E **86**, 051703 (2012).

[63] R. H. J. Otten and P. van der Schoot, J. Chem. Phys. **137**, 154901 (2012).

[64] J. Everts, M. Punter, S. Samin, P. van der Schoot, and R. van Roij, J. Chem. Phys. **144**, 194901 (2016).

[65] A. S. Sonin, J. Mater. Chem. **8**, 2557 (1998).

[66] N. Puech, E. Grelet, P. Poulin, C. Blanc, and P. van der Schoot, Phys. Rev. E **82**, 020702 (2010).

[67] V. Jamali, N. Behabtu, B. Senyuk, J. A. Lee, I. I. Smalyukh, P. van der Schoot, and M. Pasquali, Phys. Rev. E **91**, 042507 (2015).

[68] Z. Dogic, Phys. Rev. Lett. **91**, 165701 (2003).

[69] A. Modlińska, A. M. Alsayed, and T. Gibaud, Sci. Rep. **5**, 18 (2015).

[70] P. W. Oakes, J. Viamontes, and J. X. Tang, Phys. Rev. E **75**, 061902 (2007).

[71] Y.-K. Kim, S. V. Shiyanovskii, and O. D. Lavrentovich, J. Phys. Condens. Matter **25**, 404202 (2013).

[72] J.-F. Revol, L. Godbout, X.-M. Dong, D. G. Gray, H. Chanzy, and G. Maret, Liq. Cryst. **16**, 1 (1994).

[73] J. H. Park, J. Noh, C. Schutz, G. Salazar-Alvarez, G. Scalia, L. Bergstrom, and J. P. F. Lagerwall, Chem. Phys. Chem. **15**, 1477 (2014).

[74] P.-X. Wang, W. Y. Hamad, and M. J. MacLachlan, Nat. Commun. **7**, 11515 (2016).

[75] G. E. Volovik and O. D. Lavrentovich, Zh. Eksp. Teor. Fiz. **85**, 6 (1983).

[76] A. A. Verhoeff, R. H. J. Otten, P. van der Schoot, and H. N. W. Lekkerkerker, J. Chem. Phys. **134**, 044904 (2011).

[77] J. Bernal and I. Fankuchen, J. Gen. Physiol. **25**, 1 (1941).

[78] A. Kaznacheev, M. Bogdanov, and A. Sonin, J. Exp. Theor. Phys. **97**, 1159 (2003).

[79] C. T. O'Konski and H. C. Thacher Jr, J. Phys. Chem. **57**, 9 (1953).

[80] C. T. O'Konski and F. E. Harris, J. Phys. Chem. **61**, 9 (1957).

[81] J. Melcher and G. Taylor, Annu. Rev. Fluid Mech. **1**, 1 (1969).

[82] O. Vizika and D. A. Saville, J. Fluid Mech. **239**, 1 (1992).

[83] D. A. Saville, Phys. Rev. Lett. **71**, 2907 (1993).

[84] C. S. Park, N. A. Clark, and R. D. Noble, Phys. Rev. Lett. **72**, 1838 (1994).

[85] B. Lev, V. Nazarenko, A. Nych, and P. Tomchuk, JETP Lett. **71**, 6 (2000).

[86] B. Lev, V. Nazarenko, A. Nych, D. Schur, P. Tomchuk, J. Yamamoto, and H. Yokoyama, Phys. Rev. E **64**, 021706 (2001).

[87] G. K. Auernhammer, J. Zhao, B. Ullrich, and D. Vollmer, Eur. Phys. J. E **30**, 4 (2009).

[88] K. W. Wagner, Archiv für Elektrotechnik **2**, 371 (1914).

[89] E. Paineau, I. Dozov, I. Bihannic, C. Baravian, M.-E. M. Krapf, A.-M. Philippe, S. Rouzière, L. J. Michot, and P. Davidson, ACS Appl. Mater. Interfaces **4**, 8 (2012).

[90] L. Metselaar, A. Doostmohammadi, and J. M. Yeomans, Mol. Phys. **116**, 2856 (2018).

[91] M. Ravnik and S. Žumer, Molec. Crys. Liq. Crys. **594**, 2 (2014).

[92] M. Ravnik, M. Stimulak, M. Cancula, and S. Žumer, Molec. Crys. Liq. Crys. **619**, 61 (2015).

[93] I. Muševič, Materials **11**, 24 (2017).

[94] H.-B. Braun, Adv. Phys. **61**, 1 (2012).

[95] X.-Q. Xu and J. H. Han, Phys. Rev. Lett. **108**, 185301 (2012).

[96] I. Dzyaloshinsky, J. Phys. Chem. Solids **4**, 241 (1958).

[97] A. Nych, J. Fukuda, U. Ognysta, S. Žumer, and I. Muševič, Nat. Phys. **13**, 1215 (2017).

[98] T. Gibaud, E. Barry, M. J. Zakhary, M. Henglin, A. Ward, Y. Yang, C. Berciu, R. Oldenbourg, M. F. Hagan, D. Nicastro, R. B. Meyer, and Z. Dogic, Nature **481**, 348 (2012).

[99] O. Henrich, K. Stratford, D. Marenduzzo, and M. E. Cates, Proc. Natl. Acad. Sci. U.S.A. **107**, 13212 (2010).

[100] J.-i. Fukuda and S. Žumer, Phys. Rev. E **87**, 042506 (2013).

[101] H. Grebel, R. M. Hornreich, and S. Shtrikman, Phys. Rev. A **28**, 1114 (1983).

[102] P. van der Schoot, J. Phys. Chem. B **103**, 8804 (1999).

[103] A. J. McDonald, M. P. Allen, and F. Schmid, Phys. Rev. E **63**, 010701 (2000).

[104] W. Chen, T. Sato, and A. Teramoto, Macromolecules **31**, 6506 (1998).

[105] I. I. Smalyukh, Y. Lansac, N. A. Clark, and R. P. Trivedi, Nat. Mater. **9**, 139 (2010).

[106] P. J. Ackerman, J. Van De Lagemaat, and I. I. Smalyukh, Nat. Commun. **6**, 6012 (2015).

[107] Y. Guo, S. Afghah, J. Xiang, O. D. Lavrentovich, R. L. Selinger, and Q.-H. Wei, Soft Matter **12**, 6312 (2016).

[108] G. Posnjak, S. Čopar, and I. Muševič, Sci. Rep. **6**, 26361 (2016).

[109] T. Gibaud, J. Phys. Condens. Matter **29**, 493003 (2017).

[110] P. Sharma, A. Ward, T. Gibaud, M. Hagan, and Z. Dogic, Nature **513**, 77 (2014).

[111] L. Metselaar, A. Doostmohammadi, and J. M. Yeomans, J. Chem. Phys. **150**, 064909 (2019).

[112] J. D. Watson and F. H. C. Crick, Nature **171**, 737 (1953).

[113] H. C. Berg and R. A. Anderson, Nature **245**, 380 (1973).

[114] Y. Bouligand, *Liquid Crystalline Order in Biological Materials* (Academic Press, New York, 1978).

[115] M. Novak, B. Polak, J. Simunić, Z. Boban, B. Kuzmić, A. W. Thomae, I. M. Tolić, and N. Pavin, Nat. Commun. **9**, 3571 (2018).

[116] Y. H. Tee, T. Shemesh, V. Thiagarajan, R. F. Hariadi, K. L. Anderson, C. Page, N. Volkmann, D. Hanein, S. Sivaramakrishnan, M. M. Kozlov, et al., Nat. Cell Biol. **17**, 445 (2015).

[117] G. Duclos, C. Blanch-Mercader, V. Yashunsky, G. Salbreux, J.-F. Joanny, J. Prost, and P. Silberzan, Nat. Phys. **14**, 728 (2018).

[118] C. A. Whitfield, T. C. Adhyapak, A. Tiribocchi, G. P. Alexander, D. Marenduzzo, and S. Ramaswamy, Eur. Phys. J. E **40**, 50 (2017).

[119] A. Maitra and M. Lenz, Nat. Commun. **10**, 920 (2019).

[120] S. Fürthauer, M. Strempel, S. W. Grill, and F. Jülicher, Eur. Phys. J. E **35**, 89 (2012).

[121] A. Doostmohammadi, M. F. Adamer, S. P. Thampi, and J. M. Yeomans, Nat. Commun. **7**, 10557 (2016).

[122] C. Peng, T. Turiv, Y. Guo, Q.-H. Wei, and O. D. Lavrentovich, Science **354**, 882 (2016).

[123] K. Doxzen, S. K. Vedula, M. C. Leong, H. Hirata, N. S. Gov, A. J. Kabla, B. Ladoux, and C. T. Lim, Integr. Biol. **5**, 1026 (2013).

[124] H. Wioland, F. G. Woodhouse, J. Dunkel, J. O. Kessler, and R. E. Goldstein, Phys. Rev. Lett. **110**, 268102 (2013).

[125] A. Opathalage, M. M. Norton, M. P. N. Juniper, B. Langeslay, S. A. Aghvami, S. Fraden, and Z. Dogic, Proc. Natl. Acad. Sci. U.S.A. **116**, 4788 (2019).

[126] S. Fürthauer and S. Ramaswamy, Phys. Rev. Lett. **111**, 238102 (2013).

[127] E. Tjhung, M. E. Cates, and D. Marenduzzo, Proc. Natl. Acad. Sci. U.S.A. **114**, 4631 (2017).

[128] P. Guillamat, J. Ignés-Mullol, and F. Sagués, Proc. Natl. Acad. Sci. U.S.A. **113**, 5498 (2016).

[129] R. Voituriez, J.-F. Joanny, and J. Prost, Eur. Phys. Lett. **70**, 404 (2005).

[130] S. Ramaswamy and M. Rao, New J. Phys. **9**, 423 (2007).

[131] L. Giomi, M. J. Bowick, X. Ma, and M. C. Marchetti, Phys. Rev. Lett. **110**, 228101 (2013).

[132] S. P. Thampi, R. Golestanian, and J. M. Yeomans, Phys. Rev. Lett. **111**, 118101 (2013).

[133] B. Martínez-Prat, J. Ignés-Mullol, J. Casademunt, and F. Sagués, Nat. Phys. **15**, 362 (2019).

[134] P. Guillamat, J. Ignés-Mullol, and F. Sagués, Nat. Commun. **8**, 564 (2017).

[135] S. P. Thampi, R. Golestanian, and J. M. Yeomans, Phys. Rev. E **90**, 062307 (2014).

[136] S. J. DeCamp, G. S. Redner, A. Baskaran, M. Hagan, and Z. Dogic, Nat. Mater. **14**, 1110 (2015).

[137] M. Schuppler, F. C. Keber, M. Kröger, and A. R. Bausch, Nat. Commun. **7**, 13120 (2016).

[138] M. M. Genkin, A. Sokolov, O. D. Lavrentovich, and I. S. Aranson, Phys. Rev. X **7**, 011029 (2017).

[139] S. Zhou, O. Tovkach, D. Golovaty, A. Sokolov, I. S. Aranson, and O. D. Lavrentovich, New J. Phys. **19**, 055006 (2017).

[140] J. S. Lintuvuori, A. Würger, and K. Stratford, Phys. Rev. Lett. **119**, 068001 (2017).

[141] V. Schaller, C. Weber, C. Semmrich, E. Frey, and A. R. Bausch, Nature **467**, 73 (2010).

[142] I. H. Riedel, K. Kruse, and J. Howard, Science **309**, 300 (2005).

[143] S. J. DeCamp, G. S. Redner, A. Baskaran, M. F. Hagan, and Z. Dogic, Nat. Mater. **14**, 1110 (2015).

[144] S. Zhou, A. Sokolov, O. D. Lavrentovich, and I. S. Aranson, Proc. Natl. Acad. Sci. U.S.A. **111**, 1265 (2014).

[145] P. W. Ellis, D. J. G. Pearce, Y.-W. Chang, G. Goldsztein, L. Giomi, and A. Fernández-Nieves, Nat. Phys. **14**, 85 (2018).

[146] D. J. G. Pearce, P. W. Ellis, A. Fernandez-Nieves, and L. Giomi, Phys. Rev. Lett. **122**, 168002 (2019).

[147] F. Alaimo, C. Köhler, and A. Voigt, Sci. Rep. **7**, 5211 (2017).

[148] D. Khoromskaia and G. P. Alexander, New J. Phys. **19**, 103043 (2017).

[149] S. Henkes, M. C. Marchetti, and R. Sknepnek, Phys. Rev. E **97**, 042605 (2018).

[150] I. Nitschke, S. Reuther, and A. Voigt, Phys. Rev. Fluids **4**, 044002 (2019).

[151] H. Shin, M. J. Bowick, and X. Xing, Phys. Rev. Lett. **101**, 037802 (2008).

[152] A. Livshits, L. Shani-Zerbib, Y. Maroudas-Sacks, E. Braun, and K. Keren, Cell Rep. **18**, 1410 (2017).

[153] E. Braun and K. Keren, BioEssays **40**, 1700204 (2018).

[154] M. A. Bates, G. Skačej, and C. Zannoni, Soft Matter **6**, 655 (2010).

[155] F. Serra, Liq. Cryst. **43**, 1920 (2016).

[156] M. Mayer, M. Depken, J. S. Bois, F. Jülicher, and S. W. Grill, Nature **467**, 617 (2010).

[157] G. Salbreux and F. Jülicher, Phys. Rev. E **96**, 032404 (2017).

[158] A. Mietke, F. Jülicher, and I. F. Sbalzarini, Proc. Natl. Acad. Sci. U.S.A. **116**, 29 (2019).

[159] G. Nyström, M. Arcari, and R. Mezzenga, Nat. Nanotechnol. **13**, 330 (2018).

[160] D. Bonn, M. Kobylko, S. Bohn, J. Meunier, A. Morozov, and W. van Saarloos, Phys. Rev. Lett. **93**, 214503 (2004).

[161] A. K. Balin, "Statistical mechanics of colloids and active matter in and out of equilibrium", PhD thesis (University of Oxford, 2017).